DESIGN, EXPERIMENT, AND ANALYSIS OF A PHOTOVOLTAIC ABSORBING MEDIUM WITH INTERMEDIATE LEVELS

A Thesis
Presented to
The Academic Faculty

by

Michael Y. Levy

In Partial Fulfillment
of the Requirements for the Degree
Doctor of Philosophy in the
School of Electrical and Computer Engineering

Georgia Institute of Technology
August 2008

DESIGN, EXPERIMENT, AND ANALYSIS OF A PHOTOVOLTAIC ABSORBING MEDIUM WITH INTERMEDIATE LEVELS

Approved by:

Professor Alan Doolittle,
Committee Chair
School of Electrical and Computer Engineering
Georgia Institute of Technology

Professor Stephen Ralph
School of Electrical and Computer Engineering
Georgia Institute of Technology

Professor Christiana Honsberg, Advisor
School of Electrical and Computer Engineering
Georgia Institute of Technology

Professor Ajeet Rohatgi
School of Electrical and Computer Engineering
Georgia Institute of Technology

Professor David Citrin
School of Electrical and Computer Engineering
Georgia Institute of Technology

Professor Phillip First
School of Physics
Georgia Institute of Technology

Date Approved: 15 April 2008

This dissertation is dedicated to my mother, Phoebe Lynn Levy.
It is her dedication to me that manifests this contribution to you.

ACKNOWLEDGEMENTS

The author ackowledges Dr. Christiana Honsberg and Dr. David Citrin, my co-advisors, for fostering my development as a scientist and engineer. The author acknowledges Dr. Alan Doolittle (chair), Dr. Phillip First, Dr. Stephen Ralph, and Dr. Ajeet Rohatgi for their service as members of my disseration committee. The author acknowledges Phoebe Levy (chief), Sheldon Haas, Loren Gomez, Jo Anna Ruddel, and Esther Levy for their service as members of my editorial committee. The author acknowledges Marilou Mycko and the remaining personnel of the School of Electrical and Computer Engineering at the Georgia Institute of Technology for their the ever-present professionalism.

The author acknolwedges the U.S. National Renewable Energy Laboratory for its financial suport via subcontract XAT-5-44277-01 administered by Martha Symko-Davies and Robert McConnell, the U.S. National Science Foundation for its financial support in the form of Ph.D. dissertation enhancement award OISE-0509001 administered byJeanne Hudson, and the Giving Tree Fund for its financial support in the form of grant #CU4L8R.

The author acknoledges Dr. Michele Goano for expeditiously providing the MATLAB version of algorithm 745; Dr. Stephen Bremner and Dr. Guangming Liu for leading the molecular beam epitaxy growth; Dr. Gabriela Stoleru, Dr. Yuanchang Zhang, and Dr. Anup Pancholi for leading the photoluminescent spectroscopy; Dr. Nikolai Faleev for collaborating on the X-ray diffractometry; Dr. Steven Hegedus for collaborating on the absorptivity measurements; Kunal Ghosh and Keun-Yong Ban for assisting with the atomic force microscopy; Dr. Antonio Martí, Dr. David Fuertes and *becaria* Enrique Cánovas for collaborating on the photoreflectence spectroscopy; Dr. Andrew Norman for his trenchant remark regarding the Varshni parameters; Dr. Alan Ristow for his assistance in getting me started with LaTeX; and Gavriel Levy for his technical mantra "do it systematically".

Of all my professional peers, I acknowledge Sean Jacobs for the quantity and quality of the technical assistance he gave and for the breadth of the scientific exchange we shared. I

further acknolwedge my laboratory mates, Omkar Jani, Bhumika Chabra, Chris Kerestes, Mohit Mehta, Som Dahal, Paola Murcia, and Balakrishnam Jampana, for making their computer resources available to me. The author acknowledges Dr. Antonio Martí, Dr. César Tablero, *becaria* Elisa Antolín, Dr. N.J. Ekins-Daukes, and Dr. Ernest Croot for the many engaging scientific and intellectual conversations we have shared through the years. The author is grateful to the people of *Instituto de Energía Solar* of the *Universidad Politécnica de Madrid* for the scientific and inter-personal exchanges during the summers of 2003, 2004, 2005, 2006, and 2007.

TABLE OF CONTENTS

LIST OF TABLES

LIST OF FIGURES

SUMMARY

The absorption of the sun's radiation and its efficient conversion to useful work by a photovoltaic solar cell is of interest to the community at large. Scientists and engineers are particularly interested in approaches that exceed the Shockley-Queisser limit of photovoltaic solar-energy conversion (Chapter 1). The abstract notion of increasing the efficiency of photovoltaic solar cells by constructing a three-transition solar cell via an absorber with intermediate levels is well-established (Chapter 2). Until now, proposed approaches to realize the three-transition solar cell do not render the efficiency gains that are theorized; therefore, researchers are experimenting to ascertain where the faults lie (Chapter 2). In my opinion, it is unclear if the abstract efficiency gains are obtainable. Furthermore, it is difficult to determine whether three-transition absorbers are even incorporated in the existing three-transition solar cell prototypes (Chapter 2). I assert that there are material systems derived from the technologically important compound semiconductors and their ternary alloys that more clearly determine the suitability of employing nanostructured absorbers to realize a three-transition solar cell.

The author reports on a nanostructured absorber composed of InAs quantum dots completely enveloped in a $GaAs_{1-x}Sb_x$ ($x \approx 0.12$) matrix that is grown by molecular beam epitaxy (Chapter 6). The material system, $InAs/GaAs_{0.88}Sb_{0.12}$, is identified as an absorber for a three transition solar cell (Chapter 4). This material system will more easily determine the suitability of employing nanostructured absorbers because its quantum-dot heterojunctions have negligible valence-band discontinuities, which abate the difficulty of interpreting optical experimental results (Chapter 4). A key tool used to identify the $GaAs_{1-x}Sb_x$ ($x \approx 0.12$) is a maximum-power iso-efficiency contour plot (Chapter 4). This contour plot is only obtainable by first having analyzed the impact of both finite intermediate-band width and spectral selectivity on the optimized detailed-balance conversion efficiencies of the three-transition solar cell (Chapter 3). Obtaining the contour plot is facilitated by employing

a rapid and precise method to calculate particle flux (Appendix A). The author largely determines the electronic structure of the InAs/$GaAs_{1-x}Sb_x$ ($x \approx 0.12$) absorber that is grown by molecular beam epitaxy from optical experimental methods and in particular, from photoluminescent spectroscopy (Chapter 6). The interpretation of the experimental photoluminescent spectrum is facilitated by having first studied the theoretical photoluminescent spectra of idealized three-transition absorbers (Chapter 5).

This dissertation is given in six chapters and is supported by three appendices. In chapters 1 and 2 the author reviews the origin and history of this dissertation. In chapters 3, 4, 5, and 6 the author offers original research. The author now sequentially summarizes each chapter and identifies the paramount conclusions and, where applicable, the novelties.

In Chapter 1, the author describes an ideal *p*-*n* junction solar cell, reviews three important approaches that establish upper-limiting efficiencies of solar energy conversion, and reviews four approaches for realizing a global efficiency enhancement with respect to the maximum-power conversion-efficiency of a single *p*-*n* junction solar cell. The author concludes that research and development on next-generation proposals is justified.

In Chapter 2, the author reviews the theoretical operation of an idealized three-transition solar cell, proposals to realize a three transition solar cell, and experimental work that aims to confirm the theoretical precepts on which the large efficiency of the three-transition solar cell is premised. The author concludes that the solar energy conversion efficiency of a three-transition solar cell may nearly reach that of a tandem stack of three single-junction, single-transition solar cells; that an idealized three-transition solar cell is more spectrally robust than an idealized tandem stack of three solar cells electrically assembled in series; that a global efficiency enhancement is not illustrated experimentally; and that, at present, a body of experimental evidence to confirm the existence of either a three-transition absorber or a three-transition solar cell is absent from the literature.

In Chapter 3, the author examines the maximum-power efficiencies of solar cells under non-ideal conditions. This work is novel in two respects: the inclusion of photo-induced electronic transitions between two distinct states of the intermediate band; and the quantification of the impact of both finite intermediate band width and spectral selectivity on

the optimized detailed-balance conversion efficiencies of the three-transition solar cell and its associated band structure. The author concludes that photo-induced intraband electronic transitions are necessary to yield physically consistent results and that the width of the intermediate band ought to be roughly less than 800 meV to have large conversion efficiencies.

In Chapter 4, the author identifies nanostructured absorbers to fabricate a three-transition solar cell. Quantitative design rules are elucidated and these rules are applied to the technologically important III-V binary and ternary semiconductors. A novel design rule mandates a negligible valence-band discontinuity between the barrier and quantum-dot materials. The author concludes that nanostructures composed of InAs confined in GaAsSb is particularly well-suited for a three-transition solar cell.

In Chapter 5, the author describes the absorption and emission of photons by three-transition absorbers based on parabolic-band approximations. The author concludes that a three-transition absorber may absorb all photons with energies greater than the smallest bandgap in the system and, although, in principle, a criterion for complete absorption without concomitant absorption overlaps exists, achieving this criterion is non-trivial. Based on the parabolic-band approximations, novel spectroscopic consequences of three-transition absorbers are illustrated. The author concludes that the photoluminescent spectra of intermediate-band absorbers may have content within four well-separated spectral bands.

In Chapter 6, the author reports on a quantum-dot absorber fabricated by molecular beam epitaxy. The novelty is that the InAs quantum dots are completely enveloped in a barrier of GaAsSb. The author concludes that when using optical experimental methods, detecting photons within the infrared regime of the electromagnetic spectrum is necessary to confirm that the the InAs/$GaAs_{1-x}Sb_x$ ($x \approx 0.12$) absorber is, in fact, a three-transition absorber and, more generally, that any absorber is a three-transition absorber that is appropriate for a three-transition solar cell.

CHAPTER I

PHOTOVOLTAIC SOLAR ENERGY CONVERSION

1.1 Intoduction

Of interest to the population at large is the efficient photovoltaic conversion of the 1000 Watts per square meter of solar irradiance incident on the surface of the earth. In Section 1.2, the present author describes an ideal *p*-*n* junction solar cell. The present author distinguishes the solar cell's absorber, its function, and its relation to the other essential components of the solar cell. In Section 1.3, the present author reviews three important approaches that establish upper-limiting efficiencies of solar energy conversion: the radiation-in-radition-out approach of Landsberg and Tonge, the omni-colour approach of DeVos, Grosjean, and Pauwels, and the detailed-balance approach of Shockley and Queisser. The detailed-balance approach establishes the maximum-power conversion-efficiency of a single *p*-*n* junction solar cell in the terrestrial environment as 40.7%. Yet, the omni-colour approach establishes the maximum-power conversion-efficiency of solar energy in the terrestrial environment as 86.8%. In Section 1.4, the present author reviews four approaches for realizing a global efficiency enhancement with respect to the maximum-power conversion-efficiency of a single *p*-*n* junction solar cell. The current technological paradigm experimentally demonstrates high-efficiencies by using stacks of *p*-*n* junction solar cells operating in tandem. Other next-generation approaches propose the incorporation one or more physical phenomena (*e.g.*, multiple transitions, multiple electron-hole pair generation, and hot carriers) to reach high-efficiencies. In Section 1.5, the present author concludes that research and development on next-generation proposals are justified because each next-generation solar cell may offer a global-efficiency enhancement when operating on its own and, offer a large efficiency enhancement per solar cell when constituted into a stack of solar cells operating in tandem.

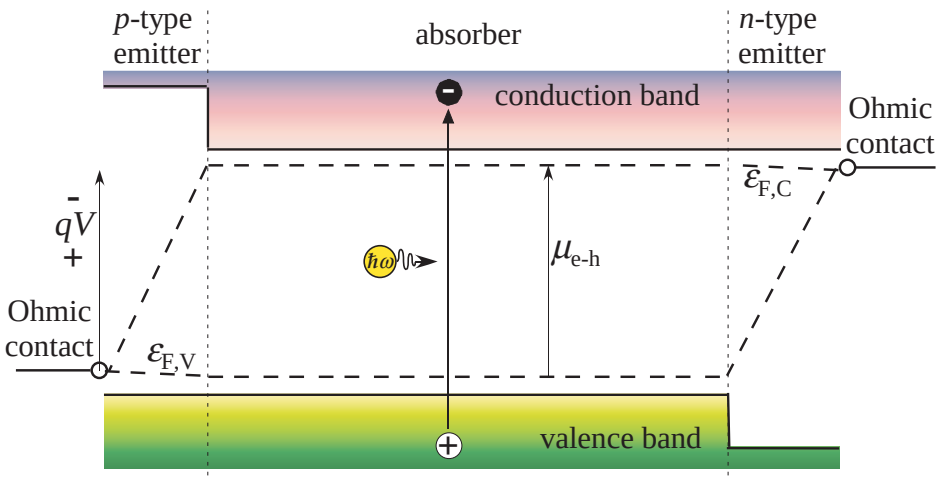

Figure 1: Ideal structure of a solar cell. Shown is the absorber, which is sandwiched between an n-type emitter and a p-type emitter. An Ohmic contact is made to each of the emitters. A voltage, V, exists between the contacts of the solar cell.

1.2 Ideal p-n Junction Solar Cell

In Figure 1, the present author illustrates the ideal electronic structure of a photovoltaic solar cell [1, 2], a device that converts the energy of radiation into electrical energy. The ideal structure of the solar cell is comprised of several components: an absorber, two emitters and two contacts. The absorber enables photo-chemical conversion, the emitters enable electro-chemical conversion, and the contacts enable useful work to be performed by an external load. In the following paragraphs, the present author describes an ideal solar cell in more detail. This is done for the special case in which the absorber is a medium with a single bandgap.

An absorber is in the center of the solar cell. As may be seen in Figure 1, the absorber is a medium whose electronic states form a conduction band and a valence band. The conduction and valence bands are separated by an energetic gap that is characterized by the absence of electronic states. The occupancy of the electronic states of the conduction band and valence band are described by the quasi-Fermi energies $\varepsilon_{F,C}$ and $\varepsilon_{F,V}$, respectively. The absorber is the region of the solar cell where the absorption of photons occurs and where the subsequent generation of electrons and holes takes place. Typically, each photon with energy greater than that of the energetic gap may generate a single electron-hole pair. In

such case, the energy of each supra-gap photon is converted to the chemical energy of an electron-hole pair, $\mu_{\text{e-h}}$, where $\mu_{\text{e-h}} = \varepsilon_{\text{F,C}} - \varepsilon_{\text{F,V}}$ [1, 2].

The absorber is sandwiched between two semi-permeable emitters [1, 2]. The emitters are selected to produce an asymmetry in the band structure. The electronegativity and bandgap of the emitter on the right (*i.e.,* the *n*-type emitter) are selected so that the (*i*) electrons largely or completely permeate through and (*ii*) holes largely or completely do not [1, 2]. A small gradient drives the majority carriers (*i.e.*, holes) to the right so that a beneficial current is produced. A large gradient drives minority carriers (*i.e.*, electrons) to the right so that a detrimental current is produced. The latter current is very small, resulting from the relative impermeability of the rightmost emitter to electrons. The emitter on the left is similarly selected, except that it is the holes that permeate through and yield a beneficial current.

On the external surface of both emitters is a metallic contact. The carriers in the contacts are in equilibrium with one another, so where the contact interfaces with the emitter the occupancy of holes and electrons are described by the same Fermi energy. That absolute value of the Fermi energy at both contacts is roughly equal to the absolute value of the quasi-Fermi energy of majority carriers where the absorber interfaces with the emitter. Thus, between the two contacts there is a voltage, V, that is proportional to the potential difference $\varepsilon_{\text{F,C}} - \varepsilon_{\text{F,V}}$ as $V = (\varepsilon_{\text{F,C}} - \varepsilon_{\text{F,V}})/q$, where q is the elementary charge. Therefore, the chemical energy of each electron-hole pair, $\mu_{\text{e-h}}$, is converted to electrical energy by a unit pulse of charge current, q, at the voltage V. In the following subsection, the present author reviews various limits describing the efficiency of solar energy conversion.

1.3 Limits to Ideal Solar Energy Conversion

In this section, the present author reviews three distinct approaches to upper-bound the efficiency of solar energy conversion. In Section 1.3.1, the present author offers a schematic of a generalized converter and uses the schematic to define the conversion efficiency. In sections 1.3.2, 1.3.3, and 1.3.4, the present author reviews the Landsberg-Tonge limit, the Shockley-Queisser limit, and the omni-colour limit, respectively. In Section 1.3.5, the

present author compares and contrasts these three approaches. Finally, in Section 1.3.6, the present author draws conclusions regarding the upper-theoretical efficiency of converting solar energy to electricity in the terrestrial environment. The present author concludes that though the efficiency limit of a single p-n junction solar cell is large, a significant efficiency enhancement is possible. This is because, in the first approximation, the terrestrial limits of a single p-n junction solar cell are 40.7% and 24.0%, whereas those of an omnicolour converter are 86.8% and 52.9% for fully-concentrated and non-concentrated sunlight, respectively.

1.3.1 Generalized Energy Converter

Figure 2 is a schematic of a generalized energy converter (*c.f.* the converter in reference [3]). The converter is pumped with a power flow, $\dot{E}_{\mathrm{p}}$, and a rate of entropy flow, $\dot{S}_{\mathrm{p}}$. Analogously, the converter, which maintains a temperature T_{c}, sinks a power flow, $\dot{E}_{\mathrm{s}}$, and a rate of entropy flow, $\dot{S}_{\mathrm{s}}$. Meanwhile, a rate of useable work, $\dot{W}$, is delivered and a rate of heat flow, $\dot{Q}$, is transmitted to the ambient. Internally, the converter experiences a rate change of energy, $\dot{E}$, and a rate change of entropy, $\dot{S}$. In addition, the converter, by its own internal processes, generates a rate of entropy, $\dot{S}_g$.

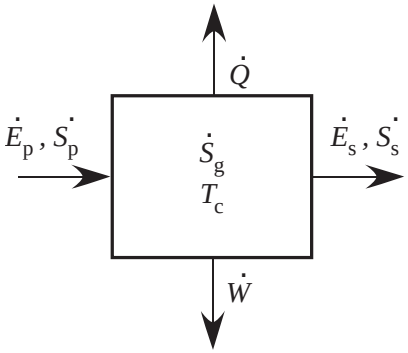

Figure 2: Generalized schematic diagram of an energy converter. In the radiative limit, the energy flows pumped to and sunk by the converter (*i.e.* $\dot{E}_{\mathrm{p}}$ and $\dot{E}_{\mathrm{s}}$) are limited to the radiant energy flux [$\mathrm{J\,m^{-2}\,s^{-1}}$] pumped to and sunk by the converter: $\dot{E}_{\mathrm{p}}$ and $\dot{E}_{\mathrm{s}}$, respectively.

The first-law conversion efficiency, η, is defined as the ratio of the useable power over

the energy flow pumped into the converter, so that [3]

$$\eta \doteq \frac{\dot{W}}{\dot{E}_{\mathrm{p}}}. \tag{1}$$

In the science of solar energy conversion, no more than two radiation flows pump the converter (see Figure 3). Always present is a direct source of radiation from the sun, which is assumed a black body with a surface temperature T_{S}, yielding an energy flux, $\dot{U}_{\mathrm{p,S}}$. Sometimes present, depending on the geometric concentration factor, C, is a diffuse source of radiation scattered from the Earth's atmosphere, which is assumed to be a black body with a surface temperature T_{E}, yielding an energy flux, $\dot{U}_{\mathrm{p,E}}$. Considering the dilution factor of solar radiation, $D\left[2.16 \times 10^{-5}\right]$, and a geometric solar concentration factor, C, which may range between unity and $1/D$ [4], the total energy flux impinging upon the converter, $\dot{E}_{\mathrm{p}}$, is written with the Stefan-Boltzmann constant, $\sigma\left[5.67 \times 10^{-8}\ \mathrm{W/m^2/K^4}\right]$, as

$$\dot{E}_{\mathrm{p}} = \sigma\left[C\,D\,T_{\mathrm{S}}^4 + (1 - C\,D)\,T_{\mathrm{E}}^4\right]. \tag{2}$$

Meanwhile, the quantification of the power density generated by the converter depends on the specific details of the converter. As this section only discusses a generalized converter, no further mathematical form of the power density is specified.

Calculating the performance measure by substituting the right-hand side of Equation (1) into the denominator of Equation (2) is different from the manner of calculating the performance measure as done in the detailed-balance work of references [5, 6, 4, 7, 8, 9, 10, 11, 12, 13, 14]. In the latter references, though the particle flux impinging upon the solar cell is given in terms of the dual source, the performance measure is calculated with respect to the energy flux from the sun, $\dot{U}_{\mathrm{p,S}}$. This distorts the performance measure of the device, resulting in efficiencies $\left[1 + \frac{1-C\,D}{C\,D}\left(\frac{T_{\mathrm{E}}}{T_{\mathrm{S}}}\right)^4\right]$ times those obtained using the first-law efficiency given throughout this dissertation. In the following subsection, the present author reviews an approach to upper bound the efficiency limit of converting solar energy to useful work.

1.3.2 Landsberg-Tonge Limit

Landsberg and Tonge present thermodynamic efficiencies for the conversion of solar radiation into work [3]. The converter is pumped with all the radiation emitted from a black

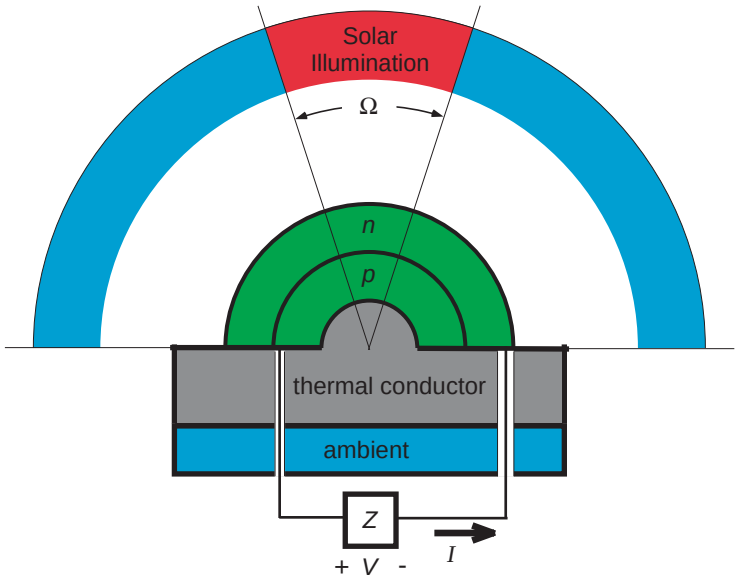

Figure 3: Cross section of an abstracted p-n junction solar cell with spherical symmetry. The exaggerated physical symmetry reinforces the solar geometry, where a solid angle of the solar cell's surface, Ω, is subtended by direct insolation from the sun and the remainder of the hemisphere is subtended by diffuse radiation from the atmosphere. The solid angle may be adjusted by geometrical concentration of the sun's light. The solar cell is maintained at the ambient temperature, the surface terrestrial temperature, by a thermal conductor.

body, which maintains a surface temperature T_p. The converter is also given as a black body, however its temperature is maintained at T_c. The converter, therefore, sinks black-body radiation associated with this temperature. With the use of two balance equations, for energy and for entropy, Landsberg and Tonge derive the following inequality for the first-law efficiency:

$$\eta \leq 1 - \frac{4}{3}\frac{T_\mathrm{c}}{T_\mathrm{p}} + \frac{1}{3}\left(\frac{T_\mathrm{c}}{T_\mathrm{p}}\right)^4 . \tag{3}$$

In arriving at the above inequality, Landsberg and Tonge assume steady-state conditions. Equality holds for the special case where there is no internal entropy generation (*i.e.* $\dot{S}_g = 0$). The resulting equality is first derived by Patela by considering the exergy of heat radiation [15]. The Landsberg-Tonge limit may be extended so as to model the dual sources of the solar geometry [1]. In the case of two black-body sources simultaneously pumping the converter, a derivation similar to that of Landsberg and Tonge yields a first-law efficiency

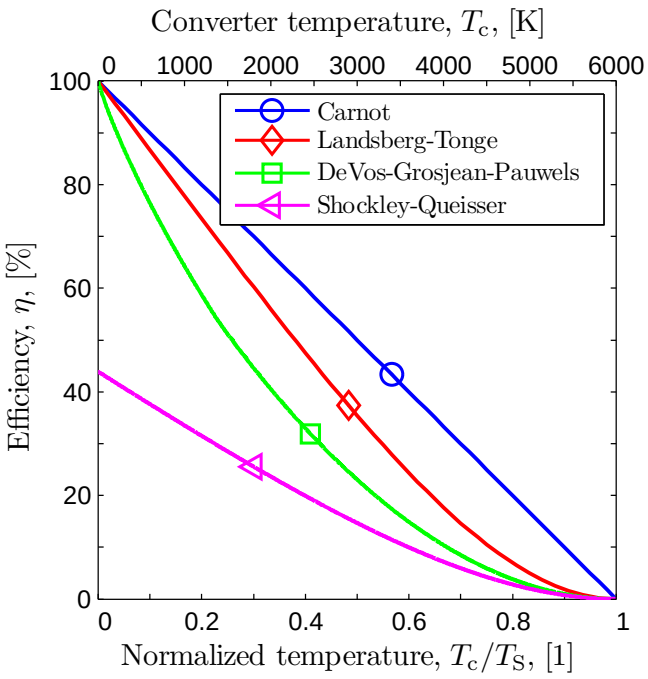

Figure 4: Efficiency limits of ideal solar energy converters as a function of the ratio of the converter's temperature, T_c, to the pump's temperature, T_S. Shown are the Landsberg-Tonge closed-form efficiencies of the radiation-in-radiation-out converter, the DeVos-Grosjean-Pauwels analytic efficiencies of the omni-colour converter, and the Shockley-Queisser numerical efficiencies of the *p-n* junction converter. All efficiencies are for fully-concentrated solar irradiance. As a visual aid, the Carnot efficiencies are presented.

given as

$$\eta \leq \frac{(C\,D)\left(T_S^4 - \frac{4}{3}\,T_c\,T_S^3 + \frac{1}{3}\,T_c^4\right) + (1 - C\,D)\left(T_E^4 - \frac{4}{3}\,T_c\,T_E^3 + \frac{1}{3}\,T_c^4\right)}{(C\,D)\;T_S^4 + (1 - C\,D)\;T_E^4}. \tag{4}$$

Figure 4 illustrates the Landsberg-Tonge efficiency limit. In Section 1.3.3, the detailed-balance method of Shockley and Queisser is presented and applied to a single *p-n* junction solar cell.

1.3.3 Shockley-Queisser Limit

Shockley and Queisser present a framework to analyze the efficiency limit of solar energy conversion by a single *p-n* junction [5]. They name this limit the detailed-balance limit for it is derived from the notion that, in principle, all recombination processes may be limited to photo-induced processes and balanced by photo-induced generation processes. Their *ab initio* limit – as opposed to a semi-empirical limit based on factors such as measured

carrier lifetimes – represents an upper-theoretical limit above which a single p-n junction solar cell may not perform. In addition, it is a reference for experimental measurements of single-junction solar cells in terms of future potential.

In their framework, Shockley and Queisser identify several factors that may degrade the efficiency of energy conversion and ideally allow that the degrading factors are perfectly mitigated. Therefore, in the detailed balance limit it is permissible that:

- the fractions of recombination and generation events that are coupled to radiative processes are both unity,
- the probability that incident photons with energy greater than or equal to the semiconductors band-gap are transmitted into the solar cell is unity,
- the probability with which a transmitted photon creates an electron-hole pair is unity,
- the probability that an electron-hole pair yields a charge current pulse through an external load is unity, and,
- the fraction of solid angle subtended by the sun may be unity- *i.e.*, the sun's radiation is completely concentrated onto the solar cell (see Figure 3 on page 6).

Figure 4 illustrates the upper-efficiency limit of solar energy conversion by a single p-n solar cell. This is given for two distinct geometric concentration factors: fully-concentrated sun light and non-concentrated sun light. In Section 1.3.4, the omni-colour limit is presented.

1.3.4 Omni-Colour Limit

In principle, the detailed-balance method may be applied to omni-colour converters [6, 16, 4]. The omni-colour limit may be derived in terms of either photovoltaic processes [6, 16, 4, 17, 2], photothermal processes [4], or hybrids thereof [4, 18]. In either case, as the number of layers in a stack of photovoltaic converters [19, 20, 21, 22, 4] or in a stack of photothermal converters [23, 4] approach infinity, the solar energy conversion efficiencies approach the same limit [6, 23, 4]- the omni-colour limit. Figure 4 illustrates the upper-efficiency limit of omni-colour solar energy conversion. In Section 1.3.5, the present author compares and contrasts the efficiency limits that are heretofore reviewed.

1.3.5 Comparative Analysis

In Section 1.3.2 through Section 1.3.4, the present author reviews several approaches that quantify the efficiency limits of solar energy conversion. At this point, the aforementioned limits are compared and contrasted.

All of the limits reviewed in this Section 1.3 have in common an efficiency limit of zero when the converter's temperature is that of the pump. In addition, several of the limits approach the Carnot limit for the special case where the converter's temperature is absolute zero. These include the Landsberg-Tonge limit and the omni-colour limit (both for fully-concentrated and non-concentrated solar irradiance). At absolute zero the Shockley-Queisser limit is substantially lower than the Carnot limit.

The large differences between the Shockley-Queisser limit and the other limits are attributed to the relationship between the energetic gap of the semiconductor comprising the p-n junction and the range of photon energies comprising the broadband spectrum of black-body radiation. Sub-bandgap photons do not yield a photovoltaic effect and so do not participate in generating charge current. Meanwhile, the conversion of each supra-bandgap photon uniformly generates a single electron-hole pair at a voltage limited by the bandgap. Therefore, the portion of each supra-bandgap photon's energy in excess of the bandgap does not contribute to useful work. The difference between the omni-colour limit and the Landsberg-Tonge limit is attributed to the generation of internal irreversible entropy. Except for the two temperature extremes aforementioned, each layer of the omni-colour converter generates a rate of irreversible entropy resulting from its internal processes. This is so even though each layer of the omni-colour converter operates at its maximum-power point and converts monochromatic light [2].

As illustrated by the present author in Figure 4, the efficiency limits reviewed heretofore may be given in descending order as Carnot, Landsberg-Tonge, omni-colour, and Shockley-Queisser. Photovoltaic converters may not exceed the omni-colour limit for their internal processes are associated with a rate of irreversible internal entropy generation [24, 25]. In Section 1.3.6, the present author concludes these findings by describing limits to the conversion of solar energy in the terrestrial environment.

1.3.6 Terrestrial Conversion Limits

Table 1 lists the upper-efficiency limits of the terrestrial conversion of solar energy. As is convention in the science of solar energy conversion, all efficiencies are calculated for a surface solar temperature of 6000 K, a surface terrestrial temperature of 300 K, and a converter maintained at the surface terrestrial temperature. In addition, the geometric dilution factor is taken as 2.16×10^{-5} [4]. For each type of converter listed, the upper- efficiency limit is given for fully-concentrated sunlight and, in some cases, for non-concentrated sunlight. The values listed depend only on the sun's surface temperature, the earth's surface temperature, and the geometric concentration factor, as opposed to consideration regarding the air mass of the Earth and other secondary phenomena. The present author concludes that though the upper-efficiency limit of a single *p-n* junction solar cell is large, a significant efficiency enhancement is possible. This is true because the terrestrial limits of a single *p-n* junction solar cell is 40.7% and 24.0%, whereas the terrestrial limits of an omni-colour converter is 86.8% and 52.9% for fully-concentrated and non-concentrated sunlight, respectively. In Section 1.4, the present author defines the notion of high-efficiency approaches to solar energy conversion and briefly reviews various proposed high-efficiency approaches.

1.4 High-Efficiency Approaches

In this section, Section 1.4, the present author reviews several distinct approaches for high-efficiency solar cells. In Section 1.4.1, the present author defines "high-efficiency" in terms of the upper-conversion efficiencies of the Shockley-Queisser solar cell and the omni-colour solar cell. In Section 1.4.2, the present author reviews the current technological paradigm to realize high-efficiency solar cells: stacks of single *p-n* junction solar cells operating in tandem. In sections 1.4.3, 1.4.4, and 1.4.5, the present author reviews three next-generation approaches to realize high-efficiency solar cells: the carrier-multiplication solar cell, the hot-carrier solar cell, and the multiple-transition solar cell, respectively. Finally, in Section 1.4.6, the present author draws conclusions regarding the justification for researching and developing next-generation approaches. Though stacks of single *p-n* junction solar cells operating in tandem are the only high-efficiency approach with demonstrated high-efficiency

Table 1: Upper-efficiency limits of the terrestrial conversion of solar energy, $\eta|_{\text{Ter}}$. All efficiencies calculated for a surface solar temperature of 6000 K, a surface terrestrial temperature of 300 K, a solar cell maintained at the surface terrestrial temperature, a geometric dilution factor, D, of 2.16×10^{-5}, and a geometric concentration factor, C, that is either 1 (non-concentrated sunlight) or $1/D$ (fully-concentrated sunlight).

Converter	$\eta\|_{\text{Ter}}$, [%]	
	$C = 1/D$	$C = 1$ †
Carnot	95.0	95.0
Landsberg-Tonge	93.3 [a]	72.4 [b]
Omni-Colour	86.8 [c]	52.9 [d]
Shockley-Queisser	40.7 [e]	24.0 [f]

† Listed values are first-law efficiencies that are calculated by including the energy flow absorbed due to direct solar radiation and the energy flow due to diffuse atmospheric radiation. The listed values are likely to be less than what are previously recorded in the literature. See Section 1.3.1 on page 4 for a more comprehensive discussion.

[a] Calculated from Equation (3) on page 6.

[b] Calculated from Equation (4) on page 7.

[c] Obtained from reference [6]and reference [2].

[d] Adjusted from the value 68.2% recorded in reference [6] and independently calculated by the present author.

[e] Obtained from reference [14].

[f] Adjusted from the value 31.0% recorded in reference [8].

performance, the present author concludes that development on a next-generation solar cell is justified in that a (i) next-generation solar cells offer a global-efficiency enhancement in themselves and (i) also per layer if incorporated in a stack of solar cells operating in tandem. Immediately below in Section 1.4.1, the present author defines what is meant by high-efficiency performance.

1.4.1 Global Efficiency Enhancement

There are several proposals for high-efficiency solar cells. In this dissertation, similar to Anderson in his discussion of the efficiency enhancements in quantum-well solar cells [26], the present author defines high-efficiency in terms of a global efficiency enhancement. Shown in Figure 5 are the upper-efficiency conversion limits of the single-junction solar cell and the omni-colour solar cell. In Figure 5, the upper-efficiency conversion limits are given as a function of the geometrical concentration factor, C. The present author defines "high efficiency" in terms of the numerical data given in Figure 5. The present author asserts that, for any and all geometric concentration factor, a proposal for high-efficiency solar cell must, when optimized, offer an efficiency greater than that of an optimized Shockley-Queisser solar cell at that same geometric concentration factor. For example, according to the present author's definition, under non-concentrated sunlight a high-efficiency proposal, when optimized, must have an upper-efficiency limit greater than 24.0.%. Clearly, for physical consistency, the optimized theoretical performance of the high-efficiency proposal must be less than that of the omni-colour solar cell at that geometric concentration factor. Furthermore, the present author asserts that any fabricated solar cell that claims to be a high-efficiency solar cell must demonstrate a global efficiency enhancement with respect to an optimized Shockley-Queisser solar cell. For example, to substantiate a claim of high-efficiency, a solar cell maintained at the terrestrial surface temperature and under a geometric concentration of 240 suns must demonstrate an efficiency greater than 35.7%- the efficiency of an optimized Shockley-Queisser solar cell operating under those conditions. Before moving on to Section 1.4.2, where the present author reviews the tandem solar cell, the reader is encouraged to view the high-efficiency regime as illustrated in Figure 5. The reader will note that there is a significant efficiency enhancement that is scientifically plausible.

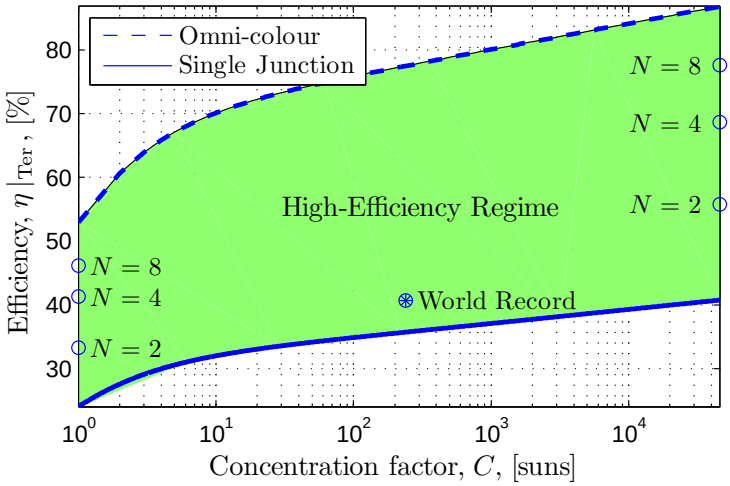

Figure 5: The region of high-efficiency solar energy conversion as a function of the geometric concentration factor. The high-efficiency region is defined as that region offering a global-efficiency enhancement with respect to the maximum single-junction efficiencies (lower edge) and the maximum omni-colour efficiencies (upper edge). The efficiency required to demonstrate a global efficiency enhacnement varies as a function of the geometric concentration factor. For illustrative purposes, the terrestrial efficiencies (see Table 2) of N-stack ($N = 2, 4,$ and 8) solar cells are given for the two extreme concentration factors (*i.e.,* 1 sun and 46,300 suns). Finally, for illustrative purposes, the present world record solar cell efficiency is given (*i.e.*, 40.7% under a concentration of 240 suns [27]).

1.4.2 Tandem Solar Cell

The utilization of a stack of p-n junction solar cells operating in tandem is proposed to exceed the performance of one p-n junction solar cell operating alone [19]. The upper-efficiency limits for N-stack tandems ($1 \leq N \leq 8$) are recorded in Table 2 on page 14 . As the number of solar cells operating in a tandem stack increases to infinity, the upper-limiting efficiency of the stack increases to the upper-limiting efficiency of the omni-colour solar cell [6, 23, 4]. This is explained in Section 1.3.4 on page 8. In practice, solar cells may be integrated into a tandem stack via a vertical architecture or a lateral architecture. An example of a vertical architecture is a monolithic solar cell. Until now, the largest demonstrated efficiency of a monolithic solar cell -or for any solar cell- is the metamorphic solar cell produced by Spectrolab [27]; Spectrolab's three-junction metamorphic solar cell has a conversion efficiency of 40.7% under a concentration of 240 suns [27]. An example of a horizontal architecture is the solar cell of reference [28], which utilizes a spectral-beam

Table 2: Upper-efficiency limits, $\eta|_{\text{Ter}}$, of the terrestrial conversion of stacks of single-transition single p-n junction solar cells operating in tandem. All efficiencies calculated for a surface solar temperature of 6000 K, a surface terrestrial temperature of 300 K, a solar cell maintained at the surface terrestrial temperature, a geometric dilution factor, D, of 2.16×10^{-5}, and a geometric concentration factor, C, that is either 1 (non-concentrated sunlight) or $1/D$ (fully-concentrated sunlight).

Converter	$\eta\|_{\text{Ter}}$, [%]	
	$C = 1/D$	$C = 1$ †
Infinite-Stack Tandem *	86.8 [a]	52.9 [b]
Eight-Stack Photovoltaic Tandem	77.63 [c]	46.12 [e]
Seven-Stack Photovoltaic Tandem	76.22 [c]	46.12 [e]
Six-Stack Photovoltaic Tandem	74.40 [c]	44.96 [e]
Five-Stack Photovoltaic Tandem	72.00 [c]	43.43 [e]
Four-Stack Photovoltaic Tandem	68.66 [c]	41.31 [d]
Three-Stack Photovoltaic Tandem	63.747 [c]	38.21 [d]
Two-Stack Photovoltaic Tandem	55.80 [c]	33.24 [d]
One-Stack Photovoltaic Solar Cell **	40.74 [c]	24.01 [d]

† Listed values are first-law efficiencies that are calculated by including the energy flow absorbed due to direct solar radiation and the energy flow due to diffuse atmospheric radiation. The listed values are likely to be less than what are previously recorded in the literature. See Section 1.3.1 on page 4 for a more comprehensive discussion.

* Recorded values are identical to those of the omni-colour converter of Table 1 on page 11.

** Recorded values are identical to those of the Shockley-Queisser converter of Table 1 on page 11.

[a] Obtained from reference [6] and independently calculated by the present author.

[b] Adjusted from the value 68.2% recorded in reference [6] and independently calculated by the present author.

[c] Obtained from reference [14] and independently calculated by the present author.

[d] Adjusted from the values recorded in reference [8] and independently calculated by the present author.

[e] Calculated independently by the present author. Values are not published in the literature.

splitter [29] and appropriately directs the resulting light onto its constituent solar cells. The present author now reviews the carrier-multiplication solar cell, the first of three next-generation proposals to be reviewed in this dissertation.

1.4.3 Carrier-Multiplication Solar Cell

Carrier-multiplication solar cells are theorized to exceed the Shockley-Queisser limit [30, 31, 7, 9], thus they may be correctly viewed as a high-efficiency approach. These solar cells produce an efficiency enhancement by generating more than one electron-hole pair per absorbed photon via inverse-Auger processes [31] or via impact-ionization processes [30, 32]. The efficiency enhancement is calculated by several authors [30, 31, 7]. Depending on the assumptions, the upper limit to terrestrial conversion of solar energy using the carrier-multiple solar cell is 85.4% [7] or 85.9% [9]. Though the carrier-multiple solar cell is close to the upper-efficiency limit of the omni-colour solar cell, the latter is larger than the former because the former is a two-terminal device. The present author now reviews the hot-carrier solar cell, the second of three next-generation proposals to be reviewed in this dissertation.

1.4.4 Hot-Carrier Solar Cell

Hot-carrier solar cells are theorized to exceed the Shockley-Queisser limit [33, 34, 25], thus they may be correctly viewed as a high-efficiency approach. These solar cells generate one electron-hole pair per photon absorbed. In describing this solar cell, it is assumed that carriers in the conduction band may interact with themselves and thus equilibrate to the same chemical potential and same temperature [33, 34, 25]. The same may be said about the carriers in the valence band [33, 34, 25]. However, the carriers do not interact with phonons and thus are thermally insulated from the absorber. Resulting from a mono-energetic contact to the conduction band and a mono-energetic contact to the valence band, it may be shown that (*i*), the output voltage may be greater than the conduction-to-valence bandgap and that (*ii*) the temperature of the carriers in the absorber may be elevated with respect to the absorber. The efficiency enhancement is calculated by several authors [33, 34, 25]. Depending on the assumptions, the upper-conversion efficiency of any hot-carrier solar cell is asserted to be 85% [2] or 86% [34]. The present author now reviews the multiple-transition solar cell, the third of three next-generation proposals to be reviewed in this dissertation.

1.4.5 Multiple-Transition Solar Cell

The multi-transition solar cell is an approach that may offer an improvement to solar energy conversion as compared to a single p-n junction, single-transition solar cell [20]. The multi-transition solar cell utilizes energy levels that are situated at energies below the conduction band edge and above the valence band edge. The energy levels allow the absorption of a photon with energy less than that of the conduction-to-valence band gap. Wolf uses a semi-empirical approach to quantify the solar energy conversion efficiency of a three-transition solar cell and a four-transition solar cell [20] (for a more detailed review of this approach, the reader is encouraged to view Section 2.2.1 on page 21). Wolf calculates an upper-efficiency limit of 51% for the three-transition solar cell and 65% four-transition solar cell [20].

Subsequently, as opposed to the semi-empirical approach of Wolf, the detailed-balance approach is applied to multi-transition solar cells. The upper-efficiency limit of the three-transition solar cell is now established at 63.2% [35, 36, 37] (for a more comprehensive review of this approach, the reader is encouraged to view Chapter 2.). In addition, the upper-conversion efficiency limits of N-transition solar cells are examined [12, 38]. Depending on the assumptions, the upper-conversion efficiency of any multi-transition solar cell is asserted to be 77.2% [12] or 85.0% [38]. These upper-limits justify the claim that the multiple-transition solar cell is a high-efficiency approach. Resulting from internal current constraints and voltage constraints, the upper-efficiency limit of the multi-transition solar cell is asserted to be less than that of the omni-colour converter [12, 38].

1.4.6 Justification for Next-Generation Approaches

In this section, Section 1.4, the present author defines the high-efficiency regime of a solar cell. The only approach to demonstrate a high-efficiency solar cell is the current technological paradigm of stacks of single p-n junction solar cells operating in tandem. The current world record belongs to a stack of three single p-n junction solar cells operating in tandem. The record efficiency demonstrated by this solar cell is 40.7% at 240 suns. This efficiency may be compared with the optimized Shockley-Queisser solar cell and the optimized omni-colour solar cell under these same operating conditions: 35.7% and 77.5%,

respectively. Based on this, the present author concludes that research and development on next-generation approaches is warranted.

The author justifies this conclusion by noting that even if a three-stack tandem solar cell achieves its terrestrial efficiency limit (63.7%), it will still fall short of the omnicolour limit (86.8%). Using the current technological paradigm, any additional significant efficiency gains will require the inclusion of more single *p-n* junction operating in tandem. However, as the number of *p-n* junctions increases, the current technological paradigms are increasingly problematic. This is due to the fundamental limitation of compatible materials with which to fabricate a tandem stack from many single-junction devices. The next generation approaches are elegant, because their single absorbing media may perform as a tandem stack of several single junctions. The next-generation approaches represent a paradigm shift, allowing for a significant efficiency enhancement per layer operating in a tandem stack. In the following section, Section 1.5, the present author, within the context of this dissertation, concludes the review of photovoltaic solar energy conversion.

1.5 Conclusions

The author begins Chapter 1 by reviewing the operation of an idealized single-transition, single *p-n* junction solar cell. The present author concludes that though the upper-efficiency limit of a single *p-n* junction solar cell is large, a significant efficiency enhancement is possible. This is so because the terrestrial limits of a single *p-n* junction solar cell is 40.7% and 24.0%, whereas the terrestrial limits of an omni-colour converter is 86.8% and 52.9% for fully-concentrated and non-concentrated sunlight, respectively. There are several high-efficiency approaches proposed to bridge the gap between the single-junction limit and the omni-colour limit. Only the current technological paradigm of stacks of single *p-n* junctions operating in tandem experimentally demonstrates efficiencies with a global efficiency enhancement. However, the gap between the present technological record (40.7%) and sound physical models indicates significant room to continue to enhance the performance of solar energy conversion. The current technological paradigm is not likely to experimentally demonstrate significant gains in efficiency. This is a consequence of the inherent limitation

of compatible materials with which to fabricate a tandem stack from many single-junction solar cells. In conclusion, research and development on next-generation proposals are justified because next generation solar cells have large efficiencies when calculated on their own and, in addition, yield larger (with respect to p-n junctions) efficiencies per solar cell when constituted into horizontal or vertical stacks of solar cells operating in tandem. In the following chapter, the present author reviews the three-transition solar cell.

CHAPTER II

THREE-TRANSITION SOLAR CELL

2.1 Introduction

Increasing the efficiency of photovoltaic solar cells by constructing a three-transition solar cell via an absorber with intermediate states is a well-established abstract notion. Until now, proposed approaches to realize the three-transition solar cell do not validate the global efficiency enhancement that is theorized. For this reason, researchers are experimenting to ascertain where the faults lie. In this chapter, the present author reviews the theoretical operation of an idealized three-transition solar cell, reviews proposals to realize a three-transition solar cell, and reviews the experimental characterization of prototype three-transition solar cells.

In section 2.2, the present author reviews the theoretical operation of idealized three-transition solar cells. The major difference between the operations of the three-transition solar cell and the single-junction solar cell results from their distinct absorbers. A three-transition solar cell has an absorber with electronic states energetically between and electronically isolated from those of the conduction band and valence band. The present author draws two conclusions pertaining to the merit of the three-transition solar cell. The present author concludes that the solar energy conversion efficiency three-transition solar cell may nearly reach that of a tandem-stack of three single-junction, single-transition solar cells. The present author further concludes that an idealized three-transition solar cell is more spectrally robust than an idealized tandem-stack of three solar cells electrically assembled in series. Therefore, whether the absolute optimum band structure may or may not be practically obtainable, the solar energy conversion efficiency will degrade gently as the practically-obtainable band structure deviates from the optimum band structure.

In section 2.3, the present author reviews proposals to construct a three-transition solar cell. Each proposal may be distinguished by their respective approach to synthesize the

three-transition absorber. Proposed approaches to realize a three-transition absorber include the following: (1) where the intermediate states are those of localized states of dopants introduced into a host semiconductor, (2) where the intermediate states are those that comprise subbands introduced by quantum-well heterojunctions, (3) where the intermediate states are those that comprise a miniband introduced by quantum-dot heterojunctions, and (4) where the intermediate states are those of extended states of dopants introduced into a host semiconductor. Based on the summary of these proposals, the present author concludes that a global efficiency enhancement is not illustrated experimentally.

In section 2.4, the present author reviews experimental works that aim to confirm the theoretical precepts on which the large efficiency of the three-transition solar cell is premised. These precepts relate to the absorption of photons, emission of photons, collection of charge carriers, generation of charge current, production of a photovoltage, and the separation of quasi-Fermi levels. The present author concludes that currently, a body of experimental evidence to support the existence of either a three-transition absorber or a three-transition solar cell is absent from the literature. The present author further concludes that the absence of infrared detection while recording absorption and emission spectra severely hampers the ability to directly observe the existence of a three-transition absorber and three-transition solar cell.

2.2 Operation of the Three-Transition Solar Cell

In this section, Section 2.2, the present author describes the operation of the three-transition solar cell. In section 2.2.1, the present author reviews the semi-empirical approach of Wolf [20]. It is explained that by utilizing energy levels in the previously forbidden bandgap, the three-transition so lar cell has a potential ly better performance than other single-junction, single-transition solar cells. In section 2.2.2, the present author reviews the detailed-balance approach of Luque and Martí [35]. It is explained how Luque and Martí quantify the upper-efficiency limit of a three-transition solar cell. In section 2.2.3, the present author reviews the relationship between the reduced-band diagram of the solar cell and its general

equivalent circuit [39, 36, 40, 41]. It is explained that the solar cell is equivalent to a tandem-stack of three single-junction solar cells electrically assembled by a combined series/parallel interconnect [42]. In section 2.2.4, the present author reviews the detailed-balance approach of Levy and Honsberg [37]. The novelty of their work is in quantifying the impact of both finite intermediate band width and spectral selectivity on the optimized detailed-balance conversion efficiencies of the three-transition solar cell solar cell and its associated band structure [37]. The work is significant as it shows that finite bandwidths result in a graceful degradation in the efficiency [37]. Finally, in section 2.2.5, the present author draws two conclusions. First, the three-transition solar cell is attractive because it provides a significant efficiency enhancement per layer of a stack of solar cells operating in tandem. For example, a two-stack of three-transition solar cell may nearly reach the efficiency limit of a six-stack of single-transition, single-junction solar cells operating in tandem. Second, whether the absolute optimum band structure may or may not be practically obtainable, the efficiency will degrade gently as the band structure deviates from the optimum band structure. This results from the fact that an idealized three-transition solar cell is more spectrally robust than an idealized tandem-stack of three solar cells electrically assembled in series.

2.2.1 Semi-Empirical Approach of Wolf

In 1960, Wolf proposes multi-transition solar cells as an approach to realize high-efficiency solar energy conversion. In this subsection, the present author reviews Wolf's semi-empirical approach. In Figure 6 the present author illustrates an absorber with a bandgap, E_g, and with a trap level at an energy E_{T_1} below the conduction band edge. In this discussion, it will be assumed, without loss of generality, that $E_{\mathrm{T}_1} < E_g - E_{\mathrm{T}_1}$. Wolf explains that, resulting from this trap level, three distinct photo-induced electronic transitions are permissible [20]: between the conduction band and valence band, between the trap level and the conduction band, and between the trap level and the valence band. Wolf explains that a solar cell with an optimized three-transition absorber may more efficiently convert the broadband solar irradiance than other p-n junction solar cells.

Wolf calculates the maximum power density generated by the solar cell, $W\,|_{\mathrm{MP}}$, in terms

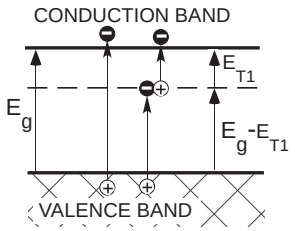

Figure 6: Reduced band diagram of an absorber with a single trap level located at an energy E_{T1} below the conduction band edge. The trap levels result in multiple photo-induced electronic transitions. One trap provides three distinct photo-induced electronic transitions. This figure is essentially that presented by Wolf in reference [20].

of the energy gap, E_g; a semi-empirical voltage factor, V.F., which is the ratio of the product of the elementary charge, q, and the open-circuit voltage to the energy gap; a semi-empirical curve factor, C.F., which is the ratio of the largest rectangle that can be inscribed into the current-voltage characteristic to the product of the short-circuit current and open-circuit voltage; and the light-generated current, I_L, as

$$\dot{W}\,|_{\mathrm{MP}} = (\mathrm{V.F.})\ (\mathrm{C.F.})\ (I_L)\ (E_g/q)\,. \tag{5}$$

Wolf explains that the voltage factor and curve factor both may be large, considering that these solar cells would have large bandgaps [20]. In addition, a large photo-generated current may also be obtained resulting from the absorption of both sub- and supra-bandgap photons [20].

The light-generated current is given in terms of the number of photons in the sun's spectrum per square meter per second available for transitions from the valence band to the conduction band, $\dot{N}_{\mathrm{p,(C,V)}}$; the number of photons in the sun's spectrum per square meter per second available for transitions from the trap level to the conduction band, $\dot{N}_{\mathrm{p,(C,T)}}$; and the number of photons in the sun's spectrum per square meter per second available for transitions from the valence band to the trap level, $\dot{N}_{\mathrm{p,(T,V)}}$, as

$$I_L = q\,\left[\dot{N}_{\mathrm{p,(C,V)}} + \min\left(\dot{N}_{\mathrm{p,(C,T)}}, \dot{N}_{\mathrm{p,(T,V)}}\right)\right]. \tag{6}$$

The generation rate of electronic charge is proportional to the sum of two numbers [20]: the number of transitions generated by a one-step process from the valence band to the

conduction band and the number of transitions generated by a two-step process from the valence band to the conduction band. Resulting from the two-step nature of the sub-bandgap transitions, the overall number of two-step transitions from the valence band to the conduction band is limited by the smaller of $\dot{N}_{\mathrm{p,(C,T)}}$ and $\dot{N}_{\mathrm{p,(T,V)}}$ [20].

The numbers of photons in the sun's spectrum per square meter per second available for each transition is given in terms of the absorptivity, $a_\gamma(\hbar\omega)$, and the emission spectrum of the sun, $\dot{n}_{\mathrm{S}}$, as

$$\dot{N}_{\mathrm{p,(C,V)}} = \int_{E_g}^{\infty} a_\gamma(\hbar\omega)\ \dot{n}_{\mathrm{S}}\ d\hbar\omega, \tag{7a}$$

$$\dot{N}_{\mathrm{p,(T,V)}} = \int_{E_g - E_{\mathrm{T}_1}}^{E_g} a_\gamma(\hbar\omega)\ \dot{n}_{\mathrm{S}}\ d\hbar\omega, \text{ and} \tag{7b}$$

$$\dot{N}_{\mathrm{p,(C,T)}} = \int_{E_{\mathrm{T}_1}}^{E_g - E_{\mathrm{T}_1}} a_\gamma(\hbar\omega)\ \dot{n}_{\mathrm{S}}\ d\hbar\omega; \tag{7c}$$

Given that the absorption coefficients relating to each transition are non-zero for all photons with energies $\hbar\omega$ greater than E_{T_1}, the absorber may absorb a photon with energy $\hbar\,\omega$ greater than the trap energy, E_{T_1} [20]. Additionally, if the trap level appropriately adjusts the absorption characteristic, then the absorption coefficient describing each of the transitions will be high [20]. In such case, the absorptivity will be unity and the absorber may completely absorb each photon that has an energy $\hbar\omega$ greater than E_{T_1}. Wolf notes that to ensure both of the sub-bandgap transitions, the number of filled trap states and the number of empty trap states must be of the same order of magnitude [20]. In other words, the three-transition absorber may be considered to be metallic [10]. Furthermore, Wolf notes that to maintain a high likelihood of a two-photon process, an absorber with a slow trap level is preferable to a fast trap level [20].

Wolf calculates an upper-efficiency limit of 51% for the three-transition solar cell [20]. Unlike Wolf's approach [20], the approach of Luque and Martí [35] gives the upper-efficiency limit of a three-transition solar cell, as there is no reference to any semi-empirical factors. In the paragraphs to follow, the present author reviews the particulars of the latter approach.

2.2.2 Detailed-Balance Approach of Luque and Martí

In 1997, Luque and Martí present a detailed-balance analysis of a three-transition solar cell [35]. Their work is novel because they derive the statistics of photons in equilibrium with the three allowed photo-induced electronic transitions of a three-transition absorber [35], use these statistics to write the photon fluxes emitted by the solar cell [35], and calculate the upper conversion efficiency of a three-transition solar cell.

Figure 7 gives the reduced band diagram of the absorber of an intermediate band solar cell, as posited by Luque and Martí. There, the electronic states between the conduction band and valence band form an intermediate band with infinitesimal band width. The energetic gap between the conduction band and valence band is $\varepsilon_{(\mathrm{C,V})}$. The bandgaps between the intermediate band and the other electronic bands are referenced from the center of the intermediate band. The bandgap between the intermediate band and conduction band is labeled $\varepsilon_{(\mathrm{C,I})}$ and the bandgap between the intermediate band and valence band is labeled $\varepsilon_{(\mathrm{I,V})}$. In this discussion it will be assumed, without loss of generality, that $\varepsilon_{(\mathrm{I,V})} < \varepsilon_{(\mathrm{C,I})}$. As explained by Shockley and Read, the electronic occupancy of the conduction band, intermediate band, and valence band are each described by unique quasi-Fermi levels [43]: $\varepsilon_{\mathrm{F,C}}$, $\varepsilon_{\mathrm{F,I}}$, and $\varepsilon_{\mathrm{F,V}}$, respectively. Meanwhile, the net photon flow absorbed, resulting from electronic transitions between band X and band Y, is the difference between the photon flow absorbed, $\dot{N}_{\mathrm{p,(X,Y)}}$, and the photon flow emitted, $\dot{N}_{\mathrm{s,(X,Y)}}$.

Allowing that all the electronic charges that are transfered to an external load pass through the conduction band and the valence band and allowing that the solar cell is in a steady-state condition, the net photon flow resulting from sub-bandgap absorption is in balance as [35]

$$\dot{N}_{\mathrm{p,(C,I)}} - \dot{N}_{\mathrm{s,(C,I)}} = \dot{N}_{\mathrm{p,(I,V)}} - \dot{N}_{\mathrm{s,(I,V)}}, \tag{8}$$

and the power density generated by the intermediate band solar cell, $\dot{W}$, is given as

$$\dot{W} = \frac{\varepsilon_{\mathrm{F,C}} - \varepsilon_{\mathrm{F,V}}}{q} \times q \left[\left(\dot{N}_{\mathrm{p,(C,V)}} - \dot{N}_{\mathrm{s,(C,V)}} \right) + \left(\dot{N}_{\mathrm{p,(C,I)}} - \dot{N}_{\mathrm{s,(C,I)}} \right) \right]. \tag{9}$$

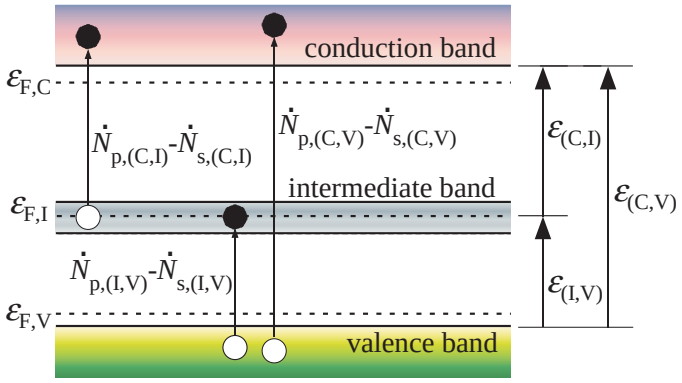

Figure 7: Reduced band diagram of an intermediate band absorber with an infinitesimal intermediate band width. Shown are energetic separations between electronic band X and electronic band Y, $\varepsilon_{(X,Y)}$; the quasi-Fermi level, $\varepsilon_{F,X}$, that describes the occupancy of band X; the photon flows absorbed that result from electronic transitions between band X and band Y, $\dot{N}_{p,(X,Y)}$; and the photon flows emitted that result from electronic transitions between band X and band Y, $\dot{N}_{s,(X,Y)}$;

Each of these photon flows may be given in terms of the Bose-Einstein integral

$$\dot{N}_{BE}\left(\varepsilon_i, \varepsilon_f, T, \mu\right) = \frac{1}{4\,\pi^3\,\hbar^3\,c^2} \int_{\varepsilon_i}^{\varepsilon_f} \frac{(\hbar\omega)^2\ d\hbar\omega}{\exp\left(\frac{\hbar\omega-\mu}{k\,T}\right)-1}, \text{ as} \tag{10}$$

$$\dot{N}_{p,(C,V)} = \dot{N}_{BE}\left(\varepsilon_{(C,V)}, \infty, 6000, 0\right), \tag{11a}$$

$$\dot{N}_{s,(C,V)} = \dot{N}_{BE}\left(\varepsilon_{(C,V)}, \infty, 300, \varepsilon_{F,C}-\varepsilon_{F,V}\right), \tag{11b}$$

$$\dot{N}_{p,(I,V)} = \dot{N}_{BE}\left(\varepsilon_{(I,V)}, \varepsilon_{(C,I)}, 6000, 0\right), \tag{11c}$$

$$\dot{N}_{s,(I,V)} = \dot{N}_{BE}\left(\varepsilon_{(I,V)}, \varepsilon_{(C,I)}, 300, \varepsilon_{F,I}-\varepsilon_{F,V}\right), \tag{11d}$$

$$\dot{N}_{p,(C,I)} = \dot{N}_{BE}\left(\varepsilon_{(C,I)}, \varepsilon_{(C,V)}, 6000, 0\right), \text{ and} \tag{11e}$$

$$\dot{N}_{s,(C,I)} = \dot{N}_{BE}\left(\varepsilon_{(C,I)}, \varepsilon_{(C,V)}, 300, \varepsilon_{F,C}-\varepsilon_{F,I}\right). \tag{11f}$$

The upper-efficiency limit of the three-transition solar cell at maximum power is found to be 63.2% [35]. This efficiency limit occurs when the conduction-to-valence bandgap is 1.95 eV, the conduction-to-intermediate bandgap is 1.24 eV, and the intermediate-to-valence bandgap is 0.71 eV [35]. By utilizing the general equivalent circuit of this solar cell, in the following subsection, the present author places this efficiency limit into the context of a tandem-stack of single-junction, single-transition solar cells.

2.2.3 General Equivalent Circuit

Figure 8 shows the reduced band diagram of a three-transition solar cell. As made implicit by Wolf [20] and made explicit by Luque and Martí [10], a three-transition solar cell is made by sandwiching the three-transition absorber between an n-type emitter on one side and a p-type emitter on the other side. Resulting from the n-type emitter, only electrons from the conduction band may pass through the n-type emitter. Similarly, resulting from the p-type emitter, only holes from the valence band may pass through the p-type emitter [35]. These electronic currents may then pass through an external load via external contacts to the emitters. The upper efficiency limit of the three-transition solar cell (63.2% [35]) may be understood by considering its general equivalent circuit [39, 36, 40, 41].

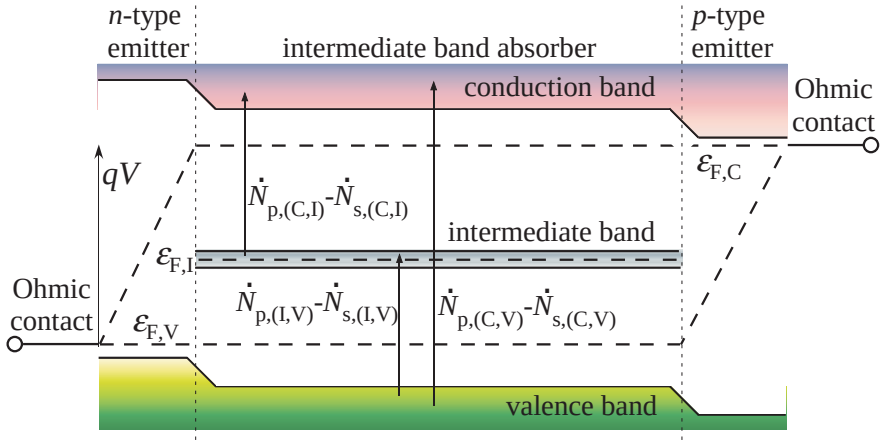

Figure 8: Sketch of a three-transition solar cell. Shown is the absorber sandwiched between n- and p-type emitters, Ohmic contacts to the emitters, and a voltage, V, across the solar cell.

As shown in Figure 9, the equivalent circuit of a three-transition solar cell is composed of three photodiodes. Two of the photodiodes are electrically connected in a series string. The third photodiode is connected in parallel to the series-connected photodiodes. Each of the photodiodes passes a light-generated current density, $J_{p,(\mathrm{X,Y})} = q \times \dot{N}_{p,(\mathrm{X,Y})}$, and a recombination current, $J_{s,(\mathrm{X,Y})} = q \times \dot{N}_{s,(\mathrm{X,Y})}$. Resulting from the series connection, the net current density generated by each of the series-connected photodiodes must be in balance. Further, resulting from the parallel connection, the voltage across the two series-connected

photodiodes is equal to the voltage across the photodiode in parallel with them.

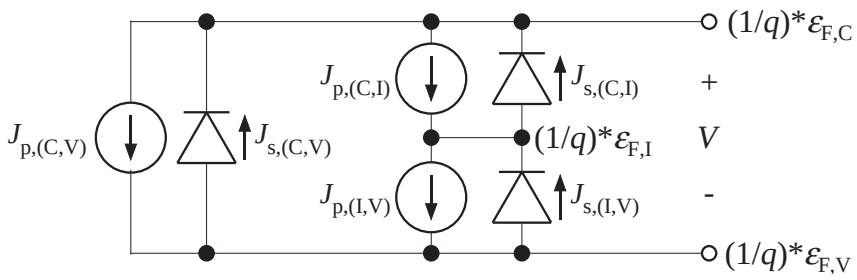

Figure 9: Equivalent circuit diagram of a three-transition solar cell. Shown are three diodes, each of which pass a recombination current density, $J_{p,(X,Y)}$, and three current sources, each of which pass a light-generated current density, $J_{s,(X,Y)}$. The voltage at each of the three nodes is labeled in terms of a quasi-Fermi level. The voltage, V, across the device is shown.

The general equivalent circuit of the three-transition solar cell is the same as that of the series-parallel solar cell [42]. Resulting from its two constraints (one current constraint and one voltage constraint), the efficiency limit of the three-transition solar cell (63.2%) is upper bounded by that of a tandem-stack of three electrically-unconstrained single-junction, single-transition solar cells (63.8% see Table 2 on page 14). Of particular note, the ideal series-parallel solar cell is more spectrally robust than an ideal tandem-stack of three solar cells electrically assembled in series [42]. One may project that (a) because the general equivalent circuit of the three-transition solar cell is the same as the general equivalent circuit of the series-parallel solar cell, that (b) the ideal three-transition solar cell is similarly more spectrally robust than an ideal tandem-stack of three solar cells electrically assembled in series.

2.2.4 Finite-Bandwidth Analysis of Levy and Honsberg

Unlike previous analyses [20, 35], Levy and Honsberg [44, 13, 37] analyze the maximum power performance of three-transition solar cells where the electronic levels between the conduction band and valence band form an intermediate band of finite width (see the right pane of Figure 10). The work of Levy and Honsberg is novel in quantifying the impact of both finite intermediate band width and spectral selectivity on the optimized detailed-balance conversion efficiencies of the three-transition solar cell and its associated band structure [37].

The inclusion of finite intermediate bandwidths is important whether the three-transition absorber is formed with dopants [45] or with alloys [46, 47, 48, 49, 50, 51]. Candidate alloys show intermediate band widths of order 100 meV [48, 49, 51] or 1 eV [46, 47, 50] . Levy and Honsberg conclude that the largest efficiencies result when the intermediate band's width is roughly equal to or less than 800 meV [37]. For example, when the width of the intermediate band equals 800 meV, the first-law efficiencies reach 57.9% and 33.9% (compared with 63.2% and 36.3% when the intermediate band's width is infinitesimally small) for fully-concentrated and non-concentrated solar illumination, respectively. According to Levy and Honsberg, when the intermediate band's width is roughly less than or equal to 800 meV, to achieve high efficiencies at large concentrations, the smallest and next smallest bandgap ought to be roughly 100 meV smaller and 400-500 meV larger than 800 meV, respectively [37]. In the following subsection, the present author offers concluding remarks regarding the operation and potential performance of the three-transition solar cell.

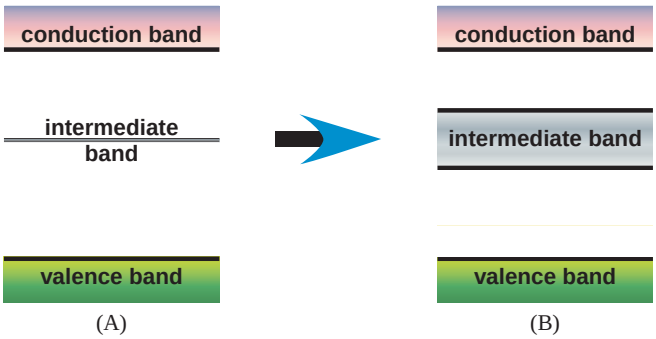

Figure 10: Reduced band diagram of a three-transition absorber whose electronic states between those of the conduction and valence bands form an intermediate band with infinitesimal width (pane A) or finite width (pane B). The work of Levy and Honsberg [37] moves from the analysis of highly idealized structures with infinitesimal intermediate band widths to more realistic structures with finite intermediate band widths, while maintaining the detailed-balance framework.

2.2.5 Conclusions

In this section the present author reviews the origin and history of the theory pertaining to the theoretical operation and performance of the three-transition solar cell. Similar to a tandem-stack of three solar cells electrically assembled by a combined series/parallel interconnect [42], the efficiency limit of the three-transition solar cell is 63.2%. The present

author draws two conclusions pertaining to the merit of the three-transition solar cell as an approach to high efficiency solar energy conversion. (*i*) First, the three-transition solar cell is attractive because it provides a significant efficiency enhancement per solar cell operating in tandem. For example, a single three-transition solar cell may nearly reach the efficiency limit of a tandem-stack of three single-junction, single-transition solar cells. Moreover, a tandem-stack of two three-transition solar cell may nearly reach the efficiency limit of a tandem-stack of six single-junction, single-transition solar cells. (*ii*) Second, an idealized three-transition solar cell may be more spectrally robust than an idealized tandem-stack of three solar cells electrically assembled in series. Thus, whether the absolute optimum band structure may or may not be practically obtainable, the efficiency will degrade gently as the band structure deviates from the optimum band structure.

In practice, realizing a three-transition solar cell presents many technological hurdles. The central impediment to realize a three-transition solar cell is fabricating a three-transition absorber. In the following section, the present author reviews proposals to realize a three-transition absorber.

2.3 Realization of a Three-Transition Absorber and Solar Cell

There are several proposals regarding the realization of a three-transition solar cell. The various proposals are at different stages of their development; some have prototypes while others do not. Each proposal may be distinguished by its respective approach to synthesize the three-transition absorber: a medium with intermediate levels that are electronically isolated from both the conduction and valence bands. Proposed approaches to realize a three-transition absorber include the following: (1) where the intermediate levels are those of localized states of dopants introduced into a host semiconductor, (2) where the intermediate levels are those that comprise subbands introduced by quantum-well heterojunctions, (3) where the intermediate levels are those that comprise a miniband introduced by quantum-dot heterojunctions, and (4) where the intermediate levels are those of extended states of dopants introduced into a host semiconductor. The present author briefly reviews these proposals in sections 2.3.1, 2.3.2, 2.3.3, and 2.3.4, respectively. The present author

concludes in section 2.3.5 that, although in some instances these proposals yield a relative efficiency enchantment, there is no experimental evidence of a global efficiency enhancement. Before continuing, it is worth noting that Reynolds and Czyzak are the first to postulate an absorbing medium with a band of electronic states that is electronically isolated from both the conduction band and valence band. They postulate this as a mechanism for both photovoltaic and photoconductive effects in CdS crystals [52].

2.3.1 Localized-States Approach

Wolf states the connection between (a) the required physical properties of the intermediate levels needed to realize the three-transition absorber and (b) the absorption resulting from localized centers [20]. This connection has spawned a branch of photovoltaics called impurity photovoltaics [53]. There are two reports of relative efficiency enhancements [26] via the use of impurity photovoltaics as compared to reference solar cells. Bruns *et al.* illustrate that a solar cell implanted with helium dose of 2×10^{16} cm^{-2} yields a 5% efficiency enhancement as compared to a reference solar cell [54]. Further, Kasai *et al.* illustrate that a indium-implanted crystalline silicon solar cell yields a 11% efficiency enhancement as compared to a reference solar cell (7.85% versus 7.09%) [55]. That said, at the time that this present disseration is written, no global efficiency enhancement is experimentally observed in solar cells intending to utilize the impurity-photovoltaic effect.

2.3.2 Quantum-Well Approach

Bremner *et al.* [56] and Green [57] illustrate the connection between quantum-well hetero-junctions and the realization of a three-transition solar cell. Bremner *et al.* [56] consider that the occupancy of electrons and holes in the quantum confined region are each described by two distinct quasi-Fermi levels. Thus, one single quasi-Fermi level variation exists in the quantum confined region. Similarly, Bremner *et al.* [56] consider that the occupancy of electrons and holes in the barrier region are each described by two distinct quasi-Fermi levels. Thus, one single quasi-Fermi level variation exists in the barrier region. In their description, at the junction between the confining material and the barrier material, there is a step in the quasi-Fermi levels describing the occupancy of electrons [56]. However, at

the junction between the confining material and the barrier material, there is no step in the quasi-Fermi levels describing the occupancy of holes [56]. Having constructed a system with three photo-induced electronic transitions, and with three quasi-Fermi levels, Bremner *et al.* calculate an upper efficiency limit of 64% for the quantum well solar cell [56]. In 1991 Barnham *et al.* illustrate up to a 10% efficiency enhancement in GaAs/AlGaAs *p-i-n* multi-quantum-well structures [58] relative to control solar cells. That said, at the time that this present disseration is written, no global efficiency enhancement is experimentally observed in quantum-well solar cells.

2.3.3 Quantum-Dot Approach

Nanostructured quantum-dot heterojunctions are proposed to implement a three-transition solar cell [59, 60, 61]. In this approach, the electronic states of the intermediate band are introduced into the previously forbidden bandgap of a host semiconductor by the three-dimensional confining potential created by quantum-dot heterojunctions. Three-transition solar cells implemented with this proposed approach are most often referred to as quantum-dot intermediate-band solar cells (QD IBSC) [59, 60, 61].

In the initial proposal of the quantum dot solar cell, it is suggested that InGaAs/AlGaAs quantum-dot heterojunctions grown on GaAs substrates may be used to synthesize the appropriate absorber [59]. Contrary to the initial proposal, experimental prototypes include the following heterojunctions: InAs/GaAs [41, 62, 63, 64] and InGaAs/GaAs [65], both grown on GaAs substrates. These material systems (*i.e.*, InGaAs/AlGaAs on GaAs substrates, InAs/GaAs on GaAs substrates, and InGaAs/GaAs GaAs substrates) have two characteristics limiting their usage for development of a QD IBSC [66]: they have valence band discontinuities and they accumulate strain. Levy and Honsberg identify absorbers for multiple transition solar cells that are implemented with nanostructured heterojunctions [66]. Their technical approach introduces a novel design rule that mandates a negligible valence band discontinuity between the barrier material and confined materials [66]. Another key design rule stipulates that the substrate have a lattice constant in between that of the barrier material and that of the quantum confined material, which permits

strain compensation [66]. Four candidate materials systems (confined/barrier/substrate) are identified: $InP_{0.85}Sb_{0.15}$/GaAs/InP, $InAs_{0.40}P_{0.60}$/GaAs/InP, InAs/$GaAs_{0.88}Sb_{0.12}$/InP, and InP/$GaAs_{0.70}P_{0.30}$/GaAs [66].

QD IBSC experimental prototypes include absorbers composed of InAs/GaAs heterojunctions [41, 62, 63, 64] and InGaAs/GaAs heterojunctions [65]. At the time that this present disseration is written, all prototype quantum-dot solar cells show a deteriorated efficiency as compared to a control solar cell fabricated without quantum dots [41, 65, 63, 67]. Thus, at the time that this present disseration is written, no global efficiency enhancement is experimentally observed in quantum-dot solar cells.

2.3.4 Extended-States Approach

The last proposed approach to fabricate a three-transition absorber involves the synthesis of alloys derived from host semi-conductors. In these proposals, the intermediate states are those of the extended states of dopants introduced into the host-semiconductor. The majority of these proposals [46, 68, 69, 70, 50, 71, 72, 73] are based on first-principle theoretical calculations using a periodic density functional theoretic approach [74, 75, 76]. However, other proposals [48, 77, 78] are explained by the band anti-crossing model [79, 80, 81, 82]. Of all these proposals, only two absorbers with a band of intermediate states are experimentally synthesized: $Zn_{1-y}Mn_yO_xTe_{1-x}$ alloys [48, 77] and $GaN_xAs_{1-y}P_y$ alloys [78]. At the time that this present disseration is written, these absorbers have not been processed into solar cells. Thus, no global efficiency enhancement is experimentally observed by using this proposed approach.

2.3.5 Conclusions

In this section, Section 2.3, the present author reviews four proposed approaches to realize a three-transition solar cell. In some instances, the proposed approaches yield a relative efficiency enhancement with respect to a control solar cell. This is the case for impurity-effect photovoltaic solar cells [54, 55], and quantum-well solar cells [58]. However, the demonstration of a global efficiency enhancement is absent from the literature. In the following section, the present author reviews experimental work on multiple transition solar

cells. The aim of much of the experimental work is to verify the key precepts on which the theorized global efficiency enhancement depends.

2.4 Experimentation to Confirm the Precepts of the Three-Transition Solar Cell

There are several theoretical precepts on which the global efficiency enhancement of the three-transition solar cell relies. Considering that the global efficiency enhancement of the three-transition solar cell is not yet experimentally demonstrated, it is of acute importance to experimentally verify these precepts one by one. In some cases, the verification requires the use of one apparatus (*e.g.* the use of a spectrophotometer to measure the absorptance) and in some cases, verification requires the use of several apparati combined with the use physical models (*e.g.* the use of a electroluminescence spectra and quantum efficiency measurements to determine the extent of quasi-Fermi level splitting). Depending on the precept, experimental data exists for one or more of the four proposed approaches to synthesize the three-transition absorber (*i.e.* localized states of dopants, subbands introduced by quantum-well heterojunctions, the intermediate states introduced by quantum-dot heterojunctions, and extended states of dopants). In section 2.4.1, the present author outlines the precepts on which the global efficiency enhancement of the three-transition solar cell relies. The subsequent six subsections are summaries of experimental evidence utilized to analyze whether or not these precepts are verified and to what extent. In section 2.4.2, the present author analyzes the extent to which the absorption characteristic of prototypes three-transition solar cells matches the hypothesized absorption characteristic of theorized three-transition solar cells. In section 2.4.3, the present author analyzes the extent to which the emission characteristic of prototypes three-transition solar cells matches the hypothesized emission characteristic of theorized three-transition solar cells. In section 2.4.4, the present author analyzes the extent to which the collection of electron-hole pairs in prototypes three-transition solar cells matches the hypothesized collection of theorized three-transition solar cells. In section 2.4.5 , the present author analyzes the extent to which the generation of charge current in prototypes three-transition solar cells matches the hypothesized generation of charge current theorized three-transition solar cells. In section 2.4.5 , the present

author analyzes the extent to which the generation of charge current under broadband illumination in prototypes three-transition solar cells matches the hypothesized generation of charge current theorized three-transition solar cells. In section 2.4.6 , the present author analyzes the extent to which the voltage factor under broadband illumination in prototypes three-transition solar cells matches the hypothesized voltage factor of charge current theorized three-transition solar cells. In section 2.4.7 , the present author analyzes the extent to which the separation of more than two quasi-Fermi levels is demonstrated in prototypes three-transitions solar cells. Finally, in section 2.4.8, the present author concludes that, at the time that this disseration is published, a body of experimental evidence to irrefutably confirm the existence of either a three-transition absorber or a three-transition solar cell is absent from the literature. The present author further concludes that, in order to substantiate these claims, the set of experimental methods applied to prototype three-transition solar cells must be extended, so that both the absorption and emission of photons in the infrared regime of the electromagnetic spectrum may be recorded.

The present author now continues to outline the precepts of the three-transition solar cell.

2.4.1 Itemization of Three-Transition Solar Cell Precepts

The global efficiency enhancement of a three-transition solar cell is predicated on several central precepts and several supporting conditions. The present author first itemizes the central precepts and then itemizes the supporting conditions.

The present author now outlines the six central precepts on which the capability of global efficiency enhancement is made possible. These central precepts include that:

- the absorption of photons results from three distinct radiatively-coupled interband electronic transitions [20],
- the emission of photons results from three distinct radiatively-coupled interband electronic transitions [41, 83],
- the collection of electron-hole pairs results from each of these three radiatively-coupled

absorption events,

- the generation of a large charge current results from the absorption of broadband illumination [20, 83, 62],
- the demonstration of a large voltage factor results from the absorption of broadband illumination [20, 83], and,
- the distribution of carriers in each of the three electronic bands is described by three distinct quasi-Fermi levels when in non-equilibrium conditions [35].

The list above contains the precepts that are absolutely necessary to achieve a global efficiency enhancement. However, the list above is not sufficient to achieve the efficiency limit of a three-transition solar cell. In fact, several other conditions are required to achieve the efficiency limit.

The present author now outlines four additional conditions that may guarantee a global efficiency enhancement and, more specifically, guarantee an efficiency near to the limiting efficiency of the three-transition solar cell. These conditions are that:

- the absorption characteristic is such that the absorption coefficient relating to each of the three radiatively-coupled electronic transitions is high for all photons greater than the smallest energetic gap between two electronic bands [20],
- the absorption characteristic is such that absorption overlap with respect to the absorption coefficients of any two radiatively-coupled transitions is minimal [84],
- the occupation of the intermediate states under broadband irradiance is such that the number of filled intermediate states and the number of empty intermediate states are of the same order of magnitude [20, 10], and,
- the recombination rate resulting from non-radiative events between any two electronic bands is "slow" rather than "fast" [20]. (This will have a significant impact on the voltage factor.)

Based on the fact that a global efficiency enhancement is not experimentally demonstrated in prototype three-transition solar cells, it is of importance to verify each of these precepts and these conditions in prototypes solar cells.

Having itemized the central precepts and additional conditions on which the potential for a global efficiency enhancement of the three-transition solar cell is premised, the present author now reviews experimental studies on prototype three-transition solar cells that relate to the first of these fundamental precepts: those studies that relate to the absorption of photons.

2.4.2 Absorption of Photons

One of the central precepts of the three-transition solar cell is that the introduction of intermediate states may adjust the absorption characteristic so that the absorption coefficient describing each electronic transition is high [20]. This precept may be demonstrated by measuring the optical absorption absolutely or by measuring the optical structure with modulation techniques. The literature includes absorption measurements for two classes of prototype three-transition solar cells: those with states intending to yield an impurity-photovoltaic effect [85] and those with states intending to yield a band of extended states [48, 86, 77, 78]. The present author will now discuss the two approaches of measuring the absorption characteristics.

The absorption characteristic of an absorber may be significantly altered via the introduction of intermediate states. This may be demonstrated by measuring the absolute reflectance [87] and absolute transmittance [87] before and after the introduction of the intermediate states and comparing the respective absorptance spectra (absorptance = 1 - transmittance - reflectance). A perfect demonstration would show that (a) the absorptance of the sample with intermediate states has an onset that is much lower than the onset of the sample without intermediate states (*i.e.*, photons with lower energies are absorbed in a sample with the intermediate states as compared to a control sample without the intermediate states) and (b) the absorptance of the sample with intermediate states is equal to or nearly equal to unity over the entire domain that its absorptance is non-zero. Though

the absorption characteristic may be modified by the introduction of intermediate states, in some instances the observation of a change in the absolute absorptance may be somewhat obscured. In such cases, the use of modulation techniques [88, 89, 90] may be used to determine the change in the dielectric constant. An indication of the correct synthesis of a three-transition absorber would be the presence of three abrupt changes in the measured modulated spectra. Each of these three abrupt changes corresponds to one of the energetic gaps of the three-transition absorber (see Figure 6 and Figure 7). The present author now reviews experimental results of prototype three-transition absorbers.

Absolute absorptance is measured by Zundel *et al.* in solar cells intending to use localized states to implement a three-transition solar cell [85]. Zundel *et al.* show that the absorptance spectra of proton-implanted solar cells and control solar cells are the same (within the bounds of experimental error) for photons with energies in the range of 0.49 eV to 6 eV. Photomodulated reflectance is measured in prototype three-transition absorbers [48, 86, 77, 78]. Using photomodulated reflectance spectroscopy, Yu *et al.* [48, 86] and Walukiewicz *et al.* [77] illustrate the onset of two band-to-band optical transitions in $Zn_{0.88}Mn_{0.12}Te$: one at 1.8 eV and the other at 2.6 eV. Similarly, Yu *et al.* illustrate the onset of two band-to-band optical transitions in $Cd_{0.88}ZnOTe_{0.12}Te$: one at 1.7 eV and the other at 2.5 eV [86]. Finally, Yu *et al.* use photomodulated reflectance spectroscopy, to illustrate the onset of two band-to-band optical transitions in GaNAsP quaternary alloys [78]. By comparing several samples with distinct molar concentrations of phosphorus, Yu *et al.* show that these two onsets increase as the molar concentration of phosphorus increases. The present author now summarizes these findings and draws one conclusion.

The global efficiency enhancement of the three-transition solar cell relies on the premise that the introduction of intermediate states may adjust the absorption characteristic so that the absorption coefficient describing each electronic transitions is high [20]. The introduction of intermediate states is experimentally demonstrated to alter the absorption characteristic in several prototype three-transition absorbers [48, 86, 77, 78]. Using direct experimental measurements, the authors of references [48, 86, 77, 78] only illustrate two of the three absorption onsets that are required of a three-transition absorber. The third

onset, which would be detected in the infrared regime of the electromagnetic spectrum, is assumed to exist without the support of direct experimental observation. Based on the experimental data reviewed in this section, Section 2.4.2, the present author concludes that (*i*) the literature contains only a weak proof of the existence of a three-transition absorber and (*ii*) a stronger proof would require the direct experimental observation of an absorption onset in the infrared regime. In the next section, section 2.4.4, the present author reviews experimental results regarding the emission of photons by prototype three-transition solar cells.

2.4.3 Emission of Photons

One of the central precepts of the three-transition solar cell is that the introduction of intermediate states may adjust the absorption characteristic so that the absorption coefficient describing each electronic transition is high [20]. This precept may be demonstrated by measuring the optical luminescent emission spectra of prototype three-transition solar cells [41, 83]. The literature includes experimental measurements for two classes of prototype three-transition solar cells. In section 2.4.3.1, the present author hypothesizes the expected results of these measurements when performed on a three-transition solar cell. In section 2.4.3.2, the present author reviews existing experimental results for prototypes where the intermediate levels are introduced by quantum wells [58, 91, 92, 93, 94]. In section 2.4.3.3, the present author reviews existing experimental results for prototypes where the intermediate levels are introduced by quantum dots [41, 62, 63, 95, 65, 67]. In section 2.4.3.4, the present author presents a comparative analysis with concluding remarks based on these experimental results. The expected results of these measurements are now discussed by the present author.

2.4.3.1 Hypothesized Results

The luminescent emission spectra from three-transition absorbers and three-transition solar cells are hypothesized to be characterized by significant emission within three distinct spectral bands [41, 83]. Each of these three distinct spectral bands corresponds to one of the

three interband electronic transitions within the three-transition absorber [41, 83]. Moreover, a spectral band will be observed at photon energies near to the minimum energetic gap that separates each of absorber's three electronic bands [41, 83]

Ekins-Daukes, Honsberg and Yamaguchi propose four photoluminescent tests to determine whether the required optical coupling exists, the relative strengths of the coupling, and whether the intermediate is electronically isolated from both the conduction band and valence band [83]. The most rudimentary of these test involves the use of standard non-contact photoluminescence spectroscopy with a laser source whose emission wavelength is low enough to induce all three interband electronic transitions. The resultant optical spectra may be compared with the luminescent signature of a three-transition absorbers with an idealized absorptance (see pane (A) of Figure 11). Proof-positive results would reveal luminescence in three well-separated spectral bands: one band for each of the three interband electronic transitions [41, 83]. Each of these bands would exist near to the minimum energetic gaps separating each of the three electronic bands comprising the three-transition absorber [41, 83]

Levy, Ekins-Daukes, and Honsberg also present theoretical photoluminescent spectra of three-transition absorbers [98]. The novelty of their work lies in illustrating the spectroscopic consequences of multi-gap absorbers whose quantum states form parabolic bands [98] (see pane (B) of Figure 11). Levy *et al.* conclude that the photoluminescent intensity of a three-transition absorber may be apparent within four distinct and well-separated spectral bands [98]. The fourth spectral band, which is not visible in the spectrum illustrated in pane (B) of Figure 11, is related to photo-induced intraband electronic transitions and appears in the far-infrared regime of the electromagnetic spectrum. One additional spectroscopic consequence of the parabolic-band approximations is that the photon energy associated with the peak of each spectral band occurs at a slightly higher energy than the photon energy associated with the luminescence onset of the same spectral band. Thus, the photon energy at which a peak is observed is larger than the minimum energetic gap between the corresponding electronic bands (see pane (B) of Figure 11). The present author now reviews existing experimental results relating to the emission of photons from prototype

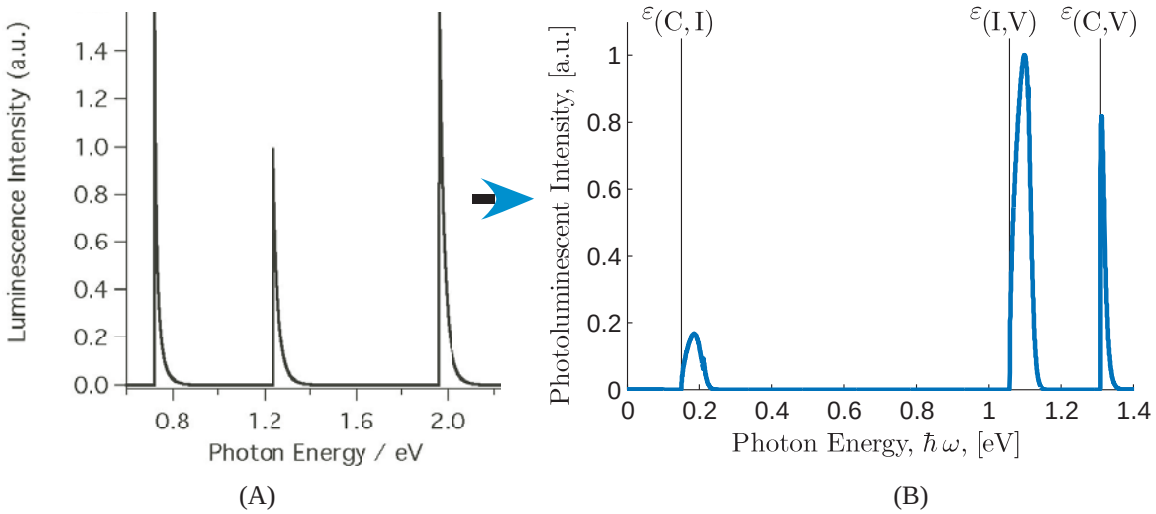

Figure 11: Photoluminescence spectra of idealized three-transition absorbers. (A) Photoluminescence spectra of three-transition absorber with a semi-infinite length and idealized absorptance. For this example, the bandgap $\varepsilon_{(\mathrm{I,V})} = 0.7$ eV, the bandgap $\varepsilon_{(\mathrm{C,I})} = 1.24$ eV, and the bandgap $\varepsilon_{(\mathrm{C,V})} = 1.95$ eV. The onsets of each spectral band occur at one of these three energies. Figure taken from reference [83]. (B) Photoluminescence spectra of a three-transition absorber of finite length and with absorption coefficients derived from parabolic-band approximiations [96, 97]. For this example, the width of the intermediate band is 0.1 eV, the bandgap $\varepsilon_{(\mathrm{I,V})} = 1.05$ eV, the bandgap $\varepsilon_{(\mathrm{C,I})} = 0.15$ eV, and the bandgap $\varepsilon_{(\mathrm{C,V})} = 1.30$ eV. The onsets of each spectral band occur at one of these three energies.

three-transition absorbers and three-transition solar cells.

2.4.3.2 Quantum Well

Several authors measure the luminescent emission of photons from prototype three-transition solar cells implemented with quantum wells [99, 100, 101, 94, 102, 103, 104, 105]. Tsui *et al.* record the photoluminescence of GaAs/AlGaAs single-quantum-well *p-i-n* photodiodes [99]. Tsui *et al.*, observe luminescence in one spectral band located at roughly 1.5 eV in structures with a quantum well whose width is 140 Angstroms and in one spectral band around 1.6 eV in structures with a quantum well whose width is 50 Angstroms [99]. Meanwhile, several authors observe luminescence from GaAs/AlGaAs structures in one spectral band whose peak is roughly located at 1.43 eV [100, 101]. Further, Nelson *et al.* [100], Ekins-Daukes *et al.* [101], and Barnham *et al.* [94, 104], observe luminescence from InGaAs/GaAs structures in two spectral band whose peaks are roughly located at roughly 1.28 eV and 1.43 eV, respectively. Kluftinger *et al.* [102, 103] observe luminescent photon

emission from GaAs/AlGaAs asymmetrical double-quantum-well structures. Kluftinger *et al.* [102, 103] also illustrates photo-emission in one spectral band from the narrow quantum well and illustrate photo-emission in one spectral band from the wide quantum well. The emission peak in these spectral bands occurs at an energy of 1.45 eV in the wide quantum well and 1.65 eV in the narrow quantum well, respectively [102, 103]. In the next paragraph, the present author reviews results obtained from prototype three-transition solar cells implemented with quantum dots.

2.4.3.3 Quantum Dot

Several authors measure the photon emission from prototype three-transition solar cells implemented with quantum dots[41, 65, 62, 63]. Norman *et al.* record photoluminescence from InGaAs/GaAs structures [65]. They record emission within one spectral band located roughly between 1 eV (1240 nm) and 1.4 eV (890 nm) [65]. Luque *et al.* measure the luminescent emission of photons from prototype three-transitions solar cells implemented with InAs/GaAs quantum dot structures [41, 62, 63]. In all cases, the emission appears to derive from one spectral band. In one electroluminescence spectrum, the emission of photons are recorded in one broad spectral roughly between the wavelengths 850 nm (1.46 eV) and 1250 nm (990 meV) [41]. In all cases, the electroluminescence spectra is recorded in one broad spectral band. The spectral band begins at a wavelength of roughly 850 nm (1.46 eV) [41, 62, 63] and ends at a wavelength of roughly 1250 nm (990 meV) [41, 62] or 1400 nm (890 meV) [62, 63]. The present author now offers a comparative analysis of the emission of photons with respect to the various proposed approaches to realize a three-transition absorber and solar cell.

2.4.3.4 Comparitive Analysis

The global efficiency enhancement of the three-transition solar cell relies on the premise that the introduction of intermediate states may adjust the absorption characteristic so that the absorption coefficient describing each electronic transitions is high [20]. The introduction of intermediate states is, though experimentation, demonstrated to alter the emission characteristic in several prototype three-transition absorbers [99, 100, 101, 94,

102, 103, 104, 41, 65, 62, 63]. The measured spectra illustrate emission in one [99, 100, 101, 94, 102, 103, 104, 41, 65, 62, 63] spectral band, or two spectral bands [100, 101, 94, 104]. With respect to quantum-well prototypes, when there is emission from two distinct spectral bands [100, 101, 94, 104], one band relates to emission from the quantum well and the other from the barrier [106]. With respect to some quantum-dot prototypes, the emission of photons illustrate narrowly separated and overlapping peaks in one spectral band, rather than the luminescent signature of a three-transition absorber or solar cell. Based on the experimental data reviewed in this section, Section 2.4.3, the present author concludes that (*i*) the literature contains no proof of the existence of a three-transition absorber and (*ii*) a stronger proof would require the direct experimental observation of an emission onset in the infrared regime. In the next section, section 2.4.4, the present author reviews experimental results regarding the collection of charge current in prototype three-transition solar cells.

2.4.4 Collection of Electron-Hole Pairs

One of the central precepts of the three-transition solar cell is that once a photon is absorbed by any of the three inter-band electronic transitions, an electron-hole pair is collected in the form of a charge current. This precept may be demonstrated by several related experimental techniques: internal-quantum-efficiency measurements, external-quantum-efficiency measurements, and spectral-response measurements. The literature includes experimental measurements for three classes of prototype three-transition solar cells. In section 2.4.4.1, the present author hypothesizes the expected results of these measurements when performed on a three-transition solar cell. In section 2.4.4.2, the present author reviews existing experimental results for prototypes where the intermediate levels are introduced by localized states [107, 54, 108, 109, 55]. In section 2.4.4.3, the present author reviews existing experimental results for prototypes where the intermediate levels are introduced by quantum wells [58, 91, 92, 93, 94]. In section 2.4.4.4, the present author reviews existing experimental results for prototypes where the intermediate levels are introduced by quantum dots [41, 62, 63, 95, 65, 67]. In section 2.4.4.5, the present author presents a comparative analysis with concluding remarks based on these experimental results. The expected results

of these measurements are now discussed by the present author.

2.4.4.1 Hypothesized Results

The quantum efficiency of an absorber is the ratio of induced current density to the incident photon flux. In solar energy research, a quantum efficiency spectra is obtained by repeatedly measuring the quantum efficiency of an absorber under monochromatic radiation, except that for each measurement, the wavelength of the incident radiation is altered. As applied to prototype three-transition solar cells, it is important to distinguish the quantum efficiencies for photons greater than its absorber's largest energetic gap from the quantum efficiencies for photons less than its absorber's largest energetic gap but greater than the absorber's smallest energetic gap (see Figure 6 on page 22 or Figure 7 on page 25).

Attention is now turned to photons with energies in the range $(\hbar\omega, \hbar\omega + d\hbar\omega)$ where $\hbar\omega$ is greater than the largest energetic gap in the solar cell. A positive quantum efficiency indicates that the absorptivity, $a_\gamma(\hbar\omega)$ (see equation (7) on page 23), is non-zero. In addition, the nearer to unity the quantum efficiencies, the better. This is because it is more likely that the electron-hole pairs are extracted before they recombine resulting from non-radiative mechanisms.

Attention is now turned to photons with energies in the range $(\hbar\omega, \hbar\omega + d\hbar\omega)$ where $\hbar\omega$ is less than the largest energetic gap in the solar cell and greater than the smallest energetic gap in the solar cell. If the quantum efficiencies are non-zero, then this would be an indication that the three-transition solar cell may yield very large solar energy conversion efficiencies. Further, the nearer to unity that these measurements are, the more likely it is that the three-transitions solar cell may yield very large solar energy conversion efficiencies. However, if the measured quantum efficiencies are near to or exactly null, then this does not conclusively indicate that the device would not yield large solar energy conversion efficiencies. In fact, there are three possibilities that need to be considered. First, it may indicate that the absorptivity, $a_\gamma(\hbar\omega)$, is zero, which would deter large solar energy conversion efficiencies. Second, it may indicate that $a_\gamma(\hbar\omega)$ is non-zero and that the radiative processes act to balance the absorption with the emission of photons. In such case there

is no net conversion of the incident photon to a charge current, yet the device may still operate as an efficient three-transition solar cell. Third, it may indicate that $a_\gamma(\hbar\omega)$ is non-zero and non-radiative recombination act to balance the generation with the recombination of charge. In such case, there is no net conversion of the incident photon to a charge current. Furthermore, the device is unlikely to operate as an efficient three-transition solar cell. The present author now reviews existing experimental results for prototypes where the intermediate levels are introduced by localized states.

2.4.4.2 Localized States

Several authors report enhanced quantum efficiencies in solar cells with deep impurities as compared to their respective control solar cells [107, 54, 108, 109, 55]. Summonte *et al.* illustrate that helium-implanted solar cells show both an improvement in light-induced generation and up to a 10% enhancement in quantum efficiency in the red side of spectrum [107]. Bruns *et al.* illustrate that helium-implanted solar cells show up to a 10% improvement in the spectral response for both sub- and supra-bandgap photons [54]. Keevers *et al.* [108] and Kasai *et al.* [109, 55] illustrate that indium incorporated into solar cells demonstrate enhanced photoresponse in the infrared. Kasai *et al.* also illustrate an enhanced photoresponse for supraband gap photons as well [109, 55]. In the next paragraph, the present author reviews the results obtained from three-transition solar cells implemented with quantum wells.

2.4.4.3 Quantum Well

The present author now summarizes experimental observations of the collection of photogenerated charges in quantum-well solar cells. The present author first summarizes results for photons with energies less than the bandgap of the barrier material of the quantum-well solar cell, and then summarizes results for photons with energies greater than the bandgap of the barrier material of the quantum-well solar cell.

With respect to photons with energies less than the bandgap of the barrier materials, several authors report enhanced quantum efficiencies in quantum-well solar cells as compared to their respective control solar cells that are fabricated with the respective barrier

material of the quantum-well solar cells [58, 91, 92, 93, 94]. Barnham *et al.* [58] illustrate this in GaAs/AlGaAs *p-i-n* multiple-quantum-well structures; Ragay *et al.* [91] and Ekins-Daukes *et al.* [92] illustrate this in InGaAs/GaAs *p-i-n* multiple-quantum-well structures; and Ekins-Dakes *et al.* [93] and Barnham *et al.* [94] illustrate this in strain-balanced multiple-quantum-well InGaAs/GaAsP *p-i-n* structures.

With respect to photons with energies greater than the bandgap of the barrier materials, the results of quantum-efficiency measurements of quantum-well solar cells vary greatly as compared to the quantum efficiencies of their respective control solar cells that are fabricated with the respective barrier material of the quantum-well solar cells. Ragay *et al.* [91], Ekins-Dakes *et al.* [93, 92], and Barnham *et al.* [94] all illustrate multiple-quantum-well structures whose quantum efficiencies are either enhanced or reduced - depending on the exact energy of the photon being considered. Ragay *et al.* [91] and Barnham *et al.* [104] illustrate multiple-quantum-well structures whose quantum efficiencies are always diminished. Barnham *et al.* illustrate multiple-quantum-well structures whose quantum efficiencies are roughly unaltered [104]. In the next paragraph, the present author reviews the results obtained from three-transition solar cells implemented with quantum dots.

2.4.4.4 Quantum Dot

The present author now summarizes experimental observations of the collection of photo-generated charges in quantum-dot solar cells. The present author first summarizes results for photons with energies less than the bandgap of the barrier material of the quantum-well solar cell, and then summarizes results for photons with energies greater than the bandgap of the barrier material of the quantum-dot solar cell.

With respect to photons with energies less than the bandgap of the barrier materials, several authors report enhanced quantum efficiencies in quantum-dot solar cells as compared to their respective control solar cells that are fabricated with the respective barrier material of the quantum-dot solar cells [41, 62, 63, 95, 65]. Luque *et al.* [41, 62, 63] and Lopez *et al.* [95] illustrate this in InAs/GaAs *p-i-n* multilayer quantum-dot structures, while Norman *et al.* [65] illustrate this in InGaAs/GaAs *p-i-n* multilayer quantum-dot structures. In some

cases, experimental results indicate that as the number of multilayers increases to fifty layers, the subbandgap response increases as well [65], while in other cases, this monotonic trend is absent [95, 67].

With respect to photons with energies greater than the bandgap of the barrier materials, several authors report reduced [65, 67] or comparable [41, 62, 65, 63] quantum efficiencies in quantum-dot solar cells, as compared to their respective control solar cells, which are fabricated with the barrier material of the respective quantum-dot solar cells. From a comparison of multilayer samples with and without silicon doping, Norman *et al.* infer that the cause of the reduced external quantum efficiency is related to the silicon doping [65]. Martí *et al.* explain this same phenomena in terms of a diminishing charge current generated by the *p*-type emitter, which is caused by an increasing number of dislocations that propagate toward the *p*-type emitter from the quantum dot region [67]. The present author now offers a comparative analysis of the collection of charge current with respect to the various proposed approaches to realize a three-transition solar cell.

2.4.4.5 Comparitive Analysis

The present author observes three trends in the summary of experimental data reviewed in section 2.4.4. First, prototype three-transition solar cells exhibit the collection of charge carriers resulting from the absorption of photons with energies less than the bandgap of their respective host semiconductors [58, 91, 92, 93, 94, 41, 62, 63, 95, 65]. Second, each prototype three-transition solar cell yields greater collection efficiencies for photons with energies larger than the bandgap of the host semiconductor as compared to the collection efficiencies for photons with energies smaller than the bandgap of the host semiconductor [107, 54, 55, 58, 94, 104, 105, 91, 92, 93, 41, 62, 63, 95, 65]. Third, depending on the details, the collection of carriers resulting from the absorption of supra-bandgap photons may be diminished, enhanced, or unaltered as compared to their respective control solar cells. The global efficiency enhancement of a three-transition solar cell depends on the precept that once a photon is absorbed by any of the three inter-band electronic transitions,

an electron-hole pair is collected in the form of a charge current. The present author concludes that measured quantum efficiency spectra of prototype three-transition solar cells do not conclusively demonstrate that these prototypes are, in fact, three-transition solar cells. This is because an induced charge current is not demonstrated for photons with energies less than a few 100 meV less than the largest energetic gap in the system. In the following section, section 2.4.5, the present author reviews the experimental results of prototype three-transition solar cells under broadband illumination.

2.4.5 Generation of Charge Current

One of the central precepts of the three-transition solar cell is that, compared to a single p-n junction solar cell, a larger portion of the broadband solar spectrum may be absorbed so that a larger light-generated current is produced [20, 83, 62]. This precept may be demonstrated by first measuring the short-circuit of the prototype solar cell when irradiated by a broadband source of illumination and then by comparing the value of the short-circuit current to the total number of of photons in the spectrum [1]. The literature includes experimental measurements for three classes of prototype three-transition solar cells. In section 2.4.5.1, the present author reviews existing experimental results for prototypes where the intermediate levels are introduced by localized states [107, 54, 109, 55]. In section 2.4.5.2, the present author reviews existing experimental results for prototypes where the intermediate levels are introduced by quantum wells [58, 91, 92, 93]. In section 2.4.5.3, the present author reviews existing experimental results for prototypes where the intermediate levels are introduced by quantum dots [65, 67, 95, 41]. In section 2.4.5.4, the present author presents a comparative analysis with concluding remarks based on these experimental results. The present author now reviews experimental results of prototype three-transition absorbers.

2.4.5.1 Localized States

Summonte *et al.* conclude that solar cells implanted with a hydrogen layer may or may not yield an increase in generated current depending on the location of the hydrogen-implanted

[1] The theorized enhancement of the light-generated short-circuit current density is given, to first order, by equation (6) on page 22

layer [107]. They conclude that any increase in generated current results from sub-bandgap absorption resulting from the states of implanted hydrogen [107]. However, they conclude that there is a concomitant increase in recombination such that the hydrogen-implanted layer yields no increase in short-circuit current [107] with respect to reference solar cells. Bruns *et al.* conclude that solar cells implanted with a layer of helium atoms yield an increase in short-circuit current with respect to reference solar cells without such layers [54]. Similarly, Kasai and Matsumora conclude that silicon solar cells implanted with indium may or may not experience an enhancement in short-circuit current, as compared to silicon solar cells implanted with boron [109]. For two solar cells with identical carrier concentrations, the enhancement in photocurrent is observed only when the carrier concentration is roughly less than or equal to 3×10^{16} cm^{-3} and the photocurrent enhancement may be as large as 30% [109]. This conclusion is re-enforced in reference [55] where Kasai *et al.* illustrate a short-circuit enhancement of an indium-implanted solar cell as compared to a reference solar cell. In the next paragraph, the present author reviews results obtained from three-transition solar cells implemented with quantum wells.

2.4.5.2 Quantum Well

Barnham *et al.* are the first to illustrate the short-circuit current enhancement of *p-i-n* multiple quantum-well solar cells composed of GaAs quantum well enveloped in AlGaAs barriers, as compared to a reference without quantum wells [58]. Subsequently, Ragay *et al.* [91] and Ekins-Daukes *et al.* [92] illustrate the short-circuit current enhancement of *p-i-n* multiple quantum-well solar cells composed of InGaAs/GaAs as compared to a reference without quantum wells. Enhancements to the short-circuit current are also observed in strain-balanced GaAsP/InGaAs multiple quantum well solar cells as compared to reference GaAs solar cells [93]. In the next paragraph, the present author reviews results obtained from three-transition solar cells implemented with quantum dots.

2.4.5.3 Quantum Dot

Prototype three-transition solar cells implemented with quantum-dot technology almost exclusively yield diminished short-circuit current in comparison to their respective control

solar cells [65, 67, 95], except for one case [41] in which there is a measured increase of 0.8%. Norman *et al.* illustrate that prototype InGaAs/GaAs quantum-dot intermediate-band solar cells have significantly diminished short-circuit current, as compared to a control solar cell [65]. The same results are shown by Martí *et al.* [67] and López *et al.* [95] for prototype InAs/GaAs quantum-dot intermediate-band solar cells. Further, a general trend exists indicating that the more quantum-dot multi-layers incorporated into the solar cells, the more degradation is present in the short-circuit current density [65, 67, 95]. The present author now offers a comparative analysis of the generation of charge current with respect to the various proposed approaches to realize a three-transition solar cell.

2.4.5.4 Comparitive Analysis

In this section, Section 2.4.5.4, the present author presents a comparative analysis and offers concluding remarks based on the experimental data reviewed in section 2.4.5. The present author offers a broad assessment of this data followed by a specific assessment of the experimental data from prototype three-transition solar cells implemented with quantum dots. The latter is necessary because the present author's dissertation focuses on the quantum dot implementation.

One of the broad trends that the present author observes is that many prototype three-transition solar cells yield an enhanced short-circuit current, as compared to their respective controls [54, 109, 55, 58, 91, 93, 92, 41]. The global efficiency enhancement of a three-transition solar cell depends on the precept that a large portion of the photons in broadband illumination are converted so as to yield a large light generated charge current. The present author concludes that measured light-generated currents of prototype three-transition solar cells demonstrate this precept when referenced to their respective control solar cells. However, even in those prototypes with an enhancement in light-generated current as compared to their respective solar cells, the ratio of the light-generated current (normalized with respect to the elementary charge) to the number of photons in the broadband illumination is smaller than what is theoretically [20, 83] expected.

The present author observes that one of the trends particular to the quantum dot approach is that it generally yields a diminished short-circuit current, as compared to a control solar cell [65, 67, 95], with one exception [41]. The present author concludes that the synthesis of three-transition solar cells implemented with quantum-dot technology has significant room for improvement. Resulting from the formation of quantum-dot layers any number of processes are either increasing the average amount of reflection of incident photons before they are absorbed or, more likely, once photons are absorbed, photo-generated carriers are recombining via non-radiative processes before they are extracted from the contacts. Among a plethora of possible improvements to the design of quantum-dot three-transition solar cells, it plausible that the use of strain-compensating techniques and/or the use of surfactants may improve the short-circuit degradation of quantum-dot three-transition solar cell prototypes. The present author now reviews the voltage factors of prototype three-transition solar cells.

The present author concludes that experimental results relating to the generation of a large charge current does not definitively justify the assertion that the devices are three-transition solar cells. This conclusion is based on the fact that, where an enhancement exists with respect to a control, the enchantment is not sufficiently large to assert that photons across the broadband illumination source are causing this. An enhancement may also be caused, for example, by thermal up-conversion [110].

2.4.6 Demonstration of Voltage Factor

One of the central precepts of the three-transition solar cell is that it will have a large voltage factor [20]. This precept may be demonstrated by measuring the open-circuit voltage of prototype solar cells when illuminated by a simulated solar spectrum. The literature includes experimental measurements for three classes of prototype three-transition solar cells: those implemented with localized states, quantum wells, and quantum dots. Based on the review of experimental data, the present author draws two conclusions.

The theorized global efficiency enhancement of a three-transition solar cell integrally depends on a large voltage factor [20]. Wolf asserts this based on the argument that an

optimized three-transition solar cell has a large conduction-to-valence bandgap and that, based on empirical data, a single-junction, single-transition solar cell with large bandgap is likely to have a large voltage factor [20]. Ekins-Daukes illustrates that the maximum-power voltage of an idealized three-transition solar cell is greater than the second largest of the three-transition absorber's three bangaps - though not much larger [83]. Having summarized the theoretical predictions of the voltage factor of the three-transition solar cell, the present author now summarizes the experimental data.

The present author observes two trends based on a summary of experimental data from prototype three-transition solar cells. First, the recorded values of the open-circuit voltages and maximum-power voltages of all prototype three-transition solar cells are reduced compared to those of their respective controls. This is true of the helium-implanted solar cells of Bruns *et al.* [54], the indium-implanted solar cells of Kasai *et al.* [55], the GaAs/AlGaAs quantum-well solar cells of Barnham *et al.* [58, 111], the InGaAs/GaAs quantum-well solar cells of Ragay *et al.* [91], the GaAs/GaInP quantum-well solar cells of Barnham *et al.* [111], the InGaAs/InP quantum-well solar cells of Barnham *et al.* [111], the InAs/GaAs quantum-dot solar cells of Luque *et al.* [41, 63, 95], and the InGaAs/GaAs quantum-dot solar cells of Norman *et al.* [65]. Second, the larger the number of quantum-dot multilayers present in prototype quantum-dot three-transition solar cells, the larger the reduction in the voltage factor [65, 67, 95]. The present author offers conclusions based on these observations.

The present author draws two conclusions. First, it is unclear if the voltage factors required for a global efficiency enhancement are obtained in prototype three-transition solar cells. This lack of clarity results from imprecise evaluations of the absorbers' respective band structures. Second, the quantum-dot approach to realize a three-transition solar cell is faced with a fundamental paradox. This paradox is that a large number of multi-layers is essential for a high absorptivity of sub-bandgap photons [112], but observations indicate that as the number of multilayers increases, the voltage factor decreases. The present author now reviews experimental data relating to the presence of more than one quasi-Fermi level separation in prototype three-transition solar cells.

2.4.7 Separation of Quasi-Fermi Levels

One of the central precepts of the three-transition solar cell is that, under non-equilibrium conditions, the occupancy of electronic states comprising each of the three bands may be described by three distinct quasi-Fermi levels. The literature includes experimental measurements of more than one quasi-Fermi level separation for two classes of prototype three-transition solar cells. In section 2.4.7.1, the present author reviews the theoretical basis for the assertion that an absorber may maintain more than one quasi-Fermi level separation. In section 2.4.7.2, the present author reviews existing experimental results for prototypes where the intermediate levels are introduced by quantum wells [99, 100, 101, 102, 103]. In section 2.4.4.3, the present author reviews existing experimental results for prototypes where the intermediate levels are introduced by quantum dots [41, 62]. In section 2.4.7.4, the present author presents a comparative analysis with concluding remarks based on these experimental results. The expected results of these measurements are now discussed by the present author.

The present author now reviews experimental evidence focused on demonstrating the existence of more than two quasi-Fermi levels in prototype three-transition solar cells. This is discussed first for prototypes where the intermediate levels are introduced by quantum wells, and next for prototypes where the intermediate levels are introduced by quantum dots.

2.4.7.1 Theoretical Basis

In the majority of textbooks on semiconductors and semiconductor devices, it is explained that the non-equilibrium occupancy of electronic states in a semiconductor may be described by two distinct quasi-Fermi levels: one describing the occupancy of electrons in the conduction band, and another describing the occupancy of electrons in the valence band. This is so whether the semiconductor is intrinsic, p-type or n-type. Yet, in their discussion of the statistics of recombination of holes and electrons in semiconductors, Shockley and Read [43] explain that occupancy of trap levels within the semiconductor's bandgap is described by a third quasi-Fermi level: one that is uniquely associated with those traps [43]. To the best of

the present author's knowledge, it is Kettemann and Guillemoles [113] who first explicitly state the importance of more than two-quasi Fermi levels with respect to the capability of a multi-transition solar cell to overcome the upper-efficiency limit of the Shockley-Queisser solar cell [5]. In their discussion of multiple-transition solar cells implemented with low-dimensional structures (*e.g.* quantum wells), Kettemann and Guillemoles consider multiple electronic bands where each electronic band is comprised of delocalized quantum states and where the distribution of carriers in each electronic band is described by a unique quasi-Fermi level [113]. In the particular case of a three-transition solar cell, the upper-theoretical efficiency limit is fundamentally premised on three quasi-Fermi levels [113, 35, 56]. Experimentally verifying the existence of more than two quasi-Fermi levels is fundamentally important in demonstrating the feasibility of developing the three-transition solar cell. The present author now reviews experimental evidence focused on demonstrating the existence of more than two quasi-Fermi levels in prototype three-transition solar cells implemented with quantum wells.

2.4.7.2 Quantum Well

Tsui *et al.* assert that the absolute value of the quasi-Fermi-levels separation may be obtained from calibrated photoluminescence spectra or calibrated electroluminescence spectra [99]. They further apply this method to determine the quasi-Fermi-levels separation in single-quantum-well structures by using photoluminescence spectra in particular [99]. Using the method explained by Tsui *et al.* [99], Nelson *et al.* state that if one assumes that the quasi-Fermi-level separation in the quantum well is that of the voltage across the structure the the emission resulting from single-quantum-well structure is overestimated [100]. Rather, the calibrated emission spectrum implies that the quasi-Fermi-level separation in the quantum well is less than that of the voltage across the cell [100]. In fact, experimental investigations from InGaAs/GaAs and GaAs/AlGaAs quantum well structures yield evidence that the difference between the voltage and quasi-Fermi-level separation in the quantum well is a few tens of meV less than the applied voltage [100, 101]. From calibrated luminescent spectra, Kluftinger *et al.* infer that quasi-Fermi-level variations exist in

asymmetric double-quantum-well structures [102, 103]. In the next paragraph, the present author reviews results obtained from prototype three-transition solar cells implemented with quantum dots.

2.4.7.3 Quantum Dot

Luque and Martí assert the presence of three distinct quasi-Fermi levels in prototype three-transition solar cells implemented with quantum dot technology [41, 62]. They infer this based on two distinct analyses. In the first analysis, they infer the presence of three distinct quasi-Fermi levels based on the fit of experimental data to generalized circuit diagram of the three-transition solar cell [41]. Depending on both the operating point of the prototype three-transition solar cell and one of four fitting cases, Luque and Martí infer that the voltage between the conduction band and intermediate band in prototype three-transition solar cells implemented InAs/GaAs quantum dot structures may be anywhere between zero and 200 meV [41], and that the voltage between the conduction band and intermediate band may be anywhere between 70 meV and 1.2 eV). In the second analysis, they present evidence for the presence of three distinct quasi-Fermi levels in prototype three-transition solar cells by placing values of measured experimental data into closed-form expressions for the quasi-Fermi level separation [62]. In particular, from quantum efficiency measurements and electroluminescence spectra recorded from prototype three-transition solar cells implemented InAs/GaAs quantum dot structures, Luque and Martí infer that the voltage between the conduction band and intermediate band is between 190 meV and 280 meV [62].

2.4.7.4 Comparitive Analysis

In this section, Section 2.4.7.4, the present author presents a comparative analysis and offers concluding remarks based on the experimental data reviewed in section 2.4.7. The present author observes that several authors assert the existence of more than one quasi-Fermi-level separation in three-transition solar cells implemented with nanostructures [99, 100, 101, 102, 103, 41, 62]. The global efficiency enhancement of a three-transition solar cell depends on the precept that when the absorber is not in equilibrium, the distribution of carriers in the solar cell are described by three distinct quasi-Fermi levels, and hence three distinct

quasi-Fermi-level separations. The present author concludes that three-transition solar cells implemented with quantum wells may have a fundamental characteristic preventing them from realizing a global efficiency enhancement. This characteristic is that only two (rather than three) quasi-Fermi-level separations are observed: one in the quantum confined region and one in the barrier region [100, 101, 102, 103]. The present author now reviews the emission of photons from prototype three-transition solar cells.

2.4.8 Conclusions

In this section, Section 2.4, the present author reviews experimental results aimed at confirming several of the central precepts (see section 2.4.1 on page 34) on which rests the global efficiency enhancement of the three-transition solar cell. Based on a review of those results, the present author asserts that the absorption and emission of photons from three distinct transitions is not verified; that the collection of electron-hole pairs generated from three distinct absorption events is not verified; that, though an increase in charge current with respect to a control is observed, the magnitude of the charge current is not commensurate with the conversion of a significant faction of broadband illumination; that the maintenance of a large voltage factor is not verified; and that, though experimental evidence is purported, the existence of three distinct quasi-Fermi levels is not irrefutably verified. The present author concludes, that at the time that this disseration is published, a body of experimental evidence to support the existence of either a three-transition absorber or a three-transition solar cell is absent from the literature. The present author further concludes that experimental results relating to both the absorption and emission of photons is severely hampered by the lack of photo-detection in the infrared regime of the electromagnetic spectrum.

2.5 Conclusions

In this chapter, the present author reviews the theoretical operation of an idealized three-transition solar cell, reviews proposals to realize a three-transition solar cell, and reviews the experimental characterization of prototype three-transition solar cells.

Based on a summary of the theoretical operation of idealized three-transition solar cells, the present author concludes that there are two principle merits that justify research and

development of the three-transition solar cell. First, the three-transition solar cell is a single p-n junction device that is capable of achieving solar energy conversion efficiencies equivalent to that of a stack of three single-junction, single-transition solar cells. Second, the spectral robustness of the three-transition solar cell is greater than that of a tandem-stack of three single-junction, single-transition solar cells electrically assembled in series. Therefore, in practice, a three-transition solar cell with a band structure that deviates from the optimum band structure will have less deterioration than a tandem-stack of three single-junction, single-transition solar cells electrically assembled in series with a comparable deviation in its band structures as compared to the optimal band structures.

Based on a summary of the four proposals to realize a three-transition solar cell, the present author concludes that a global efficiency enhancement is not experimentally demonstrated in prototype three-transition solar cells. With respect to the above conclusion, it is imperative to experimentally verify each of the six fundamental precepts and four ancillary conditions (see section 2.4.1 for more details) on which the global efficiency enhancement is theoretically based. Until a global efficiency enhancement is experimentally demonstrated, this should be done for any and all prototype three-transition solar cells.

Based on a summary of the experimental characterization of prototype three-transition solar cells, the present author draws two conclusions. First, the present author concludes that at present, a body of experimental evidence to irrefutable support the existence of either a three-transition absorber or a three-transition solar cell is, in fact, absent from the literature. Second, the present author concludes that the absence of infrared detection while recording absorption and emission spectra severely hampers the ability to directly observe the existence of a three-transition absorber and three-transition solar cell. Without the present of infrared detection, researchers may, at best, infer the presence of three absorption edges or the presence of emission within three distinct spectral bands.

CHAPTER III

DETAILED-BALANCE EFFICIENCY OF THE INTERMEDIATE BAND SOLAR CELL UNDER NON-OPTIMAL CONDITIONS

3.1 Introduction

This chapter examines the detailed-balance conversion efficiency of a solar cell with an intermediate band (IB) under non-optimal conditions. In Section 3.2 the author presents a thermodynamic treatment of an intermediate band solar cell. The novelty is the inclusion of photo-induced electronic transitions between two distinct states of the intermediate band. The treatment allows for two blackbody sources, intraband and interband photo-induced electronic transitions, overlapping absorption coefficients, multiple electronhole pair generation, and non-radiative processes. A schematic of the device's thermodynamic configuration shows that the solar cell operates as a tandem stack of three p-n junctions. In Section 3.3 the author considers solar cells with ideal electro-chemical conversion, whose absorbers are intermediate bands media with finite bandwidths, which permit both interband and intraband photo-induced electronic transitions at states within the IB. To comprehend the effect of the IB width, three classes of IB absorbers are constructed, each of which is distinguished by its spectral selectivity. It is shown that (*i*) the maximum power efficiency tends gradually towards zero with increasing bandwidth when photo-induced interband transitions and intraband transitions exist at parity; (*ii*) with respect to the former, a relative efficiency enhancement may occur when photo-induced intraband transitions dominate interband transitions; and (*iii*) though thermodynamically consistent, efficiencies may be physically inconsistent without including photo-induced intraband transitions. The emphasis on both finite bandwidth and spectral selectivity enhances the scientific understanding of opto-electronic devices with intermediate states.

3.2 Intraband Absorption in Solar Cells with an Intermediate Band

3.2.1 Introduction

The novelty within Section 3.2 is the inclusion of photo-induced electronic transitions between two distinct quantum states of an electronic band that is intermediate between the conduction band (CB) and valence band (VB) (see Figure 12). This innovation is significant for two reasons. Foremost, when intraband transitions are absent, which is the case in reference [35], the detailed-balance analysis of an intermediate band (IB) solar cell (IBSC) yields results inconsistent with physical reality [13]. Additionally, in the case where the IB width exceeds the smallest bandgap in the system, which is the case for many candidate IB absorbers (see reference [46] and citations by those authors), the calculation of efficiency without these transitions fails to account for degradation resulting from parallel absorption paths [98]. The formalism here accounts for that portion of incoming photons that excite intraband electronic transitions that generate no photovoltaic power density. The approach here emphasizes the emission spectrum of the IB material. Thus, Section 3.2 may apply to photovoltaic devices, such as up- [114] and down-converters [115] and multi-band solar cell [36], as well as electron devices that operate in different regimes of the current-voltage characteristic [4]. These may include unstacked multi-color light emitting diodes [116] and unstacked multi-color photo-detectors [117].

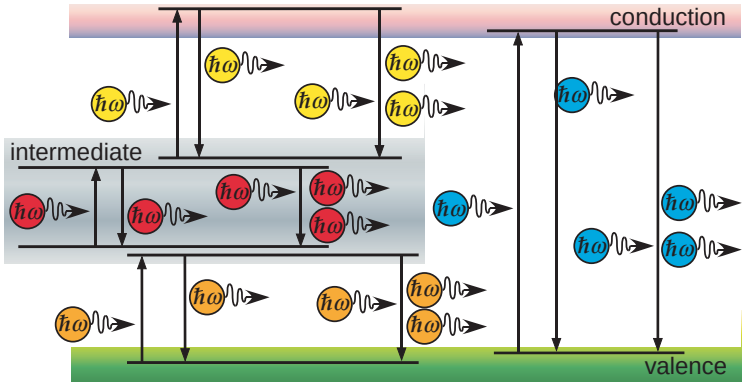

Figure 12: Interaction of light with the states of an intermediate band absorber. For each of the four electronic transitions (*i.e.* (I,I), (I,V), (C,I), and (C,V)), there are three types of photon interactions: (from left to right) stimulated absorption, stimulated emission, and spontaneous emission.

As shown in Figure 12, an IB absorber permits four photo-induced electronic transitions: an intra-band transition between two distinct states in the IB, (I,I); and three interband transitions between a state in the CB and VB, (C,V), between a state in the CB and IB, (C,I), and between a state in the IB and VB, (I,V), respectively. The set of allowed photo-induced electronic transitions, $\mathcal{T}$, is thus defined as $\mathcal{T} \doteq \{(\mathrm{I,I}), (\mathrm{I,V}), (\mathrm{C,I}), (\mathrm{C,V})\}$[1]. Shockley and Read [43] explain that the statistics of the absorber's conduction, intermediate, and valence states are each described by a unique quasi-Fermi level, $\varepsilon_{\mathrm{FC}}$, $\varepsilon_{\mathrm{FI}}$, and $\varepsilon_{\mathrm{FV}}$, respectively. The ideal structure [2] of an IBSC (see Figure 13) contains an IB absorber that is sandwiched between a *n*- and a *p*-type semiconductor [10]. The quasi-Fermi level separation, $\varepsilon_{\mathrm{FC}} - \varepsilon_{\mathrm{FV}}$, may bias a load voltage, V. The device may then pass a current density, J, and deliver a power density, $\dot{W} = V \times J$. Wolf explains that the performance of a solar cell permitting multiple photo-induced electronic transitions may surpass that of a single *p*-*n* junction solar cell with a single interband transition [20]. By using the statistics of photons in equilibrium with the allowed photo-induced electronic transitions [24], Luque and Martí write the photon fluxes absorbed and emitted by the solar cell [35], yet only for a narrow case, which does not include intraband transitions at intermediate levels.

In Section 3.2.2, the present author treats intraband transitions as well as a host of phenomena relevant to the practical operation of these solar cells. These are: interband electronic transitions at intermediate states [35], non-maximal geometric solar concentration [4], overlapping absorption coefficients [84], multiple electron-hole pair generation [118], and averaged non-radiative recombination [43]. In Section 3.2.3, conclusions are drawn from the results of detailed-balance calculations.

3.2.2 Thermodynamic Configuration

In this section, the performance measure of the device is defined in terms of the external extrinsic thermodynamic variables. Next, the photon emission spectrum of the absorbing medium is given implicitly as a function of the solar cell's internal intrinsic variables. This

[1]The set $\mathcal{T}$ may more generally include elements (C,C) and (V,V), which represent intraband electronic transitions between distinct states of the conduction and valence bands, respectively. If the quasi-Fermi level describing the electronic occupancy in one of these bands approaches or even surpasses the respective band edge, then it is important to include that element in $\mathcal{T}$. The approach here accommodates their inclusion.

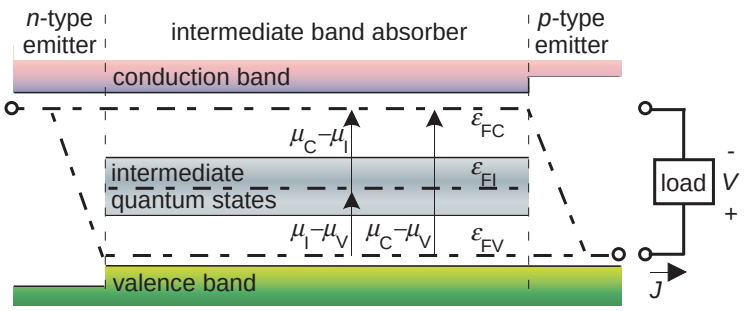

Figure 13: Ideal device structure of a solar cell whose quantum states form an intermediate band of finite width. Shown are the quasi-Fermi levels, $\varepsilon_{\mathrm{FX}}$, chemical potential differences, $\mu_{\mathrm{X}} - \mu_{\mathrm{Y}}$, voltage, V, and current density, J.

is required to finally establish the internal thermodynamic configuration of the solar cell and to specify the power density generated.

The author considers an engine driven by particle conversion: photons to electron-hole pairs. The first-law efficiency, η, is written as the photovoltaic power density generated by the converter, $\dot{W}$, over the energy flux impinging on the converter, $\dot{U}_{\mathrm{p}}$ (see Figure 14) [3]. Thus

$$\eta = \frac{\dot{W}}{\dot{U}_{\mathrm{p}}}. \tag{12}$$

Two radiation flows pump the converter. The first is a direct source of radiation from the Sun, which is assumed a black body with a surface temperature T_{S}, yielding a photon flux, $\dot{N}_{\mathrm{p,S}}$, and energy flux, $\dot{U}_{\mathrm{p,S}}$. The second is a diffuse source of radiation scattered from the Earth's atmosphere, which is assumed a black body with a surface temperature T_{E}, yielding a photon flux, $\dot{N}_{\mathrm{p,E}}$, and energy flux, $\dot{U}_{\mathrm{p,E}}$. Considering the dilution factor of solar radiation, $D\left[2.16 \times 10^{-5}\right]$, and a geometric solar concentration factor, C, which may range between unity and $1/D$ [4], the total energy flux impinging upon the converter, $\dot{U}_{\mathrm{p}}$, is written with the Stefan-Boltzmann constant, $\sigma\left[5.67 \times 10^{-8}\ \mathrm{W/m^2/K^4}\right]$, as

$$\dot{U}_{\mathrm{p}} = \sigma\left[C\,D\,T_{\mathrm{S}}^4 + (1 - C\,D)\,T_{\mathrm{E}}^4\right]. \tag{13}$$

The converter sinks a radiative energy and particle flux, $\dot{U}_{\mathrm{s}}$ and $\dot{N}_{\mathrm{s}}$, respectively, and a heat flow, $\dot{Q}$, which tends to elevate the converter's temperature, T_{L}, above that of the ambient. The performance measure, as defined in Eq. (12), diverges from previous detailed-balance

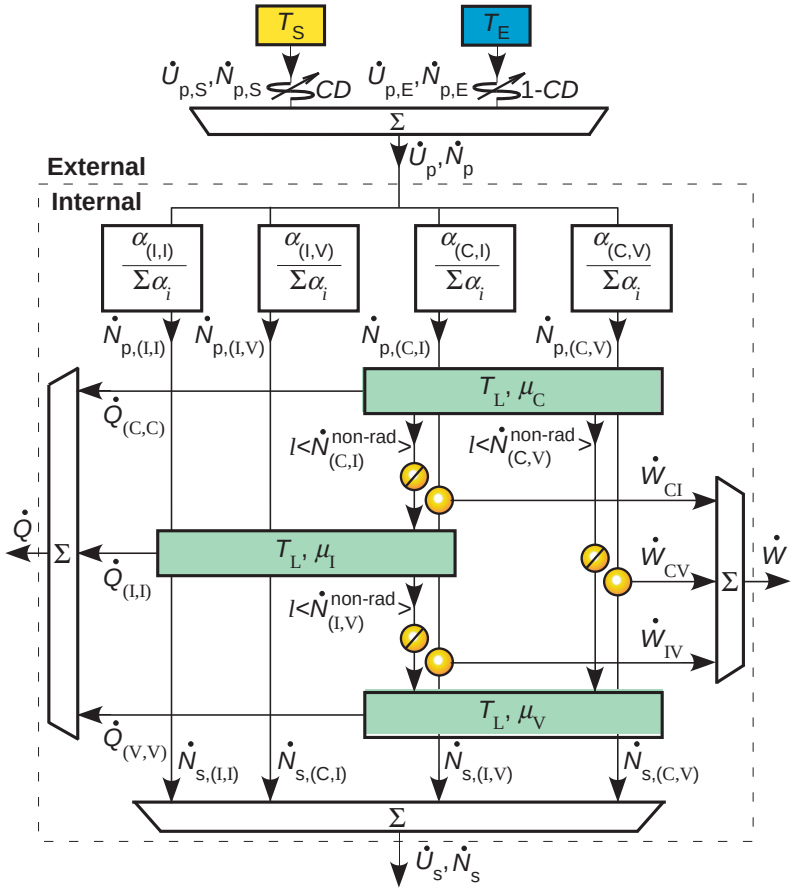

Figure 14: Thermodynamic configuration of a solar cell with an intermediate band of quantum states. The engines (circles) generate electric power by the net absorption of photons resultant from radiatively coupled interband electronic processes. Non-radiative interband recombination (circles with bars) ultimately only increase the rate of heat flow. Shown are the heat flows, $\dot{Q}_{(\mathrm{V,V})}$, $\dot{Q}_{(\mathrm{I,I})}$, and $\dot{Q}_{(\mathrm{C,C})}$, resultant from the irreversible equilibration of thermalized carriers via non-radiative intraband processes in the valence, intermediate, and conduction band, respectively.

work [13, 4, 10]. In these, though the particle flux, $\dot{N}_{\mathrm{p}}$, impinging upon the solar cell is given in terms of the dual source, the performance measure only considers the energy flux from the Sun, $\dot{U}_{\mathrm{p,S}}$. This distorts the performance measure of the device, resulting in efficiencies $\left[1+\frac{1-CD}{CD}\left(\frac{T_{\mathrm{E}}}{T_{\mathrm{S}}}\right)^4\right]$ times those obtained using the first-law efficiency given here.

An equilibrium analysis [24] reveals [13] that the equilibrium emission spectrum of an IB absorbing medium, $\dot{n}_\gamma$, is the direct sum of four (more generally the number of elements

in $\mathcal{T}$) summands, $\dot{n}_{\gamma,(\mathrm{X,Y})}$. These are

$$\dot{n}_{\gamma,(\mathrm{X,Y})}(\hbar\,\omega) = \frac{\alpha_{(\mathrm{X,Y})}(\hbar\,\omega)}{\sum\limits_{i\in\mathcal{T}} \alpha_i(\hbar\omega)}\, a(\hbar\,\omega)\, h_\gamma(\hbar\,\omega) f_{\gamma,(\mathrm{X,Y})}(\hbar\,\omega), \tag{14}$$

where i is an index into the set $\mathcal{T}$, $\hbar$ [1.05×10^{-34} J$\cdot$s] is Planck's constant, ω is the radian frequency of the photons, $\alpha_{(\mathrm{X,Y})}$ are the absorption coefficients [35, 13], a is the absorptivity of the absorber [13], h_γ is the number of photons per energy per second per area hitting the boundary surface of the absorbing medium [4], and $f_{\gamma,(\mathrm{X,Y})}$ are the Bose-Einstein distributions that describe the photons' statistics [35], which may include for multiple electron-hole pair generation [118].

The power density delivered to a matched load by the solar cell is the product of the external voltage across the device and the charge current density generated by particle conversion as

$$\begin{aligned}\dot{W} = \frac{\mu_\mathrm{C} - \mu_\mathrm{V}}{q} \times q\Bigg(&\dot{N}_{\mathrm{p},(\mathrm{C,V})} - \dot{N}_{\mathrm{s},(\mathrm{C,V})} - l\left\langle \dot{N}^{\text{non-rad}}_{(\mathrm{C,V})} \right\rangle \\ &+ \dot{N}_{\mathrm{p},(\mathrm{I,V})} - \dot{N}_{\mathrm{s},(\mathrm{I,V})} - l\left\langle \dot{N}^{\text{non-rad}}_{(\mathrm{I,V})} \right\rangle\Bigg).\end{aligned} \tag{15}$$

This is obtained by generalizing the ideal photo-chemical and electro-chemical conversions [35, 2] to include an averaged [43] rate of net non-radiative recombination per volume between the states of the X and Y bands, $\left\langle \dot{N}^{\text{non-rad}}_{(\mathrm{X,Y})} \right\rangle$. The power density is given in terms of the elementary charge, q [1.60×10^{-19} C], thickness of the solar cell, l, and the components of the photon flux emitted and absorbed by the device resultant from photon interactions with allowed (X,Y) electronic transitions, $\dot{N}_{\mathrm{s},(\mathrm{X,Y})}$ and $\dot{N}_{\mathrm{p},(\mathrm{X,Y})}$, respectively. These are given as

$$\dot{N}_{\mathrm{s},(\mathrm{X,Y})} = \int_0^\infty \dot{n}_{\gamma,(\mathrm{X,Y})}\, d\hbar\omega \text{ and} \tag{16}$$

$$\dot{N}_{\mathrm{p},(\mathrm{X,Y})} = \int_0^\infty a \frac{\alpha_{(\mathrm{X,Y})}}{\sum\limits_{i\in\mathcal{T}} \alpha_i} \left[C\,D\,\dot{n}_{\gamma,\mathrm{S}} + (1 - C\,D)\;\dot{n}_{\gamma,\mathrm{E}}\right]\, d\hbar\omega, \tag{17}$$

where $\dot{n}_{\gamma,\mathrm{S}}$ and $\dot{n}_{\gamma,\mathrm{E}}$ are the emission spectra of the Sun and Earth, respectively [4]. Eq. (15) takes into account that the IBSC is internally biased so that [35] the net rate of charge

injected and extracted from the IB is in balance as

$$q\left[\dot{N}_{\mathrm{p,IV}}-\dot{N}_{\mathrm{s,IV}}-l\left\langle\dot{N}_{\mathrm{(I,V)}}^{\text{non-rad}}\right\rangle\right]= q\left[\dot{N}_{\mathrm{p,CI}}-\dot{N}_{\mathrm{s,CI}}-l\left\langle\dot{N}_{\mathrm{(C,I)}}^{\text{non-rad}}\right\rangle\right], \tag{18}$$

and also that [35] the potential differences sum as follows with respect to the external voltage, V, across the solar cell (see Figure 13)

$$V=\left(\mu_{\mathrm{C}}-\mu_{\mathrm{V}}\right)/q=\left(\mu_{\mathrm{C}}-\mu_{\mathrm{I}}\right)/q+\left(\mu_{\mathrm{I}}-\mu_{\mathrm{V}}\right)/q. \tag{19}$$

Figure 14 presents the internal thermodynamic configuration of a photovoltaic solar cell with an intermediate band of quantum states. It shows that a solar cell with an intermediate band of quantum states operates as three particle engines working together. Each of the internal reservoirs is ascribed a unique chemical potential, μ_{X} [4], which is related to the electrochemical potential, $\varepsilon_{\mathrm{FX}}$ [24].

3.2.3 Results and Conclusions

Figure 15 gives the optimized conversion efficiencies at maximum power, $\eta|_{\mathrm{MP}}$, of IBSC as a function of IB width. In computing these results, it is assumed that when there is the physical possibility of both photo-induced intra- and interband electronic transitions at intermediate levels that the latter predominate. It is shown that (1) detailed-balance approaches that ignore the energy flow incident on the converter from the earth, $\dot{U}_{\mathrm{p,E}}$, result in efficiencies greater than those obtained from the first-law efficiency by a factor $\left[1+\frac{1-C\,D}{C\,D}\left(T_{\mathrm{E}}/T_{\mathrm{S}}\right)^{4}\right]$ and (2) as the IB width increases, the efficiencies saturate to those of two-stack tandem solar cells [13].

From these results, the author draws three conclusions. (*i*) The performance of an IBSC is limited by that of a tandem stack of three electrically-unconstrained single-junction solar cells. (*ii*) The assumption that interband transitions predominate over intra-band transitions, which is equivalent to ignoring or excluding intraband transitions, yields results inconsistent with physical reality. When the IB widths approach infinity, the band structures approach that of a black body. Please note, however, that the efficiencies do not approach those of a black body – though a black body may generate a heat flow, it generates no

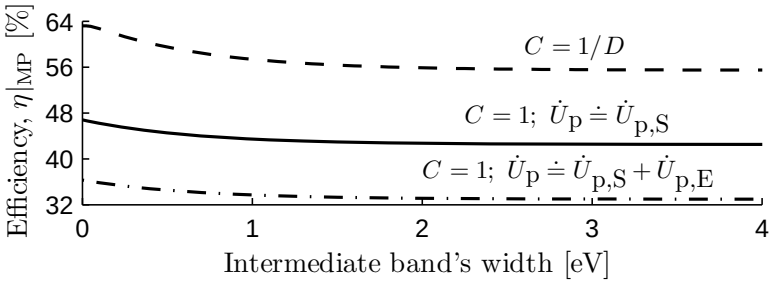

Figure 15: Optimized efficiencies of an intermediate band solar cell for two geometric concentrations, C, and with the assumption that interband transitions predominate over intraband transitions. Detailed-balance approaches that ignore the energy flow incident on the converter from the earth, $\dot{U}_{\mathrm{p,E}}$, yield efficiencies greater than or equal to those obtained by the first-law efficiency.

photovoltaic power. (*iii*) Detailed-balance methods that ignore the radiant energy transfer between the converter and the earth may yield efficiencies larger than those calculated with the first-law efficiency.

3.3 Solar Cell with an Intermediate Band of Finite Width

3.3.1 Introduction

The novelty within Section 3.3 is quantifying the impact of both finite intermediate band (IB) width and spectral selectivity on the optimized detailed-balance conversion efficiencies of the IB solar cell [35] (IBSC) and its associated band structure. The work is sigificant as it shows that (*i*) finite bandwidths result in a graceful degradation in the efficiency and (*ii*) the most suitable band structures for solar energy conversion differ significantly depending on the IB width and on the spectral selectivity of the absorbing medium. The inclusion of finite bandwidths is important whether the IB absorber is formed with dopants [45] or with alloys [48, 49, 51, 48, 49, 51]. Candidate alloys show IB widths of order 100 meV [48, 49, 51] or 1 eV [48, 49, 51]. In an earlier work [44], the author examinea IB width and showa that though thermodynamically consistent [119], the results of detailed-balance calculations are physically inconsistent when photo-induced, intraband transitions are excluded or ignored [44]. The author demonstrates here that the inclusion of intraband transitions yield fully consistent results.

Three classes of absorbers are postulated, each with a distinct spectral selectivity: (*i*) where intraband absorption coupled to two distinct states of the IB is at parity with interband absorption coupled to a state of the IB, (*ii*) where interband absorption dominates intraband absorption, and (*iii*) *vice versa*. Beyond its use in identifying materials for an IBSC, resulting from its emphasis on an absorber that permits both intra- and interband transitions at intermediate levels, Section 3.3 provides a more comprehensive understanding of a general class of opto-electronic devices with intermediate states: *i.e.*, up- [114] and down-converters [120], and multi-band solar cells [38].

The IBSC is a solar cell whose efficiency limit (63.2% [35]) surpasses the Shockley-Queisser efficiency limit (44% [5]). As shown in Figure 16, the absorber of this cell contains quantum states forming an IB of width, $\Delta\varepsilon_{\mathrm{IB}}$. Resulting from the states of the IB, there are three allowed photo-induced, interband electronic transtions [35]: between a state in the IB and one in the valence band, (I,V), between a state in the conduction band and one in the IB, (C,I), and between a state in the conduction band and one in the valence band, (C,V). In addition there are photo-induced, intraband electronic transistions between two distinct states in the IB, (I,I). Thus, the set of allowed photo-induced electronic transitions of an IBSC absorber, $\mathcal{T}$, is defined as $\mathcal{T} \doteq \{(\mathrm{I,I}), (\mathrm{I,V}), (\mathrm{C,I}), (\mathrm{C,V})\}$ [44]. Resulting from the three interband transition, the IBSC absorbing region is thermodynamically equivalent to three constrained particle engines operating in tandem [44], so that its efficiency limit has an upper ceiling at the limit of a tandem stack of three unconstrained single-junction, single-transition solar cells (63.8%) [8].

The efficiency of an IBSC is obtained by calculating six photon flows [35]: one photon flow absorbed by and one photon flow emitted from the converter resulting from each of the three interband electronic transitions. To describe each photon flow resulting from (X,Y) transitions, the absorption coefficients are relavent twice. First, the sum of all the absorption coefficients, $\sum_{i\in\mathcal{T}} \alpha_i(\hbar\omega)$, appears in the expression of the absortivity [13]. Second, the

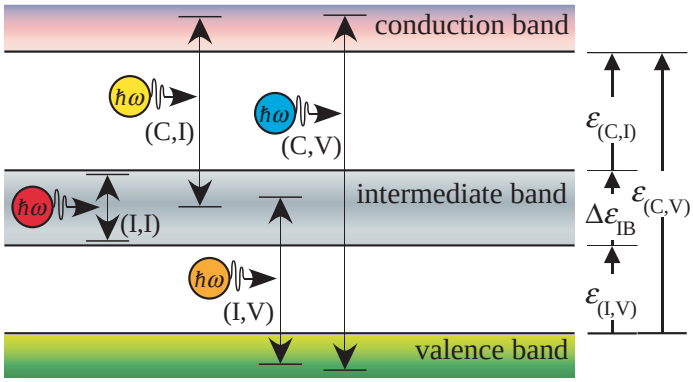

Figure 16: Reduced band structure of an intermediate band solar cell absorber. The bandgaps between bands X and Y, $\varepsilon_{(\mathrm{X,Y})}$, are shown as well as the intermediate band's width, $\Delta\varepsilon_{\mathrm{IB}}$. Also illustrated is the set, $\mathcal{T}$, of photo-induced electronic transtions: $\{(\mathrm{I,I}), (\mathrm{I,V}), (\mathrm{C,I}), (\mathrm{C,V})\}$.

aborption coefficient $\alpha_{(\mathrm{X,Y})}$ appears normalized in terms of the sum as [44]

$$\frac{\alpha_{(\mathrm{X,Y})}(\hbar\omega)}{\sum\limits_{i\in\mathcal{T}} \alpha_i(\hbar\omega)},$$

where i is an index into the set $\mathcal{T}$, $\hbar$ is Planck's constant, and ω is the radian frequency of the photons.

In the following sections, the author constructs the three distinct IB absorbers where each is distinguishing by its spectral selectivity and then gives and discusses their maximum-power solar energy conversion efficeincies.

3.3.2 Spectral Selectivity

Here, the author constructs three classes of IB absorbers, each class distinguished by its normalized absorption coefficients. To do this, attention is first directed two a band structure where the bandgaps $\varepsilon_{(\mathrm{X,Y})}$ spread within the domain of large solar irradiance. Next, the interplay between spectral selectivity and absorption overlap [84] is considered. Finally, the interplay between spectral selectivity and intraband transitions is considered.

When $\varepsilon_{(\mathrm{I,V})}$, $\varepsilon_{(\mathrm{C,I})}$, and $\varepsilon_{(\mathrm{C,V})}$ (see Figure 16) are spread within the domain of high solar irradiance, it is ideal if photons join two electronic states seperated by the largest bandgap less than the photons' energies. This is because photon interaction with matter is

associated with a rate of irreversible entropy generation, which itself increases monotonically with $\left(\hbar\omega - \mu_{(\mathrm{X,Y})}\right)$ [24], where $\mu_{(\mathrm{X,Y})}$ is the potential difference of the carriers in bands X and Y. The normalized absorption coefficients yield this spectral selectivity if, beginning at the onset of (C,I) transitions, the product of the matrix elements of momentum and joint density of states [121] governing (C,I) transitions is several orders of magnitude larger than the corresponding product governing (I,V) transitions. Similarly, beginning at the onset of (C,V) transitions, the (C,V) product must be orders greater that the corresponding (C,I) product.

With regard to absorption overlap the author considers a band structure where $\varepsilon_{(\mathrm{C,I})}$ is equal to $\varepsilon_{(\mathrm{I,V})}$. In this example, the ideal selective selectivity for photons in the range $(\varepsilon_{(\mathrm{I,V})} \leq \hbar\omega < \varepsilon_{(\mathrm{C,V})})$ is such that there are equal probabilities of photon absorption due to (I,V) transitions and (C,I) transitions. In this case, the overlap between the (I,V) and (C,I) absorption, $\varepsilon_{\mathrm{vp}} \doteq u\left(\alpha^{\mathrm{off}}_{(\mathrm{I,V})} - \alpha^{\mathrm{on}}_{(\mathrm{C,I})}, 0\right)$, is best if $\varepsilon_{\mathrm{vp}} = \varepsilon_{(\mathrm{C,V})} - \varepsilon_{(\mathrm{I,V})}$. $\varepsilon_{\mathrm{vp}}$ adjusts the I-V characteristics due to (I,V) and (C,I) excitations so at the cell's maximum power point (MPP), the constituent engines operate at their individual MPP.

With regard to the allowed intraband transitions, the author considers IB absorbers classified in one of three ways. For the situation where the IB width is larger than the smallest bandgap in the system, the absorbers may be distinguished by the absorption properties for photons within the range $\left(\Delta\varepsilon_{\mathrm{IB}} \leq \hbar\omega < \min\varepsilon_{(\mathrm{X,Y})}\right)$. The first class of absorber is distinguished by a parity of photo-induced, intraband electronic transitions and photo-induced, interband electronic transitions. For this class, for photons in the specified range, all of the non-zero absorption coefficients are of equal value. The second class of aborbers is distinguished so that photon exchange within this range is solely coupled to intraband transitions. Thus, in this range, the absorption coefficients $\alpha_{(\mathrm{I,V})}$, $\alpha_{(\mathrm{C,I})}$, and $\alpha_{(\mathrm{C,V})}$ are null. The third is distinguished so that photo-induced electronic transitions are solely coupled to interband transitions, so that the absorption coefficient $\alpha_{(\mathrm{I,I})}$ is null within this range.

The author, therefore, writes the ideal normalized absorption coefficients as

$$\frac{\alpha_{(\mathrm{X,Y})}(\hbar\omega)}{\sum\limits_{i\in\mathcal{T}}\alpha_i(\hbar\omega)} = \frac{u\Big(\hbar\omega,\, \alpha^{\mathrm{on}}_{(\mathrm{X,Y})}\Big) - u\Big(\alpha^{\mathrm{off}}_{(\mathrm{X,Y})},\, \hbar\omega\Big)}{\sum\limits_{i\in\mathcal{T}}\Big[u(\hbar\omega,\, \alpha^{\mathrm{on}}_{\mathrm{i}}) - u\big(\alpha^{\mathrm{off}}_{\mathrm{i}},\, \hbar\omega\big)\Big]}, \tag{20}$$

where the unit step functions, u, indicate the ideal absorption onsets and offsets for each of the three classes of IB aborbers. The onset and offset of photon exchange due to (X,Y) transitions begins with photons with energies greater than or equal to $\alpha^{\mathrm{on}}_{(\mathrm{X,Y})}$ and $\alpha^{\mathrm{off}}_{(\mathrm{X,Y})}$ respectively. Table 3 gives these values for each class of IB aborber, where it is uniformly assumed that $\varepsilon_{(\mathrm{C,I})} \geq \varepsilon_{(\mathrm{I,V})}$. In obtaining these results, a simplifying assumption is made: for any range of photon energies, all non-zero absorption coefficients within this range are of equal value. The normalized absorption coefficients thus take one of the following values: 0, 1/3, 1/2, or 1. The following section presents and explains the results of the detailed-balance analysis.

Table 3: This table gives the onsets, $\alpha^{\mathrm{on}}_{(\mathrm{X,Y})}$, and offsets, $\alpha^{\mathrm{off}}_{(\mathrm{X,Y})}$, of photon exchange due to (X,Y) transitions that lead to optimum maximum-power efficiencies. They are given for the three classes of intermediate band solar cell absorbers, such that when there is the possibility of both photo-induced interband and intraband electronic transitions, the transitions exist at parity, they are limited to interband electronic transitions, or they are limited to intraband electronic transitions.

	parity	lim. to interband	lim. to intraband
$\alpha^{\mathrm{on}}_{(\mathrm{I,I})}$	0	0	0
$\alpha^{\mathrm{off}}_{(\mathrm{I,I})}$	$\Delta\varepsilon_{\mathrm{IB}}$	$\min\left(\varepsilon_{(\mathrm{I,V})},\Delta\varepsilon_{\mathrm{IB}}\right)$	$\Delta\varepsilon_{\mathrm{IB}}$
$\alpha^{\mathrm{on}}_{(\mathrm{I,V})}$	$\varepsilon_{(\mathrm{I,V})}$	$\varepsilon_{(\mathrm{I,V})}$	$\max\left(\varepsilon_{(\mathrm{I,V})},\Delta\varepsilon_{\mathrm{IB}}\right)$
$\alpha^{\mathrm{off}}_{(\mathrm{I,V})}$	$\varepsilon_{(\mathrm{C,I})}+\varepsilon_{\mathrm{vp}}$	$\varepsilon_{(\mathrm{C,I})}+\varepsilon_{\mathrm{vp}}$	$\max\left(\varepsilon_{(\mathrm{C,I})}+\varepsilon_{\mathrm{vp}},\Delta\varepsilon_{\mathrm{IB}}\right)$
$\alpha^{\mathrm{on}}_{(\mathrm{C,I})}$	$\varepsilon_{(\mathrm{C,I})}$	$\varepsilon_{(\mathrm{C,I})}$	$\max\left(\varepsilon_{(\mathrm{C,I})},\Delta\varepsilon_{\mathrm{IB}}\right)$
$\alpha^{\mathrm{off}}_{(\mathrm{C,I})}$	$\varepsilon_{(\mathrm{C,V})}$	$\varepsilon_{(\mathrm{C,V})}$	$\max\left(\varepsilon_{(\mathrm{C,V})},\Delta\varepsilon_{\mathrm{IB}}\right)$
$\alpha^{\mathrm{on}}_{(\mathrm{C,V})}$	$\varepsilon_{(\mathrm{C,V})}$	$\varepsilon_{(\mathrm{C,V})}$	$\max\left(\varepsilon_{(\mathrm{C,V})},\Delta\varepsilon_{\mathrm{IB}}\right)$
$\alpha^{\mathrm{off}}_{(\mathrm{C,V})}$	$\lim\to\infty$	$\lim\to\infty$	$\lim\to\infty$

3.3.3 Results and Discussion

Figure 17 presents optimized detailed-balance conversion first-law efficiencies at maximum power, $\eta|_{\mathrm{MP}}$ [44], of the IBSC as a function of the IB width. In calculating the efficiencies, the formalism of reference [44] is used where: non-radiative recomibination is null; multiple electron-hole generation is non-existant; and, for photons in those ranges that join electronic transtions, the absorptivity is unity. All results are calculated for a surface solar temperature of 6000 K, a surface terrestrial temperature of 300 K, and a converter whose lattice is held at that of the surface terrestrial temperature. For each value of $\Delta\varepsilon_{\mathrm{IB}}$, the efficiency at maximum power is found with an optimization routine that treats $\varepsilon_{(\mathrm{I,V})}$, $\varepsilon_{(\mathrm{C,I})}$, and $\varepsilon_{\mathrm{vp}}$ as parameters in the search space. In precisely computing the photon flows, the method of reference [122] is used. Results are given for the three classes of IB aborbers and two values of geometric concentration: the maximum physically realizable concentration [5] ($\times$46,300) and non-concentrated ($\times$1) solar illumination.

With respect to the class of IB aborber such that photo-induced interband transitions and intraband transitions exist at parity whenever there is the physical possibility of both, Figure 17 shows that the optimum detailed-balance efficiency monotonicly decreases to zero as a function of the IB width. Although not visible, the data indicates that for the case of the maximum concentration there is a short lived increase in efficiency, so that the limiting IBSC efficiency (63.2 %) is achieved for a bandwidth of 15 meV. Brown *et al.* first note this perceptible increase [36]. As shown in Figure 18, the bandgaps generally increase with the bandwidth. For bandwidths greater than Wein's energy for a blackbody at 6000 K, $\varepsilon_{(\mathrm{I,V})}$ maintains the value of $\Delta\varepsilon_{\mathrm{IB}}$ so as to minimize losses due to non-work producing intraband transitions. Figure 19 shows that, in general, an absorption overlap, $\varepsilon_{\mathrm{vp}}$, of order meV is associated with the maximum power efficiencies throughout their trajectories.

With respect to the class of IB aborber such that photon exchange is limited to interband electronic transitions whenever there is the physical possibility of both inter- and intraband transitions, Figure 17 shows a monotonic decrease in the efficiency as a function of the IB width. As the width of the IB increases, the optimum efficiencies and their associated bandgaps, $\varepsilon_{(\mathrm{I,V})}$ and $\varepsilon_{(\mathrm{C,I})}$ (see Figure 18), saturate. On saturating, the efficiency and these

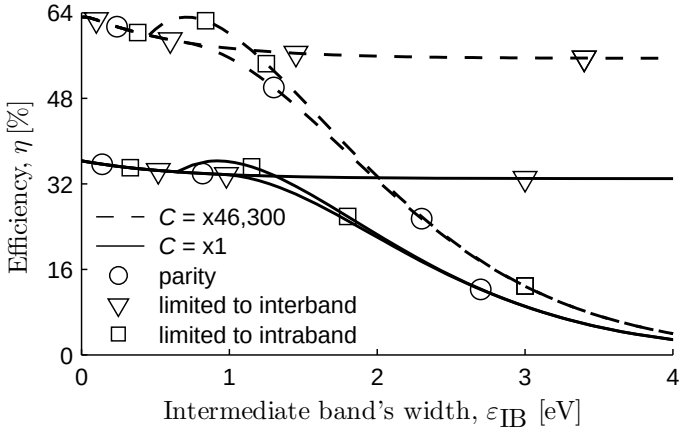

Figure 17: Maximum power efficiency of intermediate band solar cell as a function of the intermediate band's width. Curves are given for two geometrical concentrations factors and for three classes (see Tab. 3) of intermediate band aborbers. The concentrations are the maximum physically realizable concentration (×46,300) and non-concentrated (×1) solar illumination. Limiting efficiency of 63.2% occurs when $\Delta\varepsilon_{\mathrm{IB}}$ is 15 meV.

associated bandgaps are those of an optimized two-junction tandem electrically assembled in series [11]. This indicates that as the IB width increases, the power absorbed due to (C,V) electronic excitations steadily decreases. Ultimately, the photo-induced (C,V) excitations offer negligible contribution as there are relatively few photons in the solar spectrum with such high energies. That the IBSC operates as a two-junction solar cell results from the stringent condition that photo-induced electronic transitions are limited to interband transitions and the solar cells current and voltage constraints [35, 44].

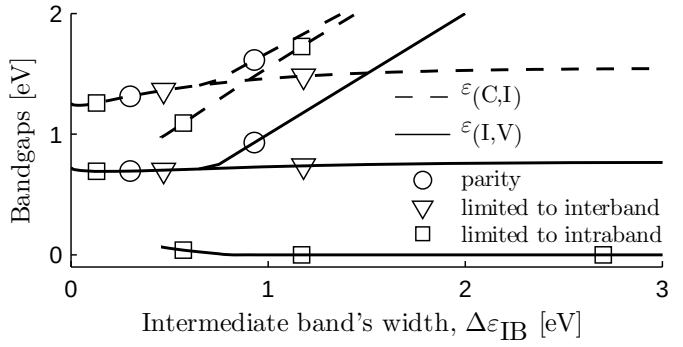

Figure 18: Bandgaps $\varepsilon_{(\mathrm{I,V})}$ and $\varepsilon_{(\mathrm{C,I})}$ associated with efficiencies given in Figure 17. Results given for a concentration of (×46,300).

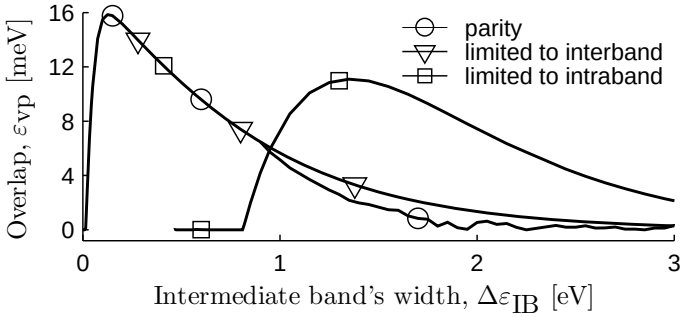

Figure 19: Overlap (see Tab. 3) between (I,V) and (C,I) absorption. Results associated with maximum power efficiencies of Figure 17 for a concentration of (×46,300).

Though the detailed-balance method is thermodynamically consistent, the results obtained for this class are not physically coherent for large bandwidths. As the bandwidth increases *ad absurdum*, the electronic band structure appears as that of a black body. Though a black body may produce a heat flux, no photovoltaic work may be produced from such aborbers, for all the carriers are in thermodynamic equilibrium. The more the bandwidth exceeds Wien's energy for a blackbody at 6000 K, the more physically inconsistent are the results.

With regards to the class of IB aborber with photon exchange limited to intraband electronic transitions whenever there is the physical possibility of both inter- and intraband transitions, Figure 17 shows that the trajectories of the efficiencies follow similar courses as those of class parity up until a bandwidth of 0.46 eV and 0.65 eV, respectively, for concentrations of (×46,300) and (×1). At these bandwidths this class offers a relative efficiency enhancement with respect to class parity.

A solar cell with this class of absorber exploits the fact that the absorption onset due to (I,V) transitions is limited by $\Delta\varepsilon_{\mathrm{IB}}$ rather than $\varepsilon_{(\mathrm{I,V})}$. The upshot is that the internally biased chemical potential difference, $\mu_{(\mathrm{I,V})}$, is no longer limited from above by $\varepsilon_{(\mathrm{I,V})}$, but rather by $\Delta\varepsilon_{\mathrm{IB}}$. Additionally, $\varepsilon_{(\mathrm{I,V})}$ is no longer relevant in calculating the net photon flux absorbed due to (I,V) transitions, so it may be decreased if it enhances the performance of the solar cell. Figure 18 shows that a performance gain is indeed obtained by a concomitant reduction of $\varepsilon_{(\mathrm{C,I})}$ and $\varepsilon_{(\mathrm{C,V})}$, so that the onsets of optical absorption are spaced more evenly

across the range of high solar irradiance; consequently, there is an increase in the net photon flux absorbed due to both (C,I) and (C,V) transitions. In theory, the value of $\varepsilon_{(\mathrm{I,V})}$ may not approach arbitrarily close to zero because at some threshold [123] the rate of non-radiative, interband transitions induced by phonon emission may no longer be ignored. In such case, the premises of the equilibrium analysis [24] are violated; for the carriers in the valence band and IB would be brought to thermodynamic equilibrium by the phonon exchanges.

3.3.4 Conclusions

Section 3.3 quantifies the effect of the intermediate band's width, $\Delta\varepsilon_{\mathrm{IB}}$, and spectral selectivity on idealized intermediate band solar cells. The author concludes that, irrespective of the geometric concentration factor, resulting from the solar surface temperature of ~6000 K, the largest efficiencies result when $\Delta\varepsilon_{\mathrm{IB}} \lessapprox \mathcal{O}\left(\hbar\omega_{\mathrm{W}}\big|_{6000\ \mathrm{K}} = 825\ \mathrm{meV}\right)$, where $\mathcal{O}$ is the order of Wein's energy, $\hbar\omega_{\mathrm{W}}$, of a black-body with a surface temperature $T_{\mathrm{P}} = 6000$ K. When $\Delta\varepsilon_{\mathrm{IB}} = 825$ meV, the first-law efficiencies may reach 57.9% and 33.9% (as compared with 63.2% and 36.3% when $\Delta\varepsilon_{\mathrm{IB}} = 0$) for fully concentrated and non-concentrated solar ilumination, respectively. When $\Delta\varepsilon_{\mathrm{IB}} \lessapprox \mathcal{O}\left(\hbar\omega_{\mathrm{W}}\right)$, to achieve high efficiencies at large concentrations, the smallest and next smallest bandgap ought be roughly 100 meV smaller and 500 meV larger than $\mathcal{O}\left(\hbar\omega_{\mathrm{W}}\right)$, respectively. Finally, when $\Delta\varepsilon_{\mathrm{IB}}$ is greater than the smallest bandgap, photo-induced, intraband transitions are necessary to present a physically consistent model of the solar cell's operation.

3.4 Conclusions

The author begins Chapter 3 by examining the detailed-balance conversion efficiency of a solar cell with an intermediate band (IB) under non-optimal conditions. This examination allows for two blackbody sources, intraband and interband photo-induced electronic transitions, overlapping absorption coefficients, multiple electron-hole-pair generation, and non-radiative processes. The author concludes that ignoring or excluding intraband transitions may yield results inconsistent with physical reality and that ignoring the radiant energy transfer between the converter and the earth may yield efficiencies greater than those calculated with the first-law efficiency. The author continues Chapter 3 by quantifying the

effect of the intermediate band's width and spectral selectivity on idealized intermediate band solar cells. Irrespective of the geometric concentration factor and resulting from the solar surface temperature, the author concludes that the largest efficiencies result when the intermediate band's width is roughly equal to or less than 825 meV: Wein's energy of a black-body with a surface temperature of 6000 K. The author further concludes that when the intermediate band's width is approximately less than or equal to 825 meV, in order to achieve high efficiencies at large concentrations, the smallest and next smallest bandgap ought to be roughly 100 meV smaller and 400-500 meV larger than 825 meV, respectively; and that when the intermediate band's width is greater than the smallest bandgap, photo-induced, intraband transitions need to be included for physical consistency. The results of this Chapter 3 are used in Chapter 4 to calculate the iso-efficiency contour plot of an intermediate band solar cell.

CHAPTER IV

NANOSTRUCTURED ABSORBERS FOR MULTIPLE TRANSITION SOLAR CELLS

4.1 Introduction

This chapter identifies absorbers for multiple transition solar cells that are implemented with nanostructured heterojunctions (*e.g.* quantum well solar cells with quasi-Fermi level variations and quantum dot intermediate band solar cells). In the radiative limit the solar cells implemented with these absorbers are capable of achieving a conversion efficiency $\geq$50% with a geometric solar concentration of at least $\times$1000. The technical approach enumerates a set of quantitative design rules and applies the rules to the technologically important III-V semiconductors and their ternary alloys. A novel design rule mandates a negligible valence band discontinuity between the barrier material and confined materials. Another key design rule stipulates that the substrate have a lattice constant in between that of the barrier material and that of the quantum confined material, which permits strain compensation. Strain compensation allows a large number of quantum dot layers to be incorporated into the solar cell because each layer is freer of defects. Four candidate materials systems (confined/barrier/substrate) are identified: $InP_{0.85}Sb_{0.15}$/GaAs/InP, $InAs_{0.40}P_{0.60}$/GaAs/InP, InAs/$GaAs_{0.88}Sb_{0.12}$/InP, and InP/$GaAs_{0.70}P_{0.30}$/GaAs. Resulting from the design features, the candidate systems may also find use in other opto-electronic applications.

The remainder of this chapter is organized as follows. Section 4.2 presents detailed background information. Section 4.3 enumerates and details the quantitative design rules, Section 4.4 explains how these rules are applied to the technologically III-V material systems. Section 4.5 follows with concluding remarks.

4.2 Background

Physical phenomena that may increase the efficiency of a single junction solar cell above the Shockley-Queisser limit [5] include proposals such as multiple transitions [20], multiple

electron-hole pair generation [30], and hot carriers [33]. Identifying materials that may be used to implement these phenomena is of significant interest. For example, multiple electron-hole pair generation is demonstrated in several materials [124, 125]. Several approaches are proposed to implement multiple transition solar cells, all of which require the introduction of valid quantum states deep into the previously forbidden bandgap of a host semiconductor [20]. Two of these, which rely on nanostructured heterojunctions, are the quantum well solar cell with quasi-Fermi level variations [56] and the quantum dot (QD) intermediate band solar cell (IBSC) [59]. It is important to note that both of these approaches may be shown to be thermodynamically consistent [119]. Until now, material systems that are most suitable to implement these two solar cells are not yet identified.

This chapter identifies absorbers for solar cells that utilize nanostructured heterojunctions to generate multiple transitions [56, 59], and that are theorized [56, 59] and experimentally inferred [100, 62] to maintain more than one quasi-Fermi level separation. Specifically, the material systems identified here may lead to devices capable, in principle, of conversion efficiencies $\geq$50% with a geometric solar concentration of at least $\times$1000. The technical approach taken here identifies candidate material systems by enumerating quantitative design rules and by applying these design rules to the technologically important III-V semiconductors and their ternary alloys. Though the remainder of this chapter gives pronounced emphasis to the QD IBSC, the chapter may find use in developing related photovoltaic technologies and in other opto-electronic communities.

In the QD IBSC [59, 60, 61], the intermediate states within the formerly forbidden bandgap are introduced by the three-dimensional confining potential created by the QD heterojunctions. The states introduced by the QD heterojunctions may either form a band of extended states, which would yield beneficial transport properties, or a collection of localized states as shown in Figure 20. The material systems identified here would be appropriate regardless of whether a band of extended states is formed or not. With respect to the former case, a band of extended states with well-defined band edges and band width requires some measure of order [45] (for a general discussion, see reference [126] and references therein). Allowing that the required order exists, then one may consider a QD crystal

with miniband formation resultant from coupling between QD [127] and next consider the design constraints of a QD IBSC [128]. With respect to the latter, a collection of localized states may result if there would exists non-uniformities in the QD matrix or if the inter-QD distance is large. If the localized intermediate states within the heterojunctions' confining potentials exist energetically close to one another, then they will create an energetic interval of allowed intermediate states, $\Delta\varepsilon_{\mathrm{IB}}$ (see Figure 20). With respect to either of the two cases, assuming that all the carriers in the intermediate states are in electro-chemical equilibrium, the population of carriers at intermediate states may be described by a single quasi-Fermi level, $\varepsilon_{\mathrm{FI}}$. If $\varepsilon_{\mathrm{FI}}$ is energetically close to the intermediate states, which may require the inclusion of dopants [60, 128, 129], then there is strong likelihood that absorbed photons may induce electronic transitions between the intermediate states and the conduction and valence band continua, respectively.

Previous work on the QD IBSC revolves around the InAs/GaAs (confined/barrier) [41, 62, 63, 64] and InGaAs/GaAs [65] material systems, both grown on GaAs substrates. These choices derive from the systems being relatively well understood. In addition, the bandgap of a GaAs barrier is near to the optimum conduction-to-valence bandgap associated with the upper limiting efficiency of an IBSC [35]. These materials systems have two characteristics limiting their usage for development of an QD IBSC: they have valence band discontinuities and they accumulate strain. The first characteristic (type-I heterojunction) enables the luminescent spectra of QD IBSC samples [41, 62] to illustrate narrowly separated and overlapping peaks, rather than the luminescent signature of an intermediate band material. The most rudimentary signature is the appearance of three [83] (or four [98]) strong luminescence peaks separated across a wide energy range; each of the three peaks corresponds to one of three allowed interband electronic transitions (whereas the fourth peak corresponds to an intraband transition [98]). The second characteristic (strain accumulation) causes the open-circuit voltage to degrade as the number of quantum-dot multi-layers increases [65]. This is a problem to the design of a high-efficiency QD IBSC, for a large number of multi-layers is essential for a high absorptivity of sub-bandgap photons [112] - the high absorptivity of sub-bandgap photons may be viewed experimentally by an increase

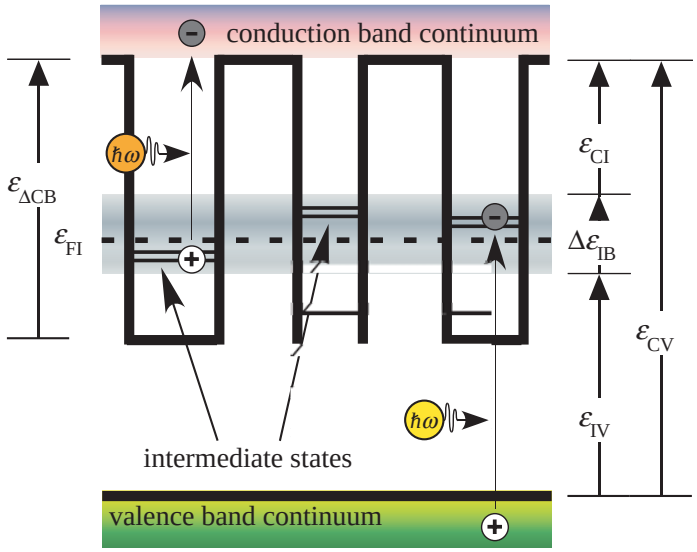

Figure 20: Energetic structure of an array of non-uniform quantum dot heterojunctions that would be favorable for a multiple transition solar cell's absorbing medium. Here, the valence band discontinuity is negligible, which precludes the existence of hole states in the formerly forbidden bandgap. Bound intermediate states within the heterojunctions' confining potentials, which are formed from the conduction band discontinuities, $\varepsilon_{\Delta CB}$, exist energetically close to one another. Inhomogeneities (*e.g* non-uniform dot sizes) broaden the interval of allowed intermediate states (gray hue) and create an energetic interval of allowed intermediate states, $\Delta\varepsilon_{IB}$. The minimum energetic distances between the intermediate states and the conduction band continuum and valence band continuum are ε_{CI} and ε_{IV}, respectively. Assuming that all the carriers in the intermediate states are in electro-chemical equilibrium, their occupancy statistics may be described by a single quasi-Fermi level, ε_{FI}.

in their external quantum efficiencies with an increase in the number of QD layers [65]. This chapter's design rules identify candidate material systems that may overcome these two characteristics.

The candidate material systems identified here yield heterojunctions at the transition between type-I and type-II heterojunctions and the potential for strain compensation. Heterojuntions at the transition between type-I and type-II exclusively permit bound states due either to hole(s) or to electron(s), but not both. This choice is meritorious for several reasons. First, it abates the difficulty in interpreting data from inter-band, optical experimental methods that exists if both holes and electrons are involved [130]. Second, it may limit the extension of the band edge into the previously forbidden bandgap [61], which would reduce the open-circuit voltage when compared to a control cell without QD [131]. Third, it may limit the accumulation of excess miniband formation [131]. Further, material systems that compensate strain accumulation permit the realization of longer, optically-active, multi-layered QD structures fabricated without generating [132, 133, 134, 135, 136] and propagating large number of defects, which decrease the open-circuit voltage. The literature presents several techniques to introduce strain compensating epitaxial layers [137, 138, 139], which permit fabricating optically-active QD structures comprised of 100 or more QD multilayers [140, 141].

Beyond the quantum well solar cell with quasi-Fermi level variations [56] and the QD IBSC [59], the design features and candidate material systems identified here may find use in developing related photovoltaic technologies and other opto-electronic devices. In addition, the candidate systems are of import to the fundamental physical study of heterojunctions. Within the photovoltaic field, the operating principles of several devices (*i.e.* multi-band solar cells [38]; and up-[142] and down-converters[120]) all rely on absorbers admitting multiple photo-induced electronic transitions. With respect to the physical import, type-II heterojunctions are theoretically predicted [143] and experimentally verified [144] as having relatively long radiative lifetimes resulting from the spatial division of confined electrons and holes. In addition, the nature of electronic conduction is shown to differ in type-I and type-II heterojunctions [145]. Therefore, the study of systems at the transition between

type-I and type-II systems warrants attention and may eventually lead to novel devices and device applications.

4.3 Design Rules

Seven quantitative design rules are specified to identify candidate material systems for nanostructured absorbers that are suitable for solar cells with multiple transitions. The first and second design rules are discussed extensively in the introductory section. The third and fourth design rules pertain to the placement of the intermediate states to permit, in principle, $\geq 50\%$ conversion under a solar concentration of at least $\times 1000$ Suns. The remaining rules assist in identifying candidates that offer an advantage in terms of minimizing the technological complexity of fabrication and characterization.

Negligible valence band discontinuity The first design rule specifies that the upper VB edge of the confined material must be continuous with the upper VB edge of the barrier material (see Figure 20). The absence of a valence band discontinuity eliminates the possibility of introducing intermediate states resulting from quantum confined holes. There are two reasons why the VB discontinuity is set to a negligible value rather than the CB discontinuity. First, in the technologically realizable interval of QD radii, for even a small VB discontinuity, many hole states appear; however fewer electron states appear with a similar magnitude CB discontinuity. This result stems from the fact that the technologically important III-V semiconductors have larger hole effective masses than electron effective masses [146]. Thus, within technologically realizable QD radii, it is possible to provide a single electron state within the confining potential, whereas, at those same radii, many hole states would exist. Second, in general, for the technologically important III-V semiconductors, the hole mobilities are less than the electron mobilities. In an actual device, the higher the mobility of the carriers is, the higher the diffusion length is for a given carrier lifetime. Thus, the mobility, through the diffusion length, enhances the collection of generated electron-hole pairs, and hence the performance of the device.

Substrate's lattice constant between those of the confined material and the barrier material The second design rule specifies inequalities relating the lattice constants of the confined, barrier, and substrate materials. Specifically, the lattice constant of the substrate must be between the lattice constants of the barrier and the confined materials. Material systems complying with this rule may allow the incorporation of tensile strain to compensate for compressive strain accumulated during the growth of the multi-layer quantum well [93, 147] and QD structures [137]. Strain compensation reduces the density of defects in multi-layer QD structures [148]. Thus, strain compensation is relevant to the number of QD layers, which has a direct impact upon the absorptivity of sub-bandgap photons [112], that can be incorporated into multi-layer structures before relaxation occurs. Further, the reduced density of defects in multi-layer QD structures [148] abates large open-circuit voltage losses in experimental samples [41, 65].

Barrier's bandgap between 1.25 eV and 3.13 eV The third design rule specifies the required interval of the conduction-to-valence bandgap, $\varepsilon_{\mathrm{CV}}$. In a previous examination of the QD IBSC [59], a bandgap of 1.95 eV is considered necessary for candidate barrier materials. This consideration is derived from detailed balance calculations [35] where the solar irradiance is concentrated at $\times 46\,000$, which is the physical limit of geometrical concentration (*i.e.* the reciprocal of the geometrical dilution factor [5]). The bandgap of 1.95 eV is associated with the apex of the efficiency curve found there. Here, the present author considers a more practical geometrical concentration factor of $\times 1000$. In addition, unlike previous calculations [35], when obtaining the maximum-power detailed balance efficiencies, the author includes the following as parameters in the search space: the energetic width of intermediate states [36], and the spectral extent of absorption overlap [84]. Similar to previous calculations [35], all calculations here are performed in the limit where electronic transitions are coupled to radiative interactions with the absorber. To what extent this is actually the case may be determined by future experimental investigation.

Figure 21 shows the upper theoretical maximum power iso-efficiency contour plot of an IBSC under a geometric concentration of $\times 1000$. Allowing that the energetic widths of

intermediate states corresponding to these efficiencies are negligible - which is the case in the high efficiency regime ($\geq 50\%$) - inspection of Figure 21 reveals that conduction-to-valence bandgap must be between 1.25 eV and 3.13 eV. Before moving on to the next design rule, the author points out an advantage of computing a two-dimensional iso-efficiency contour plot as compared to the one-dimensional plot previously presented in the literature [35]. This advantage stems from the fact that the complete set of ordered pairs $(\varepsilon_{\mathrm{IV}}, \varepsilon_{\mathrm{CI}})$ that result in efficiencies greater than 50% is visible. The upshot is a larger search space with which to apply the design rules, and hence a greater likelihood of obtain suitable material systems.

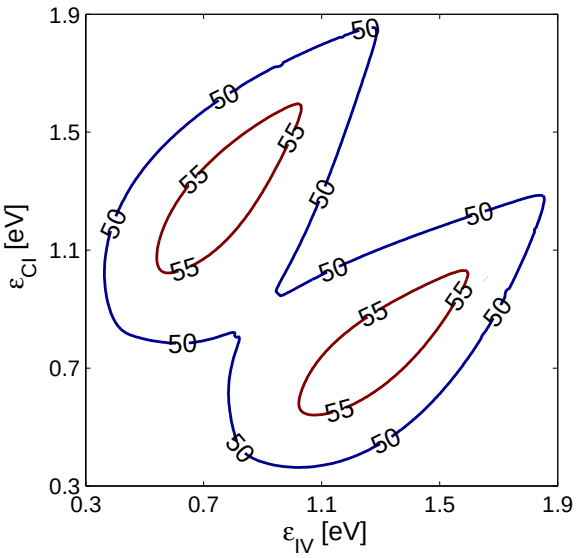

Figure 21: Maximum power iso-efficiency contour plot of an intermediate band solar cell under a geometric solar concentration of $\times 1000$ (shown here are the 50% and 55% contours) as a function of the energetic gaps, $\varepsilon_{\mathrm{IV}}$ and $\varepsilon_{\mathrm{CI}}$ (see Figure 20). Contours obtained using the rapid and precise computation method of Ref. [122]

Conduction band discontinuity accommodates states associated with high efficiencies The fourth design rule specifies the minimum value of the conduction band discontinuity, $\varepsilon_{\Delta \mathrm{CB}}$, which defines the confining potential (see Figure 20). This rule demands that the confining potential's depth accommodates positioning the intermediate states to enable high-efficiency solar energy conversion. The minimum quantitative value for the conduction band discontinuity depends upon the conduction-to-valence bandgap. These values

are obtainable from the data comprising the iso-efficiency contour plot (see Figure 21).

Direct bandgaps The fifth design rule demands that both the confined material and barrier material must be direct bandgap materials. For high-efficiency approaches, especially where the height of the absorbing medium may be limited by existing fabrication techniques, it is essential to have the largest absorptivity possible. For this reason, indirect bandgap materials, which require phonon exchange for light absorption, are excluded because their absorption coefficients are lower than those of direct bandgap materials. Further, the use of an indirect bandgap barrier requires thicker devices to significantly trap light and a longer duration of epitaxial growth, which may increase the opportunity for defect formation.

Confined material or barrier material is a binary semiconductor The sixth design rule simplifies the technological complexity of the multi-stack fabrication process. It is indubitably simpler to epitaxially fabricate a binary semiconductor than a ternary or quaternary semiconductor.

Substrate is commercially available The seventh design rule stipulates that the substrate must be commercially available. In general, the crystalline quality of devices grown by molecular beam epitaxy is much better if the substrate is commercially available. In addition, the experimental repeatability of measurements is more likely if the substrate is subject to industrial process control. At the time of writing, the following materials are commercially available: InP, GaAs, and InAs.

The design rules offer quantitative criteria to identify material system suitable for multiple transition solar cells implemented with nanostructures. These rules may be applied to a set of sufficiently characterized materials, as is done below.

4.4 Application to the III-V Semiconductors and their Ternary Alloys

The design rules are applied to the technologically important III-V zinc-blend and wurtzite compound semiconductors and their ternary alloys. Specifically, the following compounds and their ternary alloys are considered for any of the three components (*i.e.*, confined,

barrier, or substrate) of the material system: GaAs, GaSb, GaP, GaN, AlAs, AlSb, AlP, AlN, InAs, InSb, InP, and InN. The following parameters for all these binaries and their ternary alloys are required to identify material systems that conform to the design rules: a_{lc}, the lattice constant; E_{g}^{Γ}, the band in the Γ valley; E_{g}^{X}, the bandgap in the X valley; E_{g}^{L}, the bandgap in the L valley; VBO, the valence band offset; and, when available, $\alpha\left(\Gamma\right)$, $\beta\left(\Gamma\right)$, $\alpha\left(X\right)$, $\beta\left(X\right)$, $\alpha\left(L\right)$, and $\beta\left(L\right)$, the Varshni parameters of the Γ, X, and L bandgaps, respectively. The review of Vurgaftman *et. al.* is the sole source of information used by the author in modeling these material properties [146].

The design rules are applied to the technologically important III-V semiconductors at two distinct temperatures. These temperatures are 300 K, the terrestrial operating temperature of a solar cell, and 4 K, a temperature at which a significant amount of research and development of these types of material systems is likely to be performed [83, 98]. At both temperatures only the following material systems are identified: $\mathrm{InP}_{0.85}\mathrm{Sb}_{0.15}$/GaAs/InP, $\mathrm{InAs}_{0.40}\mathrm{P}_{0.60}$/GaAs/InP, $\mathrm{InAs}_{0.40}\mathrm{P}_{0.60}$/GaAs/InP, InAs/$\mathrm{GaAs}_{0.88}\mathrm{Sb}_{0.12}$/InP, and InP/ $\mathrm{GaAs}_{0.70}\mathrm{P}_{0.30}$/GaAs. Table 4 gives the conduction-to-valence bandgaps and conduction band discontinuities of these material systems at both 300 K and 4 K. It need be noted that at 300 K the band alignments of both the InAs/GaAsSb/InP and InP/GaAs/GaAs material systems may yield, in principle, a conversion efficiency between 48% and 50%. They are included here to provide material systems whose quantum confined regions are composed of a binary semiconductor.

Negligible valence band discontinuities are experimentally inferred for two of these four systems: InAsP/GaAs [149, 150], and InAs/GaAsSb [151, 152]. As regards the QD IBSC, InAs/GaAsSb structures offer the most promise. There are two reasons for this. First, antimonide acts as surfactant [153, 154], which inhibits the generation of interfacial defects and thus leads to superior optical activity [155]. Second, it is indubitably less complex to constitute binary QD within a ternary barrier than *vice versa*. The following concludes these findings.

Table 4: Material systems with which to implement nanostructured absorbers for multiple transition solar cells. Given for each system is the confined material, the barrier material, and the optimum maximum-power conversion efficiency, η_{opt}, at 300 K and $\times$1000 concentration. Additionally given are the conduction-to-valence bandgap, $\varepsilon_{\mathrm{CV}}$, and the conduction band discontinuity, $\varepsilon_{\Delta\mathrm{CB}}$, at both 300 K and 4 K (300 K/4 K). The systems given in the first three rows require InP substrates, whereas that of the fourth row requires a GaAs substrate.

Confined	Barrier	η_{opt} [%]	$\varepsilon_{\mathrm{CV}}$ [eV]	$\varepsilon_{\Delta\mathrm{CB}}$ [eV]
$InP_{0.85}Sb_{0.15}$	GaAs	53	1.42/1.52	0.49/0.51
$InAs_{0.40}P_{0.60}$	GaAs	53	1.42/1.52	0.49/0.52
InAs	$GaAs_{0.88}Sb_{0.12}$	48	1.18/128	0.83/0.86
InP	$GaAs_{0.70}P_{0.30}$	49	1.79/189	0.43/0.46

4.5 Conclusions

Four candidate material systems are identified for further development of multiple transition solar cells implemented with nanostructures. The materials systems provide heterojunctions at the transition between type-I and type-II heterojunctions, resulting from their negligible valence band discontinuities, and offer the possibility for strain compensation during the growth of multi-layer quantum dot structures. Resultant from several advantageous properties, the InAs/GaAsSb is particularly suited to further investigation of a quantum dot intermediate band solar cell. A key tool used to identify these material systems is a maximum power iso-efficiency contour plot of an intermediate band solar cell under a geometric concentration of $\times$1000.

CHAPTER V

ABSORPTION AND EMISSION BASED ON PARABOLIC BANDS

5.1 Introduction

In this chapter the author details the absorption and emission of three-transition absorbers based on parabolic-band approximations. In Section 5.2, the author models the absorption coefficients of an intermediate-band absorbing medium. In addition, equilibrium absorption coefficients are presented for several absorbers, each distinguished by their energy-wavevector dispersion and equilibrium temperature. Several simplifying assumptions are made including that the energy-wavevector dispersions are parabolic. The model requires the absolute locations of three quasi-Fermi levels. This is made possible by using two balance equations. One of these, a charge-neutrality condition, requires the numerical computation of the carrier statistics in each band of the absorbing medium. The use of Fermi-Dirac integrals make this possible. Conclusions are drawn regarding the completeness of absorption, the existence of absorption overlap, and the temperature-dependence of the absorption. In Section 5.3, the author presents theoretical photoluminescent spectra of absorbing media, each with valid quantum states forming an intermediate band. The novelty is illustrating the spectroscopic consequences of multi-gap absorbers whose quantum states form parabolic bands. Photoluminescent spectroscopy allows the band-edges of multiple transition solar cells to be investigated without the additional complication of fabricating electrical contacts. Results are presented for absorbers with the same bandgaps, yet they each have distinct absorption characteristics, temperatures, and lengths. The author draws two conclusions. First, the photoluminescent intensity of an intermediate band absorber may be appreciable within four distinct and well-separated spectral bands. Second, the full width at half maximum of the spectral band in the infrared regime approximates the width of the intermediate band.

5.2 Absorption Coefficients of under Parabolic-Band Approximations

5.2.1 Introduction

In this section the author models the absorption coefficients of intermediate-band [52] (IB) absorbing media. Such media may permit multiple photo-induced electronic transitions [20]. The literature offers several candidate material systems to implement such media [46, 48, 78, 72, 73, 59, 60, 41, 66]. Though they differ on a case-by-case basis, the electronic structures of the candidate materials systems have similarities. Here, the technical approach is to model the gross electronic features with parabolic bands and to consider the absorption resulting from momentum-conserving photo-induced electronic transitions. The absorption coefficients are necessary to determine the radiative flows pumped into and sunk out of such media [44], and hence are pertinent to the performance of a variety of potential applications. In particular, Section 5.2 addresses two open questions in the science of solar energy conversion and distinguishes the absorption at distinct equilibrium temperatures.

Reynolds and Czyzak postulate an absorbing medium with a band between the conduction band (CB) and valence band (VB) as a mechanism for photovoltaic and photoconductive effects in crystals [52]. The reduced band diagram of such a medium is illustrated in Figure 22. Here, the IB has well-defined band edges and band width, which may require some measure of order [45] (for a general discussion, see [126] and references therein). Shockley and Read [43] explain that the occupancy of the conduction, intermediate, and valence states are described by distinct quasi-Fermi levels. Here the author labels these as $\varepsilon_{\mathrm{F,CL}}$, $\varepsilon_{\mathrm{F,IH}}$ or $\varepsilon_{\mathrm{F,IL}}$, and $\varepsilon_{\mathrm{F,VH}}$, respectively. Resulting from the existence of the intermediate quantum states, multiple photo-induced transitions may be possible within the medium [20]. Photo-induced electronic transitions are possible between the states of the IB and the states of CB and VB states, respectively, as well as between states of the CB and VB. In addition, resulting from the possible existence of occupied and unoccupied states [126], photo-induced intraband electronic transitions are likely between two distinct states in the IB [44].

Several approaches are given to realize an absorber with a band of intermediate quantum states. These include III-V semiconductor alloys with transitional metal substitution [46],

highly mismatched alloys [48, 78], II-VI semiconductors alloys with transitional metal substitution [72], transition metal doped chalcopyrite semiconductors [73], and quantum dots crystals [59, 60, 41, 66]. *Ab initio* theoretical surveys of semiconductor alloys using periodic density functional theory [46, 156, 72, 73], and a band anticrossing model of the oxide semiconductor alloys [48], both indicate the existence of an IB of quantum states; whereas Kronig-Penney solutions of quantum dot crystals [127] indicate the possibility of one or more minibands. The energy-wavevector dispersion curves of the intermediate states, vary on a case-by-case basis, but they have in common clearly defined energetic band widths and band edges. The energetic width of the minibands formed by the quantum dot crystals may be up to the order of tens of meV [127], depending on the inter-dot spacing. The energetic widths of the IBs of semiconductor alloys range from the order of hundreds of meV [48, 156, 72, 73] to the order of 1 eV [46].

The technical approach taken here is to treat the intermediate quantum states as a continuum of states. Similar to the pioneering work on inter-band absorption of semiconductors and insulators [121, 157, 158, 159], the present author approximates the ε-k dispersion of the bands as parabolic functions. The author uses these approximations with cognizance that these are less and less realistic proceeding further from the band edges. Further, the approach utilizes effective mass parameters to quantify the concavity of the ε-k curves. The author notes that the applicability of the effective mass approximation to semiconductor

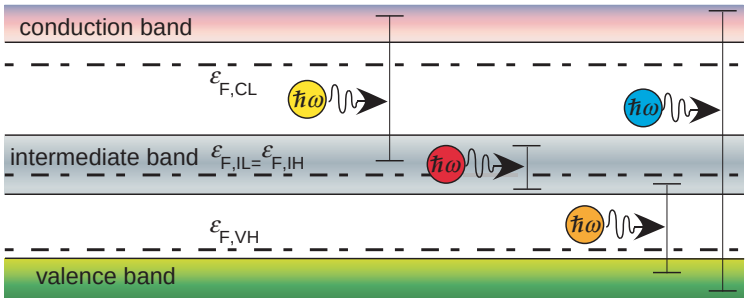

Figure 22: Reduced band diagram of an intermediate-band absorbing medium. Electronic levels are confined to three electrically isolated band continua. Shown are the quasi-Fermi levels, $\varepsilon_{F,X}$, and allowed photo-induced electronic transition (three interband and one intraband).

alloys with deep quantum states may be limited to those whose deep states result from isocoric substitutions [160]. Similar to the ε-k dispersion given elsewhere [161], the present authors' approach allows direct transitions at intermediate levels only within a well-defined and continuous interval of wavevectors. The maximum wavevector may be related to the effective Bohr radius [161, 126] and the IB width may be related to the concentration of atoms contributing to the intermediate states [45]. The technical approach here contrasts with previous models of quantum dot absorption [162, 163, 164] and also with previous absorption models of impurity absorption [161]. In those, the absorption coefficients are given for discrete intermediate levels, rather than a band of intermediate quantum states. An additional important contrast is that the model here is unique in that it allows for the calculation of the absorption coefficients far from equilibrium. The approach here provides insight into the gross features of the absorption in IB absorbing media; more detailed treatments of the absorption characteristics of such absorbers may be determined on a case-by-case basis by fundamental absorption studies [156].

The normalized absorption coefficients and the cumulative absorption coefficient (via the absorptivity [13]) determine how incident radiative flows are pumped into an IB absorber [44]. Additionally, they are explicitly related to the emission spectrum of an IB absorber, which determines the radiative flows sunk by the IB absorber [44]. The absorption coefficients are thus pertinent to the performance of a host of devices that may employ such absorbers. These applications include up- [165] and down-converters [115], multi-transition solar cells [20, 35, 36], unstacked multi-color light emitting diodes [116] and unstacked multi-color photo-detectors [166, 167, 168, 117].

The remainder of Section 5.2 is organized as follows. In Section 5.2.2 the simplifying assumptions of the approach are made explicit. Next, in Section 5.2.3 the absorption coefficients are written explicitly based on these assumptions. Next, in Section 5.2.4 the approach is employed to illustrate several salient features of the equilibrium absorption coefficients. Here, the author addresses two open questions in the science of solar energy conversion. The first is determining to what extent the concentration of intermediate quantum states adjusts the absorption characteristic so that photons with energies greater than the smallest

bandgap are fully absorbed [20]. The second is determining to what extent the intermediate quantum states produce absorption overlaps [84], which is directly related to the normalized absorption coefficients[44]. Next, in Section 5.2.5 conclusions are offered.

5.2.2 Simplifying Assumptions

The approximation of the absorption coefficients is premised upon several simplifying assumptions regarding the absorbing medium. First, it is assumed that the ε–k dispersions may be defined as parabolic with respect to the wavevector and further that the ε–k dispersion of the IB is continuous with respect to the energy levels comprising the IB. Second, it is assumed that the bandgaps between the bands are direct (*i.e.*, the onsets of all inter-band optical transitions occur at a single wavevector). Third, it is assumed that the matrix elements of momentum may be given by the electric dipole approximation (see for example the reference here [169]) with the further simplification that the electric dipole matrix elements are constant with respect to the wavevector. Fourth, it is assumed that momentum-conserving electronic transitions (direct transitions) are allowed and further that they predominate over indirect transitions, so that indirect absorption may be ignored. The following section presents the formalism of calculating the absorption coefficients based on these simplifying assumptions.

5.2.3 Formalism

This section is divided into three subsections. Subsection 5.2.3.1 illustrates the energy-wavevector dispersion curves of the model, with all important features labeled and defined. Subsection 5.2.3.2 quantifies the absorption coefficients. There it is shown that calculating the absorption coefficients requires the absolute locations of the quasi-Fermi levels. Subsection C provides a method to determine the absolute locations of the quasi-Fermi levels.

5.2.3.1 Dispersion Curves

Based on the first two assumptions, the resulting ε–k dispersion model of an IB absorber is illustrated graphically in Figure 23. The energy versus wave-vector dispersion is given by four curves: the conduction and valence bands are each given by a single parabolic

function, while the IB is given as two piecewise-continuous parabolic functions. The CB edge, $\varepsilon_{\mathrm{CL}}$; the VB edge, $\varepsilon_{\mathrm{VH}}$; and the upper and lower IB edge, respectively $\varepsilon_{\mathrm{IH}}$ and $\varepsilon_{\mathrm{IL}}$, are labeled. The reader may note by inspection that the absorber is uniformly a direct-bandgap material; thus, all the bandgaps are defined at an identical wavevector, namely, k_0. The bandgaps are defined as $\varepsilon^{k_0}_{(\mathrm{CL,VH})}$, $\varepsilon^{k_0}_{(\mathrm{CL,IH})}$, and $\varepsilon^{k_0}_{(\mathrm{IL,VH})}$. Additionally defined at k_0 are the energetic differences between the CB and the lower intermediate subband; the upper intermediate subband and the valence band; and the upper and the lower intermediate subbands, which are $\varepsilon^{k_0}_{(\mathrm{CL,IL})}$, $\varepsilon^{k_0}_{(\mathrm{IH,VH})}$, and $\varepsilon^{k_0}_{(\mathrm{IH,IH})}$, respectively. The concavity of the CB, the upper and the lower intermediate subbands, and the valence band dispersions are given by their respective effective masses: m_{CL}, m_{IH}, m_{IL}, and m_{VH}. That the ε–k dispersion of the IB is continuous, the subbands comprising the IB meet at a specific wavevector. This wavevector, k_{max}, and the absolute energetic position of the intermediate states there, $\varepsilon_{k_{\mathrm{max}}}$, may be solved algebraically [170]. The results are

$$k_{\mathrm{max}} = \sqrt{\frac{2\,\varepsilon^{k_0}_{(\mathrm{IH,IL})}\,m_{\mathrm{IL}}\,m_{\mathrm{IH}}}{\hbar^2\,\left(m_{\mathrm{IL}}+m_{\mathrm{IH}}\right)}} \text{ and} \tag{21}$$

$$\varepsilon_{k\mathrm{max}} = \frac{\varepsilon_{\mathrm{IH}}\,m_{\mathrm{IH}}+\varepsilon_{\mathrm{IL}}\,m_{\mathrm{IL}}}{m_{\mathrm{IL}}+m_{\mathrm{IH}}}, \tag{22}$$

where $\hbar$ is Planck's constant. At k_{max} the energetic distances between the intermediate levels and the conduction and valence bands, respectively, may also be solved algebraically [170]. The results are

$$\varepsilon^{k_{\mathrm{max}}}_{\mathrm{CI}} = \varepsilon^{k_0}_{(\mathrm{CL,IH})} + \frac{\left(\hbar\,k_{\mathrm{max}}\right)^2}{2}\left(\frac{1}{m_{\mathrm{CL}}}+\frac{1}{m_{\mathrm{IH}}}\right) \text{ and} \tag{23a}$$

$$\varepsilon^{k_{\mathrm{max}}}_{\mathrm{IV}} = \varepsilon^{k_0}_{(\mathrm{IL,VH})} + \frac{\left(\hbar\,k_{\mathrm{max}}\right)^2}{2}\left(\frac{1}{m_{\mathrm{IL}}}+\frac{1}{m_{\mathrm{VH}}}\right), \tag{23b}$$

respectively. As constructed, photo-induced electronic transitions at intermediate levels are impermissible beyond k_{max}. The effects of this are seen clearly in the illustrations of the equilibrium absorption coefficients found in section 5.2.4.3.

Inspection of Figure 23 indicates that the simplifying assumptions must yield a total of six possible momentum-conserving photo-induced electronic transitions. The set of allowed momentum-conserving transitions, $\mathcal{T}$, is thus given as $\mathcal{T}$ = {(CL,VH), (CL,IH), (IL,VH),

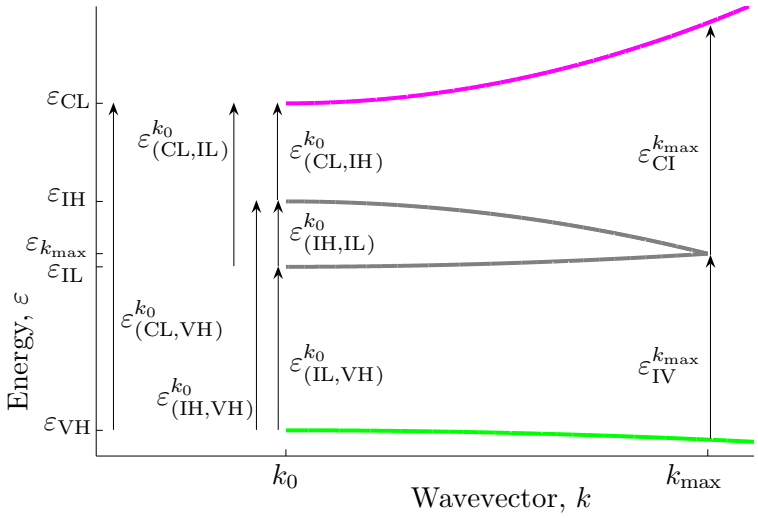

Figure 23: Energy-wavevector (ε-k) dispersion diagram of a direct-gap intermediate-band absorbing medium under parabolic approximations. The intermediate band is comprised of two subbands.

(IH,IL), (CL,IL), (IH,VH)}. The elements of set $\mathcal{T}$ refer to electronic transitions between the CB and valence band; CB and upper subband of the IB; upper subband of the IB and valence band; upper subband of the IB and lower subband of the IB; CB and lower subband of the IB; and upper subband of the IB and valence band, respectively.

The following subsection utilizes the dispersion curves and renders expressions for the absorption coefficients of the absorbing medium.

5.2.3.2 Absorption Coefficients

The approach taken here derives the absorption coefficients for each of the momentum-conserving electronic transitions in a manner similar to the derivation for a direct bandgap semiconductor near its absorption edge [121, 157, 158, 159]. In general, modeling the absorption coefficients of semiconductors with parabolic-band approximations is tenuous away from the band edges; nonetheless, the gross features manifest. Based on the four simplifying assumption, the absorption coefficients, $\alpha_{(\mathrm{X,Y})}(\hbar\omega)$, of a simplified IB absorber are modeled in Appendix C. To utilize this model, certain parameters, which are listed in Table 5, are required. These parameters include the absolute energetic positions of the

quasi-Fermi levels, which may be obtained with the method detailed in Appendix C. Having outlined the formalism required to model the absorption coefficients of an IB absorbing medium, attention is now turned to an explicative example of its usage.

Table 5: Minimum set of scalar variables required to approximate the absorption coefficients of an intermediate-band absorbing medium. These variables may be obtained from empirical data, theoretical considerations, or semi-empirical models.

variable	symbol
band edges	$\varepsilon_{\mathrm{CL}}$, $\varepsilon_{\mathrm{IH}}$, $\varepsilon_{\mathrm{IL}}$, $\varepsilon_{\mathrm{VH}}$
effective masses	m_{CL}, m_{IH}, m_{IL}, m_{VH}
matrix elements	x_{VC}, x_{IC}, x_{VI}, x_{II}
optical index of refraction	n_{op}
quasi-Fermi levels	$\varepsilon_{\mathrm{F,CL}}$, $\varepsilon_{\mathrm{F,IH}} = \varepsilon_{\mathrm{F,IL}}$, $\varepsilon_{\mathrm{F,VH}}$
absorber temperature	T_{c}

5.2.4 Explicative Example

In this section, explicative examples are offered to illustrate and explain several salient features [171] of the absorption characteristic of IB absorbers. Here the author addresses two open questions stated in the introduction, as well as distinguish the absorption characteristics at distinct temperatures. In Section 5.2.4.1, the model parameters are given and justified. In Section 5.2.4.2, the equilibrium carrier statistics of this system are explained. Finally, in Section 5.2.4.3, the equilibrium absorption coefficients are presented and explained.

5.2.4.1 Model Parameters

The model parameters of the examples are given in Table 6. Parameters relating to the CB and VB are those relating to $GaAs_{0.88}Sb_{0.12}$, which is the host semiconductor of an IB absorbing medium identified for high-efficiency solar energy conversion [66]. These are calculated at room temperature from the band parameters of III-V semiconductors and their ternary alloys [146]. The location of the IB is centered at the value corresponding to high-efficiency solar energy conversion [66]. The width of the IB is typical of several

of the identified IB absorbing medium [48, 156, 72, 73]. The matrix elements are given in terms of the Kane energy, E_P, which takes a value within the accepted range of those for various semiconductors [172]. In addition, it is assumed that only 2/4 (each photo-induced electronic transition occurs between only two of the four dispersion curves) of the oscillator strength contributes to the matrix elements. The model assumes that the hole and electron effective masses in the IB's subbands are equal. For pedagogical simplicity, the model parameters are not altered with temperature. The following subsection describes the carrier statistics of this system.

Table 6: Model parameters for the explicative examples. Some parameters given in terms of the electron rest mass, m_o.

Variable	Value
$\varepsilon_{\mathrm{CL}}$	0.59 eV
$\varepsilon_{\mathrm{IH}}$	0.25 eV
$\varepsilon_{\mathrm{IL}}$	0.15 eV
$\varepsilon_{\mathrm{VH}}$	-0.59 eV
m_{CL}	$0.051\, m_o$
$m_{\mathrm{IH}} = m_{\mathrm{IL}}$	Depends on $k_{\max}$; see Equation (42)
m_{VH}	$0.57\, m_o$
$x_{(\mathrm{X,Y})}$	$\frac{\hbar}{\frac{k_0}{\varepsilon_{(\mathrm{X,Y})}}}\mathrm{sqrt}\left(\frac{2}{4}\right)\mathrm{sqrt}\left(\frac{1}{2}\frac{E_P}{m_o}\right)$
E_P	20 eV
n_{op}	1
T_{c}	10 K or 300 K

5.2.4.2 Equilibrium Fermi Energy

Knowledge of the equilibrium Fermi energy of an IB absorber is prerequisite to interpret its equilibrium absorption coefficients. To locate the equilibrium Fermi energy, $\varepsilon_{\mathrm{F}i}$, Equation (36) is solved for the special case where the quasi-Fermi levels are all equal to $\varepsilon_{\mathrm{F}i}$. Figure 24 illustrates the equilibrium Fermi energy as a function of temperature for absorbers with distinct concentrations of intermediate states, G_{I}, which is defined in Equation (42).

At one extreme, when the concentrations of electrons in the CB and holes and VB

are both very small compared with the concentration of intermediate states, the charge-neutrality condition indicates that the concentration of holes and electrons in the IB are in balance. Therefore, at low temperatures, where the thermally generated population of CB and VB carriers is low, the equilibrium Fermi level is within the IB. In this example, by construction, the carrier statistics of holes and electrons in the IB are symmetric; therefore, the intrinsic Fermi level appears directly in the center of the band at low temperatures. At a second extreme, when the concentrations of electrons and holes in the CB and VB band are very large compared to the concentrations of the IB carriers, the charge-neutrality condition may be determined by the number of electrons and holes in the CB and VB, respectively. Thus, the position of the equilibrium Fermi level reduces to that determined from the canonical expression of the Fermi level of an intrinsic semiconductor. For cases between the two extremes, the equilibrium Fermi level will be located between those of the two extremes. For any given temperature, the larger the concentration of intermediate states, the closer is the Fermi energy to the first extreme and *vice versa*.

This investigation reveals that an IB absorbing medium may be metallic [10] or insulating. Further, the metal-insulator transition depends upon the concentration of intermediate states, the energetic width of the IB, and the carrier statistics of the CB and VB. In continuing to the next section, the reader should note that the IB media there are assured to be metallic at and below room temperature so long as the concentration of intermediate states is of order 10^{10} cm^{-3} or greater.

5.2.4.3 Absorption Characteristics

In what follows is a discussion of several salient features of the absorption characteristics. First, is a discussion of the completeness of light absorption and absorption overlap. Second, is a discussion that compares the absorption characteristics at distinct temperatures. Figure 25 presents the absorption coefficients of four distinct samples: in the first three panes (a-c) are samples in equilibrium at room temperature (300 K), whereas in the fourth pane (d) the sample is in equilibrium at a temperature closer to absolute zero (10 K). For each sample, the concentration of intermediate states is sufficient to ensure that the Fermi

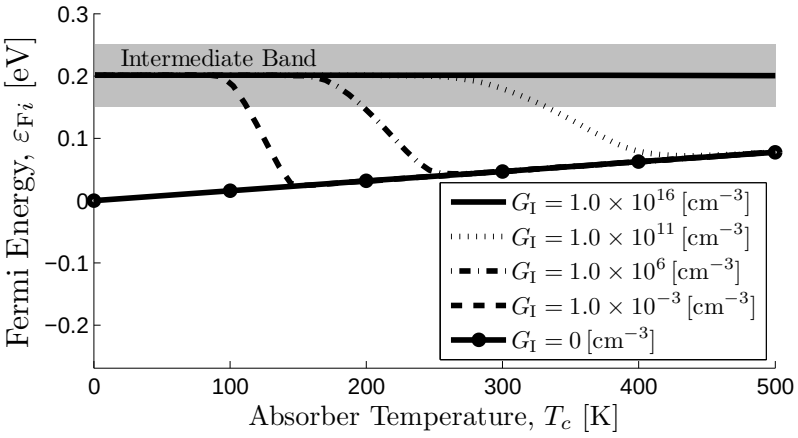

Figure 24: Equilibrium Fermi energy of intermediate-band absorbers as a function of temperature. Each medium is distinguished by its concentration of intermediate states, G_{I}.

energy is well within the IB. Thus, the electronic occupancy is favorable for absorption resultant from photons joining each of the interband electronic transitions [10].

Completeness and Overlap of Absorption Of general importance to high-efficiency solar-energy conversion are two criteria. First, is the absorption of photons within the broad range of high solar irradiance. Second, to first approximation, is that when multiple absorption paths exist, that photons interact with matter across the largest bandgap less than the photons' energies. This is because photon interaction with matter is associated with a rate of internal irreversible entropy generation, which increases monotonically with $\hbar\,\omega - (\varepsilon_{\mathrm{F,X}} - \varepsilon_{\mathrm{F,Y}})$ [24].

Figure 25 illustrates that sample (a) does not permit light absorption for all photons greater than the absorber's smallest bandgap. Sample (b), however, does permit light absorption for all these photons. However, for photons in the range $\left(\varepsilon^{k_0}_{(\mathrm{IL,VH})}, \varepsilon^{k_{\max}}_{\mathrm{IV}}\right)$ the absorption resultant from photo-induced interband electronic transitions between states in the VB and IB overlaps the absorption resultant from transitions between states in the IB and CB. Similarly, for photons in the range $\left(\varepsilon^{k_0}_{(\mathrm{CL,VH})}, \varepsilon^{k_{\max}}_{\mathrm{CI}}\right)$ the absorption resultant from photo-induced interband electronic transitions between states in the VB and IB overlaps the absorption resultant from photo-induced interband electronic transitions between states in the VB and CB. Sample (c) shows an additional absorption overlap, namely for photons in

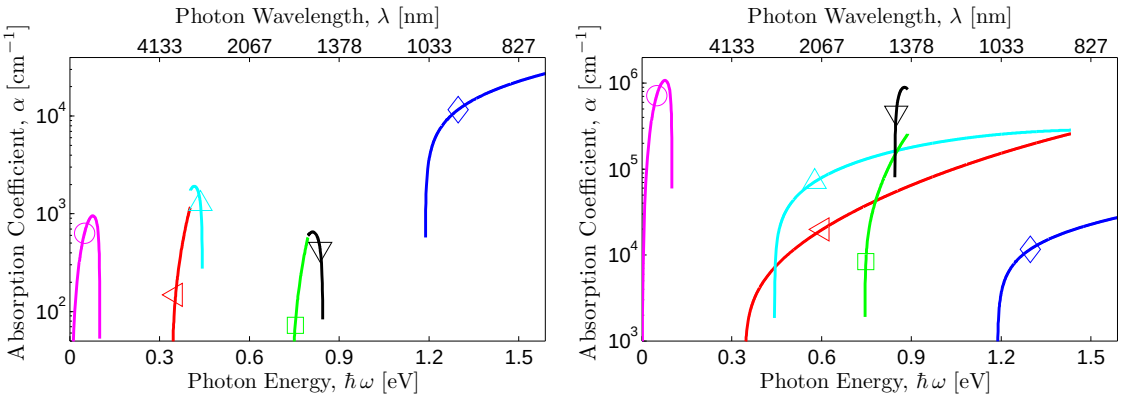

(a) $T_{\mathrm{c}} = 300\,\mathrm{K}$; $k_{\max} = 1.1 \times 10^{8}\,\mathrm{m}^{-1}$; $G_{\mathrm{I}} = 1.0 \times 10^{17}\,\mathrm{cm}^{-3}$

(b) $T_{\mathrm{c}} = 300\,\mathrm{K}$; $k_{\max} = 1.2 \times 10^{9}\,\mathrm{m}^{-1}$; $G_{\mathrm{I}} = 1.1 \times 10^{20}\,\mathrm{cm}^{-3}$

(c) $T_{\mathrm{c}} = 300\,\mathrm{K}$; $k_{\max} = 3.0 \times 10^{9}\,\mathrm{m}^{-1}$; $G_{\mathrm{I}} = 1.9 \times 10^{21}\,\mathrm{cm}^{-3}$

(d) $T_{\mathrm{c}} = 10\,\mathrm{K}$; $k_{\max} = 1.2 \times 10^{9}\,\mathrm{m}^{-1}$; $G_{\mathrm{I}} = 1.1 \times 10^{20}\,\mathrm{cm}^{-3}$

Figure 25: Equilibrium absorption coefficients for four distinct conditions. Each plot has six curves which are demarcated as: $\alpha_{(\mathrm{IH,IL})}$, $\alpha_{(\mathrm{CL,IH})}$, $\alpha_{(\mathrm{CL,IL})}$, $\alpha_{(\mathrm{IL,VH})}$, $\alpha_{(\mathrm{IH,VH})}$, $\alpha_{(\mathrm{CL,VH})}$.

the range $\left(\varepsilon^{k_0}_{(\mathrm{CL,VH})}, \varepsilon^{k_{\max}}_{\mathrm{CI}}\right)$. Here the absorption resultant from photo-induced interband electronic transitions between states in the IB and CB overlaps the absorption resultant from photo-induced interband electronic transitions between states in the CB and VB. In these explicative examples there is no situation that satisfies the two stated criteria.

According to the parabolic-band approximations, to obtain the complete absorption of photons greater than the smallest bandgap in the system without overlap, the following

inequality and two equalities must be satisfied (see Figure 23)

$$\varepsilon^{k_0}_{(\mathrm{IH,IL})} \leq \varepsilon^{k_0}_{(\mathrm{CL,IH})}, \tag{24a}$$

$$\varepsilon^{k_{\max}}_{\mathrm{CI}} = \varepsilon^{k_0}_{(\mathrm{IL,VH})}, \text{ and} \tag{24b}$$

$$\varepsilon^{k_{\max}}_{\mathrm{IV}} = \varepsilon^{k_0}_{(\mathrm{CL,VH})}. \tag{24c}$$

Here it is assumed $\varepsilon^{k_0}_{(\mathrm{CL,IH})} < \varepsilon^{k_0}_{(\mathrm{IL,VH})}$. Plugging in from Equation (23), the existence of the desired absorption is guaranteed so long as

$$\frac{m_{r,(\mathrm{CL,IH})}}{m_{r,(\mathrm{IL,VH})}} = \frac{\varepsilon^{k_0}_{(\mathrm{CL,IH})} - \varepsilon^{k_0}_{(\mathrm{IH,IL})}}{\varepsilon^{k_0}_{(\mathrm{IL,VH})} - \varepsilon^{k_0}_{(\mathrm{CL,IH})}}. \tag{25}$$

The next paragraph compares the absorption coefficients at distinct temperatures.

Comparative Absorption at Distinct Temperatures There are noticeable differences in the absorption characteristic at room temperature and at temperatures closer to absolute zero. In particular, as illustrated by comparing Figure 25(b) and Figure 25(d), the absorption coefficients $\alpha_{(\mathrm{CI,IH})}$ and $\alpha_{(\mathrm{IL,VH})}$ are significantly reduced at temperature near absolute zero. This is resultant from the sharpness of the Fermi-Dirac statistics $\overline{f}_{(\mathrm{CI,IH})}$ and $f_{(\mathrm{IL,VH})}$, respectively, at temperatures near absolute zero. Though the joint densities of states coupled to transitions (CL,IH) and (IL,VH) are appreciable, the states of the IB's upper subband are almost completely void of electrons with which to couple to the holes of the CB and the states of the IB's lower subband are almost completely void of holes with which to couple to the electrons of the VB. Thus, though rigorously the onsets of interband transition are those given in Table 9, the thresholds of appreciable absorption have much to do with the energetic difference between the location of the Fermi energy and the lower CB edge and upper VB edges, respectively. Thus, in the particular case of low-temperature absorption, the absorption edges may be depicted as in here [10].

The author now concludes the findings of Section 5.2.

5.2.5 Conclusions

Based upon four simplifying assumptions the author models an intermediate-band absorbing medium's absorption coefficients. From this, it is concluded that (i) if the concentration

of intermediate states is at least of order of the intrinsic carrier concentration of an equivalent medium that excludes the intermediate states, then the Fermi energy will exist within the band of intermediate quantum states. In such case, absorption resulting from each of the allowed photo-induced electronic transitions may be appreciable. In addition, it is concluded that (ii) it is possible that an absorbing medium with a multi-bandgap electronic structure may absorb all photons with energies greater than the smallest bandgap in the system. Further, it is concluded that (iii) though in principle there exists a criterion for complete absorption without concomitant absorption overlaps, achieving this criterion is non-trivial. Finally, (iv) it is concluded that at temperatures near absolute zero, the absorption edges resulting from transitions at intermediate levels may appear blue-shifted as compared with room-temperature absorption. This is resultant from a sharp change in the electronic occupancy of the states of the intermediate band around its quasi-Fermi level. In Section 5.3, the author uses the parabolic-band approximations to model the photo-emission from intermediate-band absorbers.

5.3 Photoluminescence based on Parabolic-Band Approximations

5.3.1 Introduction

This section presents theoretical photoluminescent spectra of intermediate band (IB) absorbing media. The work is relevant to several approaches that aim for high-efficiency solar energy conversion. These include multi-transition solar cells [20, 35, 36], and colloidal and epitaxial quantum dot solar cells [173], which may include multiple electron-hole pair generation [124]. Photoluminescent spectroscopy allows the band edges of absorbers to be investigated. Therefore, properties of an absorber that are relevant to photovoltaic solar energy conversion may be examined without the additional complication of processing an absorbing medium into an actual solar cell [83]. Previous research examining the photoluminescent properties of IB absorbing media does so only for the most ideal case [83], where, for example, the absorptivity is given as a linear combination of unit step functions.

The core novelty here is to illustrate the spectroscopic consequences of a multi-gap

absorber whose energy-wavevector dispersion is given by parabolic bands [96, 97] (see Figure 26). In particular, the author utilizes absorption coefficients based on parabolic-band approximations to calculate the photon flows pumped into and sunk out of the IB absorber [44]. The author stresses that calculating the absorption coefficients under the parabolic-band approximations requires the absolute locations of three quasi-Fermi energies. This as opposed to calculations of the photon flows of IB absorbers based on idealized absorption coefficients [35, 36, 83, 44, 10], where only the three quasi-Fermi energy separations need be identified.

The remainder of this section is organized as follows. In section two, the author reviews relevant assumptions of the parabolic-band approximations. There, specific details of the absorption characteristics of the IB absorber are highlighted. Subsequently, in section three, the author describes the procedure used to obtain the photoluminescent spectra. In section four, the author offers the spectroscopic consequences of the parabolic bands. The results presented are largely invariant with respect to any particular absorption characteristics. In section five, the author utilizes the invariance of the results to draw two conclusions.

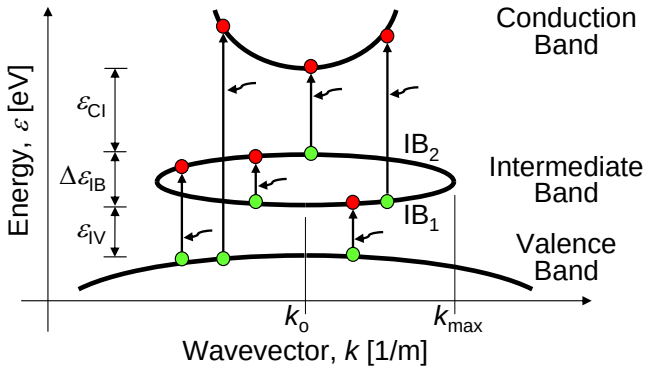

Figure 26: Energy-wavevector dispersion of a direct-gap intermediate-band absorbing medium under parabolic-band approximations. Photoluminescent spectra present here include contributions from six momentum-conserving photo-induced electronic transitions.

5.3.2 Parabolic-Band Approximations

The PL spectra obtained here utilize absorption coefficients for an IB absorbing medium based on parabolic-band approximations, which are described in more detail in references [96, 97]. This section is divided in three parts. First, the author reviews the major assumptions of the parabolic-band approximations. Second, the author explains the phenomenon of parallel absorption paths and distinguish this from ideal spectral selectivity. Third, the author clarifies the consequences of $k_{\max}$ and explain the role of $k_{\max}$ in the subsequent presentation of data.

5.3.2.1 Relavent Parabolic-Band Assumptions

Figure 26 depicts the parabolic energy-wavevector dispersion that is here considered. The IB is comprised of two subbands (IB_1 and IB_2) and has a non-infinitesimal bandwidth, $\Delta\varepsilon_{IB}$. The IB is separated from the conduction band (CB) and valence band (VB) by energetic gaps ε_{CI} and ε_{IV}, respectively. As shown, the model supposes a direct-gap medium so that the band extrema occur at the same wavevector, namely ko, which can be, for simplicity and without loss of generality, assumed to equal zero. The parabolic-band approximation assumes that each quantum state in the IB has a wavevector between k_o and $k_{\max}$ (see Figure 26). as shown in Figure 26, six momentum-conserving, photo-induced electronic transitions resulting from the parabolic-band approximations.

5.3.2.2 Parallel Absorption Paths

Each of the momentum-conserving, photo-induced electronic transitions has a quantifiable onset and offset of optical absorption. Both depend on the difference between k_o and $k_{\max}$ [96, 97]. The onset of absorption is that energy at which the absorption coefficient transitions from zero to a non-zero value and *vice versa* for the offset. A photon with an energy in the range $(\hbar\omega, \hbar\omega + d\hbar\omega)$ may induce any electronic transition whose onset of optical absorption is less than or equal to the photon's energy and whose offset of optical absorption is greater than the photon's energy. In other words, if in the range $(\hbar\omega, \hbar\omega + d\hbar\omega)$ the IB absorber's absorption characteristic has an absorption overlap [84], more than one

of the absorption paths are available to photons within this range – thus parallel absorption paths exist for the photons within this range. This contrasts with the notion of ideal spectral selectivity, whereby a photon definitively generates an electron-hole pair across the largest bandgap less than or equal to the photon's energy.

5.3.2.3 Role of Wavevector, k_{max}

The absorption characteristic of an IB absorbing medium that is yielded by the parabolic-band approximations is intimately related to the value of $k_{\max}$ of the IB absorbing medium. In the first place, $k_{\max}$ is related to the cube root of the concentration [$\#/\mathrm{m}^3$] of quantum states in the IB. This itself is linked to the absorption coefficients via the joint density of states [96]. In the second place, all else being equal save the effective masses of the intermediate band's subbands, the value of $k_{\max}$ may adjust the onsets and offsets of optical absorption [96, 97]).

As an example of the role of $k_{\max}$, the author now describes which of the absorption paths is most likely to convert a photon in the range $(1.40, 1.40 + d\hbar\omega)$ eV into an electron-hole pair. The energy range around 1.4 eV is of particular import as it is the threshold of the non-black emitter (see Figure 27) used to obtain the results present here. Based on the band parameters of the absorbers, which are roughly those given in Table III of reference [96, 97]), when $k_{\max}$ is 1×10^8 m^{-1}, photons near 1.4 eV excite carriers from the VB to the CB. When $k_{\max}$ is 1×10^9 m^{-1}, there are three parallel absorption paths available to these photons; however, they will most likely excite carriers from the IB to the CB. When $k_{\max}$ is 3×10^9 m^{-1}, there are five parallel absorption paths available to these photons; however, these photons will primarily excite carriers from the VB to the IB.

Many of the major results given in this section are given for distinct values of $k_{\max}$ (see Figure 28) or plotted with respect to $k_{\max}$ (see Figure 30). In either case, the author utilizes $k_{\max}$ to identify photoluminescent features that are entirely or largely invariant with respect to $k_{\max}$, and hence invariant with respect to the particularities of the absorption characteristics. In this way, the author identifies features that have high likelihoods of being general photoluminescent properties of an IB absorbing medium as opposed to photoluminescent

properties specific to a particular IB medium. Before offering the major results, the author first outlines the necessary steps to calculate photoluminescent spectra. This is the topic of the following section.

5.3.3 Spectroscopic Procedure

This section details the method used to obtain the photoluminescent spectra. First, the emission spectrum of a light emitting diode is chosen for the incident beam. Second, three (one each to describe the occupancy of the quantum states of each of the three electronic bands) quasi-Fermi levels are adjusted until two conditions are simultaneously obtained: (*i*) the carrier concentrations in the bands yield a charge neutral IB medium [96, 97] and (*ii*) the net rate of electronic charge injected into each band of the IB medium is null. On converging to a solution, the emission spectrum [24] of the IB absorber is used to obtain its photoluminescent spectrum. These steps are now explained in more detail.

5.3.3.1 Incident Beam

The incident spectrum used to illuminate the samples is that emitted by a non-black emitter [24]. In determining the absorptivity of the non-black emitter, a null surface reflectivity is assumed and the absorption coefficients are calculated as for a semi-conductor [172]. Here, the length, temperature, and quasi-Fermi level separation of the non-black emitter are adjusted so that the photon flux [174] emitted is of the order of the solar irradiance at the Earth's surface concentrated 1000 times ($\tilde{1}00$ W/m^2) and so that the full-width at half-maximum (FWHM) is 10 meV (see Figure 27). To generate this large photon flux, the non-black emitter is biased so that population inversion results. Here, the bandgap of the non-black emitter is set to 1.4 eV, which is greater than the largest bandgap of the IB absorbing media under test. It is assumed that the all of the photons emitted from the non-black emitter are incident on the IB samples.

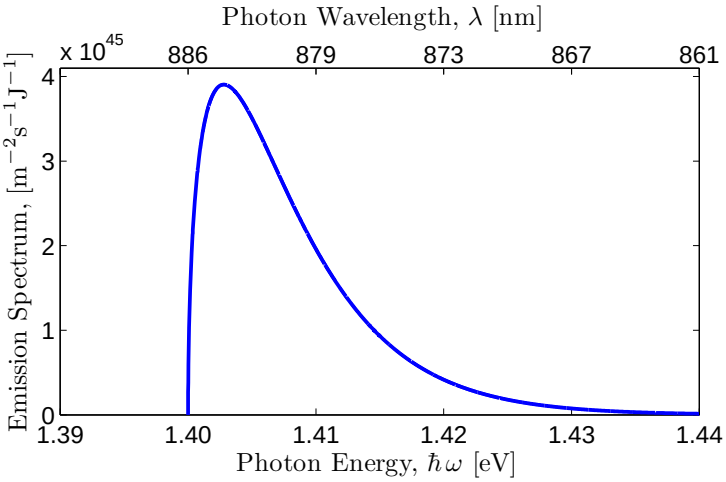

Figure 27: Simulated emission spectrum of the non-black emitter used to irradiate the intermediate band absorbers.

5.3.3.2 Net Charge Current

The net charge current injected into each band is calculated from the radiative flows and as in reference [44]. Here, it is assumed that only those photons emitted from the non-black emitter are incident on the IB samples, that multiplicity [118] does not result from photon absorption, and that the net averaged non-radiative recombination rates are null. In calculating the photon flows pumped into and sunk out of each IB medium [44], the absorption coefficients resulting from the parabolic-band approximation are employed [96, 97]. These absorption coefficients are used to calculate the absorptivity [13] of each IB sample. In so doing, surface reflectivity is assumed to be null.

5.3.3.3 Photoluminescent spectra

On converging to a simultaneous solution of the conditions stated in the introduction of this section, the photoluminescent spectra are obtained. The photoluminescent spectra for photons in the range $(\hbar\omega, \hbar\omega + d\hbar\omega)$ are given as the product of the photon energy, $\hbar\omega$, multiplied by the photon emission spectrum within this range [24]. The author now gives the results of the ongoing investigation.

5.3.4 Invariant Photoluminescent Features

In this section, the author illustrates and discusses two photoluminescent features that are invariant with respect to the value of $k_{\max}$. First, is the number of spectral bands that are present in the PL spectra. Second, is the FWHM of the infrared component of the PL spectra. In obtaining the results present here, the model parameters that are used are nearly those employed in reference [96, 97].

5.3.4.1 Number of Spectral Bands

Figure 28 shows the photoluminescent spectra of three semi-infinite [1] IB absorbing media at 4 K. Each of these three samples have similar band structures; the only difference is that the effective masses of the intermediate band's subbands are adjusted to yield distinct values of $k_{\max}$. Though there are differences in the exact appearances of the PL spectra of each of these three absorbers, the author concentrates attention on contrasting the gross characteristics of these spectra with the PL spectra obtained from previous studies of the luminescent properties of such media [83].

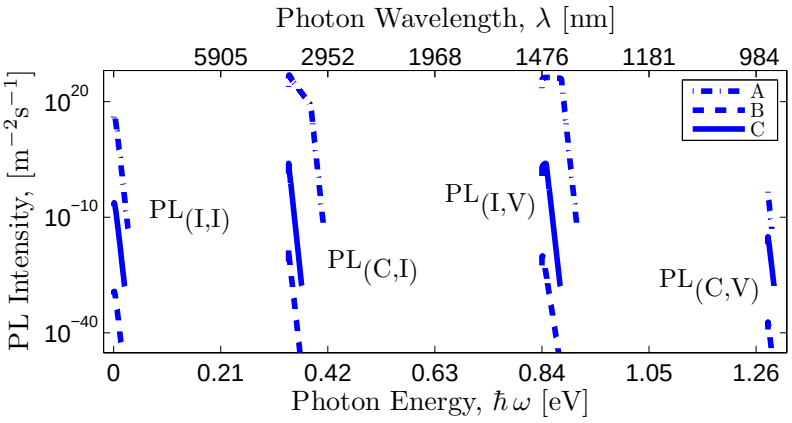

Figure 28: Photoluminescent spectra for three distinct semi-infinite [1] IB absorbing media at 4 K. Each absorber is distinct with respect to the maximum valid wavevector in the intermediate band: (A) $k_{\max}= 1.1 \times 10^8$ m^{-1}, (B) $k_{\max}= 1.2 \times 10^9$ m^{-1} and (C) $k_{\max}= 3 \times 10^9$ m^{-1}. Please note that for visual clarity the magnitudes of plots B and C are scaled by 1×10^{-46} and 1×10^{-23}, respectively.

[1] The absorptivity of a semi-infinite medium will exhibit very sharp transitions (see Figure 29). In addition, a semi-infinite medium will push the computer towards its numerical tolerance. Here, calculations that refer to a semi-infinite media are equivalent to media with a length of 100 gigameters.

Luminescence with Four Spectral Bands The first new characteristic is that each sample yields four, rather than three, spectral bands, within which are contained a significant photoluminescent response. The leftmost spectral bands, $PL_{(I,I)}$, which are absent in references [83], result from momentum-conserving, intraband photo-induced electronic processes between two distinct states in the IB. The remaining three peaks, $PL_{(C,I)}$, $PL_{(I,V)}$, and $PL_{(C,V)}$, result from photo-induced interband electronic processes between the CB and IB, the IB and VB, and the CB and VB, respectively. The onsets of all four spectral bands are identical to the onsets of absorption that are defined in reference [96, 97]. Similarly, the offset of the spectral band associated with the intraband processes is equal to the width of the IB [96, 97].

Photoluminescence at Absorption Onset The second new characteristic is that the apex of each luminescent peak in each spectral band does not, in general, occur at the optical absorption edge. Rather, the apexes occur at slightly larger energies. This results from the fact that under the parabolic-band approximations, the joint density of states at the absorption edges are null. Before moving on to the third major difference, the author stresses that the absorption edges of optical transitions are most fundamentally associated with the minimum energetic difference between any two distinct bands (see Figure 29). This is in contrast to a previous discussion of the absorption edges [10], where there the absorption edges are referenced to the quasi-Fermi level associated with the IB.

Relative Intensity of Luminescence The third new characteristic is that the orders of magnitude of the apexes associated with the interband transitions at intermediate states are several orders of magnitude larger than those associated with the other electronic transitions. This results from the fact that the potential difference between the carriers in the CB and IB, $\varepsilon_{F,CI}$, is near to if not greater than the onset of optical absorption governing those photo-induced electronic transitions. A similar argument may be made regarding the potential difference between the carriers in the IB and VB, $\varepsilon_{F,IV}$. Pane A of Figure 29 illustrates a case where two distinct population inversions exist, which are illustrated by the negative absorptivity for photons in the ranges $(\varepsilon_{CI} \leq \hbar\omega < \varepsilon_{F,CI})$ and $(\varepsilon_{IV} \leq \hbar\omega < \varepsilon_{F,IV})$.

Further, for photons within the range ($\varepsilon_{\mathrm{CI}} \leq \hbar\omega < \varepsilon_{\mathrm{CI}} + \Delta\hbar\omega$), the absorptivity contains a sharp spike. The upshot is that extremely large emission results within these two spectral bands. Contrary to the results of pane A of Figure 29, the author notes that only a single range of negative absorptivity, namely between ($\varepsilon_{\mathrm{CI}} \leq \hbar\omega < \varepsilon_{\mathrm{F,CI}}$), is observed when parallel interband absorption paths exist for photons in the range ($\varepsilon_{\mathrm{IV}} \leq \hbar\omega < \varepsilon_{\mathrm{F,IV}}$) .

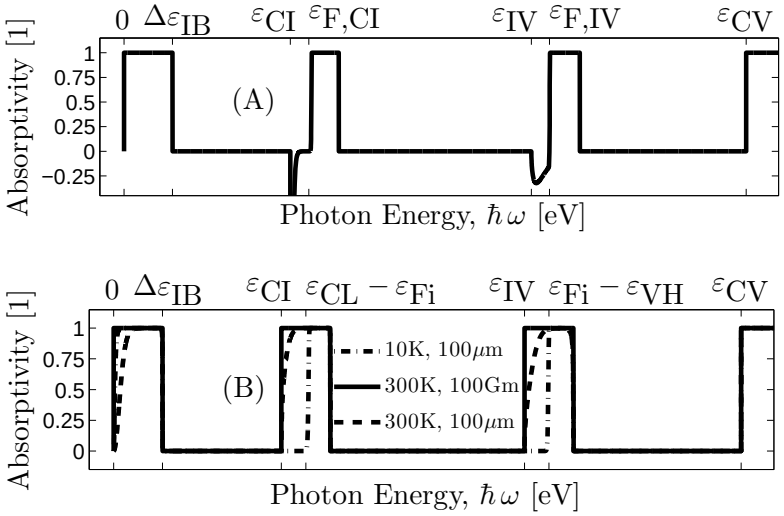

Figure 29: Absorptivity of intermediate band absorbing media with $k_{\max}$ equal to 1.1×10^8 m^{-1}. Pane (A) illustrates the non-equilibrium absorptivity of a semi-infinite medium at 4 K. Pane (B) illustrates the absorptivity of media with distinct lengths each of which is in equilibrium with a blackbody of the temperature listed.

The absorptivity given in pane A of Figure 29 may be compared with the three given in pane B of Figure 29. The absorptivity of each of the latter is obtained when the IB medium is in equilibrium with a blackbody. Note that at temperatures near absolute zero two of the optical edges appear shifted to higher energies. In particular, one edge appears at the energetic difference between the CB edge, $\varepsilon_{\mathrm{CL}}$, and the Fermi energy, $\varepsilon_{\mathrm{Fi}}$; while a second edge appears at the energetic difference between the Fermi energy and the VB edge, $\varepsilon_{\mathrm{VH}}$. Though on close inspection, they are non-zero at the onsets given in Table I of reference [96, 97].

In the following subsection, the author makes observations regarding the FWHM.

5.3.4.2 Full Width at Half Maximum

Figure 30 illustrates the FWHM of the spectral band associated with the photo-induced, electronic transitions between two distinct states of the IB. Shown are nine curves plotted with respect to $k_{\max}$. Each of the curves is associated with an absorber whose temperature and length are distinct from all the others. It is clear that the FWHM increases with increasing temperature. At temperatures near absolute zero, the FWHM range between 1 meV and 4 meV, which are less than the FWHM of the incident beam. Finally, at room temperature the FWHM range between 50 meV and 80 meV, which are less than the widths of the IB considered here (*i.e.* here, as in reference [96, 97], the widths of the IB are uniformly 100 meV). The following section provides concluding remarks.

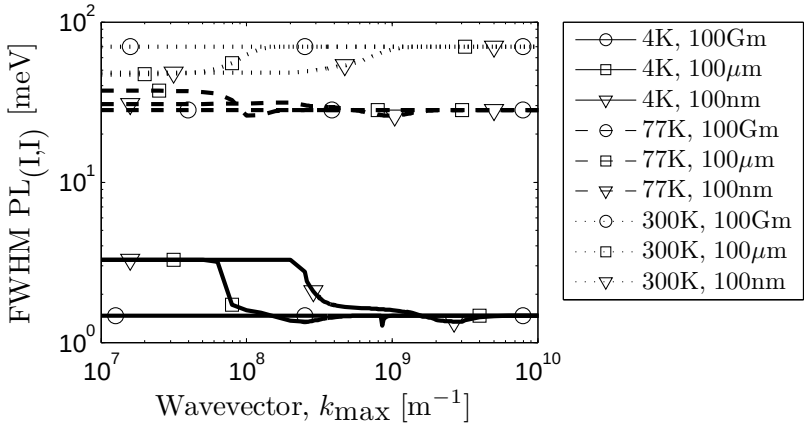

Figure 30: The full width at half maximum (FWHM) of the spectral band associated with intraband electronic transitions between distinct states of the intermediate band (*i.e.* $\mathrm{PL}_{(\mathrm{I,I})}$). Each of the nine plots is associated with an absorber whose temperature and length are distinct from all the others (see legend).

5.3.5 Conclusions

This section illustrates the spectral consequences of intermediate band absorbers under parabolic-band approximations. The results presented here are obtained for absorbers with similar band structures. However, the absorbers are distinct with respect to their temperatures, their lengths, and their absorption characteristics. By directing attention to those results that are largely or completely invariant with respect to the nuances of the absorption

characteristics, the author is able to draw conclusions. The author draws two conclusions regarding the photoluminescent spectra of an absorber with quantum states forming a band of a non-infinitesimal width that is electronically isolated from both the conduction and valence bands and that has a bandwidth smaller than the smallest bandgap in the absorber. First, the resulting PL spectra will have content within four well-separated spectral bands. Second, the full-width at half-maximum of the spectral band in the infrared regime is less than the energetic bandwidth of the quantum states forming the intermediate band. This is important as it allows an empirical measure of the energetic width of the deep quantum states.

5.4 Conclusions

The author begins Chapter 5 by modelling the absorption coefficients of an intermediate-band absorbing medium. Several simplifying assumptions are made, one of which is that the energy-wavevector dispersions are parabolic. The author concludes that an absorbing medium with a multi-bandgap electronic structure may absorb all photons with energies greater than the smallest bandgap in the system and, although, in principle, a criterion for complete absorption without concomitant absorption overlaps exists, achieving this criterion is non-trivial. The author continues Chapter 5 by presenting theoretical photoluminescent spectra of absorbing media. The absorbing media are simplified according to the parabolic-band approximations. The author concludes that photoluminescent intensity of an intermediate band absorber may be appreciable within four distinct and well-separated spectral bands.

CHAPTER VI

REPORT OF INDIUM-ARSENIDE QUANTUM DOTS ENVELOPED IN GALIUM-ARSENIDE-ANTIMONIDE BARRIERS

6.1 Introduction

A nanostructured quantum-dot absorber intended for a three-transition solar cell is reported. Molecular beam epitaxy is employed to fabricate InAs quantum dots completely enveloped in a barrier of $GaAs_{1-x}Sb_x$ ($x \approx 0.12$) matrix grown on a GaAs substrate. The absorber design is presented and the grown structures are characterized by transmission-electron microscopy, atomic-force microscopy, photoreflectent spectroscopy, and time-integrated and time-resolved photoluminescent spectroscopy. The author inferrs that the conduction-band discontinuity of the quantum dot heterojunctions is roughly 250-300 meV; and that the quantum-dot heterojunctions are either type-II heterojunctions or near to the transition between type-I heterojunctions and type-II heterojunctions. The author concludes that detecting photons within the infrared regime of the electromagnetic spectrum is necessary to confirm that the InAs/$GaAs_{1-x}Sb_x$ ($x \approx 0.12$) absorber is, in fact, a three-transition absorber.

The outline for the remainder of this chapter is as follows. In Section 6.2, the author presents detailed background information. In section 6.3, the author describes the InAs/$GaAs_{1-x}Sb_x$ ($x \approx 0.12$) quantum-dot absorber. In section 6.4, the author disscusses the various experiments that are performed on the the InAs/$GaAs_{1-x}Sb_x$ ($x \approx 0.12$) quantum-dot absorber as well as a control absorber. In section 6.5, the author discusses the experimental results in relation to the theory of the three-transition absorber. In section 6.6, the author offers concluding remarks.

6.2 Background

The abstract notion of increasing the efficiency of photovoltaic solar energy conversion with a three-transition solar cell is well-established [20, 35]. In addition to offering a global efficiency enhancement while operating on its own, when comparing layers within tandem stacks, a layer comprised of a three-transition solar cell is theorized to offer a greater efficiency enhancement than a layer comprised of a standard p-n junction solar cell [175]. At the time that this disseration is published, an experimental demonstration of a global-efficiency enhancement is absent from the literature. The primary impediment in realizing a three-transition solar cell is the fabrication of an appropriate three-transition absorber.

The use of quantum-dot technology is offered as a means to realize a three-transition solar cell [59, 60, 61]. Previous work on three-transition solar cells implemented with quantum-dot technology (*i.e.*, a quantum-dot intermediate-band solar cell (IBSC)) revolves around the InAs/GaAs (confined/barrier) [41, 62, 63, 64] and InGaAs/GaAs [65] material systems. They are both grown on GaAs substrates. One characteristic limiting the usage of these material systems is that they are type-I heterojunctions. This enables the luminescent spectra of these prototype QD IBSC samples [41, 62] to illustrate narrowly separated and overlapping peaks, rather than the luminescent signature [83] (*i.e.*, luminescence in three [83] (or four [98]) well-separated spectral bands) of a three-transition material [66].

The author reports on the InAs/$GaAs_{1-x}Sb_x$ ($x \approx 0.12$) material system, which is identified as a material system for prototype three-transition solar cells [66]. The author emphasizes two beneficial properties of this material system. First, it is theoretically calculated [66] and experimentally inferred [151, 152] to yield heterojunctions at the transition between type-I and type-II heterojunctions. Second, antimonide acts as a surfactant [153, 154]. The former (band alignment), is advantageous because it abates the difficulty in interpreting data from inter-band, optical experimental methods that exists if both holes and electrons are involved [130]. The latter (surfactant) is advantageous, because it inhibits the generation of interfacial defects and thus leads to superior optical activity [155]. In the next section, the author describes the intended structure of the InAs/GaAsSb absorber.

6.3 Description of the Absorber

In this section, section 6.3, the author depicts (section 6.3.1) and predicts (section 6.3.2) the intended electronic structure of the absorber.

6.3.1 Depiction of the Absorber

A cross section of the intended structure of the absorber is depicted in Figure 31. There are five distinct regions that comprise the absorber: a GaAs layer (includes both the GaAs substrate and a GaAs buffer), a $GaAs_{0.88}Sb_{0.12}$ barrier layer, an InAs quantum dot layer, a second $GaAs_{0.88}Sb_{0.12}$ barrier layer, and a GaAs capping layer. The thicknesses of these layers are labeled as $t_{\mathrm{s,l}}$, $t_{\mathrm{b,l}}$, t_{c}, $t_{\mathrm{b,r}}$, and $t_{\mathrm{s,r}}$, respectively. The thickness of each layer is intended to be thin to minimize the formation and propagation of dislocations. The thickness of the deposited InAs layer is intended to be just large enough to produce a Stranski-Krastanov morphological change from a two-dimensional epitaxial-layer to a three-dimensional layer of quantum dots. The band gaps of the GaAs layer and GaAsSb layers are labeled as $\varepsilon_{\mathrm{CV,s}}$ and $\varepsilon_{\mathrm{CV,b}}$, respectively. The conduction-band discontinuity and valence-band discontinuity at the interface between the GaAs and GaAsSb layers are labeled as $\varepsilon_{\Delta\mathrm{CB,s\text{-}b}}$ and $\varepsilon_{\Delta\mathrm{VB,s\text{-}b}}$, respectively. The conduction-band discontinuity at the interface between the GaAsSb and InAs layers is labeled as $\varepsilon_{\Delta\mathrm{CB,b\text{-}c}}$. The valence-band discontinuity at this interface is intended to be negligible.

A collection of bound electronic states will be present in the potential well defined by the conduction-band discontinuity $\varepsilon_{\Delta\mathrm{CB,b\text{-}c}}$. The minimum energetic separation between the collection of bound states and the valence-band continuum is labeled as $\varepsilon_{\mathrm{I,V}}$, where $\varepsilon_{\mathrm{I,V}} \leq \varepsilon_{\mathrm{CV,b}} - \varepsilon_{\Delta\mathrm{CB,b\text{-}c}}$. The minimum energetic separation between the collection of bound states and the conduction-band continuum is labeled as $\varepsilon_{\mathrm{CI}}$, where $0 \leq \varepsilon_{\mathrm{CI}} \leq \varepsilon_{\Delta\mathrm{CB,b\text{-}c}}$. The difference between the energy of the bound state with the largest energy and the bound state with smallest energy is labeled as $\varepsilon_{\Delta\mathrm{IB}}$, where $0 \leq \varepsilon_{\Delta\mathrm{IB}} \leq \varepsilon_{\Delta\mathrm{CB,b\text{-}c}}$.

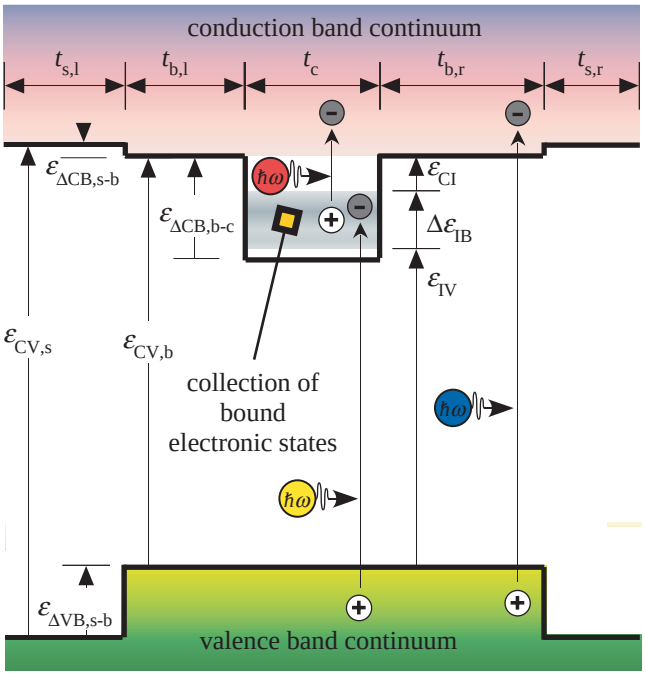

Figure 31: Schematic band structure for the InAs/$GaAs_{0.88}Sb_{0.12}$/GaAs quantum dot absorber.

6.3.2 Prediction of Electronic Structure

Based on the band parameters of the technologically important III-V semiconductors and their ternary alloys [146], the author calculates the bandgaps $\varepsilon_{CV,s}$ and $\varepsilon_{CV,b}$ as 1.4 eV and 1.2 eV, respectively; and the discontinuities $\varepsilon_{\Delta CB,s\text{-}b}$, $\varepsilon_{\Delta VB,s\text{-}b}$, and $\varepsilon_{\Delta CB,b\text{-}c}$ as 30 meV, 210 meV, and 830 meV, respectively. The calculations of the above values include the temperature-related Varshni coefficients but exclude the strain-related elastic coefficients. The inclusion of the strain-related coefficients significantly reduces the value of $\varepsilon_{\Delta CB,b\text{-}c}$, so that it may be of order 400 meV [176].

The locations of the bound electronic states that are predicted from the band parameters of the technologically important III-V semiconductors and their ternary alloys roughly conforms to the locations of the bound states derived from an atomistic pseudopotential method [177]. The application of an atomistic pseudopotential method to a prototypical InAs/GaAs system predicts that the ground energy of the bound level is 300 meV less than the lower edge of the conduction-band continuum [177].

6.4 Experimentation with the Absorber

Two absorbers are grown on GaAs(0 0 1) epi-ready substrates by molecular-beam epitaxy. One is a quantum-dot absorber and the other is a control that has a structure similar to that depicted in Figure 31, except that the layer of InAs quantum dots is excluded. X-ray diffractometry is used to characterize the layer compositions and layer thicknesses of both absorbers (section 6.4.1). Both transmission-electron microscopy and atomic-force microscopy are used to characterize the morphological structure of the quantum dot absorber (section 6.4.2). Photoreflectent spectroscopy is used to characterize changes in the optical constants of both absorbers (section 6.4.3). Photoreluminescent spectroscopy is used to characterize the photo-emission of both absorbers (section 6.4.4).

6.4.1 X-Ray Diffractometry

X-ray diffractometry is used to characterize the layer compositions and layer thicknesses by fitting double-crystal and triple-crystal rocking curves (both ω and $\omega/2\theta$ rocking curves). The fitting of the rocking curves associated with the quantum-dot absorber implies that the thickness of the GaAs buffer layer is 390 nm, the thickness of first $GaAs_{1-x}Sb_x$ layer is 19 nm, the thickness of the InAs layer is 0.3 nm, the thickness of second $GaAs_{1-x}Sb_x$ layer is 17 nm, the thickness of the GaAs capping layer is 45 nm, and the molar concentration of antimonide, x, in the first and second GaAsSb layer is 0.14 and 0.11, respectively. The fitting of the rocking curves associated with the control absorber implies that the thickness of the GaAs buffer layer is 380 nm, the thickness of the single $GaAs_{1-x}Sb_x$ layer is 34 nm, the thickness of the GaAs capping layer is 94 nm, and the molar concentration of antimonide, x, is 0.12.

6.4.2 Transmission-Electron Microscopy and Atomic-Force Microscopy

Both transmission-electron microscopy and atomic-force microscopy are used to characterize the morphological structure of the quantum dots. Images obtained from contact-mode atomic-force microscopy performed in both height mode and deflection mode suggest that the quantum dots form into elongated lenses. The typical length along the major axis is of

order 40 nm. The typical length along the minor axis is of order 20 nm. Images obtained from transmission-electron microscopy suggest that the typical diameter of a quantum dot is of order 20 nm and that the typical height of a quantum dot is of order 4 nm. In the following section, the author describes the characterization of the absorbers by photoreflectent spectroscopy.

6.4.3 Photoreflectent Spectroscopy

In this section, section 6.4.3, the author describes the apparatus used to acquire the photoreflectent spectra, and presents a time-integrated photoreflectent spectrum of the control absorber and the quantum-dot absorber.

6.4.3.1 Description of the Apparatus

Time-integrated photoreflectent measurements are conducted with two beams of light. The pump beam is a He-Ne laser that operates at 17 mW and emits photons with a wavelength of 632 nm (1.96 eV) within a spot size of 1 mm^2. The probe beam is a 250 W quartz-tungsten halogen lamp that operates at 125 W and is suitable for measuring within the visible and near-infrared regimes of the electromagnetic spectrum. The probe beam is first passed through a monochrometer and next, passed through a lens to enhance the power density within a spot size of 1 mm^2, which matches that of the laser. The photoreflectance is modulated by chopping the laser beam at 790 Hz. The signal at the photodetector is integrated over a period of one second. A Ge detector operating at room temperature is used to detect photons with wavelengths between 800 nm (1.55 eV) and 1600 nm (0.78 eV).

6.4.3.2 Presentation of the Time-Integrated Photoreflectance

The photoreflectent spectrum of the control absorber and the photoreflectent spectrum of the quantum-dot absorber are presented in Figure 32. The photoreflectent spectrum of the control absorber implies that its optical constant changes starting at 1.2 eV and again at 1.37 eV. The change at 1.2 eV results from the GaAsSb matrix and the change at 1.37 eV results from the GaAs matrix. The photoreflectent spectrum of the quantum-dot absorber is qualitatively similar to that of the control absorber. The author emphasizes that, similar

to the photoreflectent spectrum of the control absorber, the photoreflectent spectrum of the quantum-dot absorber is unchanging between 0.78 eV and 1.2 eV. In the following section, the author describes the characterization of the absorbers by photoluminescent spectroscopy.

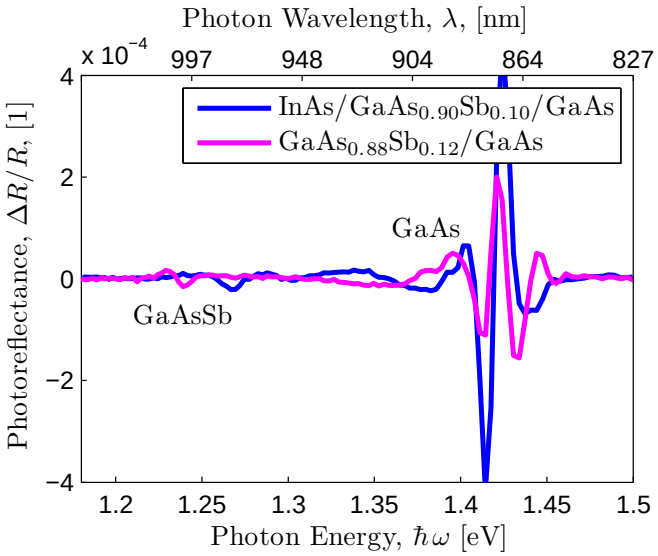

Figure 32: Time-integrated photoreflectent spectra of the quantum-dot absorber and the control absorber. Though probed, no change in optical constant is discernable in either absorber between the energies 0.78 eV and 1.2 eV.

6.4.4 Photoluminescent Spectroscopy

In this section, section 6.4.4, the author describes the apparatus used to acquire the photoluminescent spectra, presents a time-integrated photoluminescent spectrum of the control absorber and of the quantum-dot absorber, and discusses time-resolved photoluminescent data of the control absorber and the quantum-dot absorber.

6.4.4.1 Description of the Apparatus

The photoluminescent apparatus is described in reference [178]. Time-integrated photoluminescent (PL) and time-resolved photoluminescent (TRPL) measurements are conducted with the sample mounted in a He-flow cryostat operating from 4.4 to 300 K. The excitation source was a tunable Ti:sapphire laser with operating wavelength fixed at 750 nm (1.65 eV), which delivers 130 fs long pulses with a power density of 1.36 W/cm^2 and with a

repetition rate of 76 MHz. The luminescence is dispersed into a 0.32 m spectrometer and is detected by a liquid nitrogen cooled InGaAs detector or by a C4334 streak camera for PL and TRPL, respectively. The InGaAs detector is used to detect photons with wavelengths between 700 nm (1.77 eV) and 1600 nm (0.78 eV). The time resolution of the setup is less than 80 ps. The author now offers the time-integrated photoluminescent spectra.

6.4.4.2 Presentation of the Time-Integrated Photoluminescence

Figure 33 presents time-integrated photoluminescent spectra of the control absorber and the quantum-dot absorber, where each spectrum is normalized with respect to its peak intensity.

The spectrum of the control absorber (dashed line of Figure 33), which is obtained while the absorber is maintained at 4 K, indicates strong luminescence within two spectral bands. These spectral bands are labeled $PL_{CT,I}$ and $PL_{CT,II}$. In spectral band $PL_{CT,I}$, photoluminescence is apparent for photons with energy $\hbar\omega$ in the range (1.19 eV (1040 nm) $\leq$ $\hbar\omega$ $\leq$ 1.35 eV (919 nm)), with a peak occurring at 1.32 eV (939 nm). In spectral band $PL_{CT,II}$, photoluminescence is apparent for photons with energy $\hbar\omega$ in the range (1.36 eV (912 nm) $\leq$ $\hbar\omega$ $\leq$ 1.52 eV (816 nm)), with a peak occurring at 1.47 eV (844 nm). The spectrum of the quantum dot absorber (solid line of Figure 33), which is obtained while the absorber is maintained at 77 K, indicates strong luminescence within two spectral bands. These spectral bands are labeled $PL_{QD,I}$ and $PL_{QD,II}$. In spectral band $PL_{QD,I}$, photoluminescence is apparent for photons with energy $\hbar\omega$ in the range (1.03 eV (1240 nm) $\leq$ $\hbar\omega$ $\leq$ 1.22 eV (1020 nm)), with a peak occurring at 1.14 eV (1090 nm). In spectral band $PL_{QD,II}$, photoluminescence is apparent for photons with energy $\hbar\omega$ in the range (1.29 eV (960 nm) $\leq$ $\hbar\omega$ $\leq$ 1.40 eV (886 nm)), with a peak occurring at 1.35 eV (919 nm). In Figure 33, the author emphasizes that the spectral band $PL_{QD,I}$ may be characterized by its full widths. The full-width at half-maximum, FW_a, the full-width at tenth-maximum, FW_b, and the full-width at hundredth-maximum, FW_c, are 55 meV, 120 meV, and 160 meV, respectively.

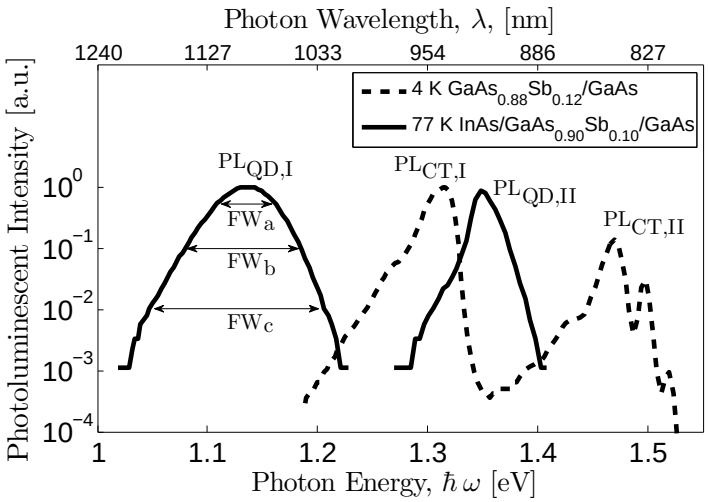

Figure 33: Time-integrated photoluminescent spectra of the quantum-dot absober (solid) and the control absorber (dashed). Each spectrum is normalized with respect to its peak intensity. Though probed, no photons with energies between 0.78 eV to 1.03 eV are detected from sample B.

The photoluminescent response of the control absorber within the spectral bands labeled $PL_{CT,I}$ and $PL_{CT,II}$ results from its $GaAs_{0.90}Sb_{0.10}$ matrix and its GaAs matrix, respectively. The photoluminescent response of the quantum dot absorber within the spectral band labeled $PL_{QD,II}$ is highly correlated with the photoluminescent response of the control absorber within the spectral band labeled $PL_{CT,I}$. Therefore, photoluminescence of the quantum dot absorber within the spectral band labeled $PL_{QD,II}$ may be attributed to the $GaAs_{0.88}Sb_{0.12}$ barrier layer. The presents author now discusses the time-integrated photoluminescent spectra.

6.4.4.3 Discussion of the Time-Resolved Photoluminescence

Time-resolved photoluminescent spectroscopy is performed on the control absorber and the quantum-dot absorber while they are maintained at 77 K. For the control absorber, the tunable laser is set to 944 nm (1.31 eV), which corresponds to the peak of the spectral band labeled $PL_{CT,I}$ (see Figure 33). The fit to the time-resolved data indicates a lifetime of 3.8 ns at this wavelength. For the quantum dot absorber, two time-resolved measurements are made. First, the tunable laser is set to 920 nm (1.35 eV), which corresponds to the peak of the spectral band labeled $PL_{QD,II}$ (see Figure 33). Second, the tunable laser is set

to 1091 nm (1.14 eV), which corresponds to the peak of the spectral band labeled $PL_{QD,I}$ (see Figure 33). The fit to the time-resolved data indicates a lifetime of 10 ns and 1.4 ns at these wavelengths, respectively.

The author now offers a discussion of the theoretical and experimental components presented thus far.

6.5 Discussion of the Results

In Section 6.5 the author discusses the experimental results within the context of the three-transition solar cell. Specifically, in Section 6.5.1, the author infers the electronic structure of the quantum-dot absorber from experimental results and in Section 6.5.2, the author discusses the failure to match the experimental photoluminescent spectrum of the quantum-dot absorber with the photoluminescent signature of a three-transition absorber. In Section 6.5.3, the author discusses why a photoreflectent signal associated with the bound states of the quantum-dot heterojunctions is not apparent.

6.5.1 Inference Regarding Absorber's Electronic Structure

The author draws three inferences regarding the absorber's electronic structure. The author infers that the InAs/$GaAs_{1-x}Sb_x$ ($x \approx 0.12$) heterojunctions exists at or near a type-I to type-II heterojunctions. The author infers that the bandgap of the $GaAs_{1-x}Sb_x$ ($x \approx 0.12$) is roughly 1.22 eV and 1.19 eV at room temperature and at 4 K, respectively. The author infers that the conduction band discontinuity in the InAs/$GaAs_{1-x}Sb_x$ heterojunctions is roughly 200 eV-300 meV.

The author infers that the band alignment of the InAs/$GaAs_{1-x}Sb_x$ heterojunctions within the quantum-dot absorber exist at or near the transition between a type-I heterojunctions and a type-II heterojunctions. Type-II heterojunctions are theoretically predicted [143] and experimentally verified [144] as having relatively long radiative lifetimes resulting from the spatial division of confined electrons and holes. A very long lifetime (10 ns) is extrapolated from the time-resolved photoluminescent data that is taken at a wavelength associated with the peak of the photoluminescent spectrum within the spectral band labeled $PL_{CT,I}$ in Figure 33. This lifetime is one order of magnitude greater than the

lifetimes associated with the bound states in type-I InAs/GaAs heterojunctions, which are typically of the order 1 ns when the InAs/GaAs absorber is maintained at temperatures between 10 K and 85 K [179].

The author infers that the bandgap of the $GaAs_{1-x}Sb_x$ ($x \approx 0.12$) matrix, $\varepsilon_{CV,b}$, is roughly 1.22 eV +/- 0.01 eV at room temperature and 1.19 eV+/- 0.02 eV at 4 K. The former inference is drawn from the photoreflectent spectrum that shows a change in the photoreflectance beginning roughly at 1.22 eV. The latter inference is drawn from the time-integrated photoluminescent data within the spectral band labeled $PL_{CT,I}$ (see Figure 33), which has an emission onset at 1.19 eV.

The author infers that the conduction-band discontinuity at the interface between the GaAsSb matrix and InAs matrix, $\varepsilon_{\Delta CB,b\text{-}c}$, is between 210 meV and 320 meV. This inference is drawn from the time-integrated photoluminescent spectrum of the quantum dot absorber. The smaller of the two values corresponds to the energetic difference between the peak of spectral band $PL_{QD,II}$, and the peak of spectral band $PL_{QD,I}$, which is 210 eV. The larger of the two values corresponds to the energetic difference between the peak of spectral band $PL_{QD,II}$, and the onset of spectral band $PL_{QD,I}$, which is 320 eV.

The author now discusses the photoluminescent spectrum of the quantum-dot absorber in relation to the photoluminescent signature of a three-transition absorber.

6.5.2 Non-apparence of Photoluminescent Signature

The author now discusses the failure to observe the photoluminescent signature of a three-transition solar cell within the photoluminescent spectrum of the $InAs/GaAs_{1-x}Sb_x$ ($x \approx 0.12$) quantum-dot absorber. The photoluminescent spectrum of the quantum-dot absorber, which is illustrated in Figure 33, shows significant photoluminescent intensity within two well-separated spectral bands. This, as opposed to the photoluminescent signature of the three-transition absorber that is theorized to have significant intensity within three [41, 83] or four [98] well-separated spectral bands. The author infers where these non-apparent photoluminescent features would be visible, were they to exist. The author discusses the need for infrared detection, to determine whether or not they are visible.

Photoluminescent features will result from radiatively-coupled transitions between any two states in the collection of bound states (hereafter referred to as "(I,I) transitions"). The onset of the photoluminescent features associated with the (I,I) transitions should be apparent, beginning just above 0 meV. The offset of the photoluminescent features associated with the (I,I) transitions should be apparent at an energy less than or equal to $\varepsilon_{\Delta\mathrm{IB}}$ (see Figure 31) [98]. Based on the inferred electronic structure, the offset of the photoluminescent features associated with (I,I) transitions should be detected from photons with energy $\hbar\omega$ where 0 meV $< \hbar\omega \leq$ 320 meV (3.9 μm). If the energetic extent of the collection of bound states is infinitesimally small, then the offset should occur at 0 meV. If the energetic extent of the collection of bound states is equal to the potential depth of the InAs/GaAs$_{0.88}$Sb$_{0.12}$, $\varepsilon_{\Delta\mathrm{CB,b\text{-}c}}$, then the onset should occur nearer to 320 meV. The higher the temperature at which the absorber is maintained, the nearer the offset will be to $\varepsilon_{\Delta\mathrm{IB}}$ [98].

The author emphasizes that if the photoluminescent features resulting from the (C,I) transitions and the (I,I) transitions of the InAs/GaAs$_{1-x}$Sb$_x$ ($x \approx 0.12$) absorber were to be viewable, then they would likely appear within one spectral band. The shallowness of the conduction-band discontinuity and the broadness of the spectrum of the electronic levels [177] justify this. Furthermore, the photoluminescent features associated with the (C,I) transitions might or might not be distinguishable from the photoluminescent features associated with the (I,I) transitions [180].

The failure to detect photoluminescence within the remaining one or two spectral bands may be attributed to the absence of infrared photodetection in the experimental apparatus (see section 6.4.4.1). In addition, because of the failure to detect photons within the infrared regime of the electromagnetic spectrum, it is impossible to irrefutably assert that the InAs/GaAs$_{1-x}$Sb$_x$ ($x \approx 0.12$) quantum-dot absorber is, in fact, a three-transition absorber.

In the next subsection, the author now discusses the absence of a photoreflectent signal associated with the bound states of the quantum-dot absorber.

6.5.3 Non-appearance of Photoreflectent Signal

In this subsection, the author discusses the failure to observe a photoreflectent signal associated with the collection of bound electronic states. The author presents four possible reasons for this non-apparent photoreflectent signal and next evaluates each of the reasons.

A correspondence between the time-integrated photoluminescent spectra and time-integrated photoreflectent spectra of an absorber is generally expected. Both an appreciable photoluminescent intensity and an appreciable change in the photoreflectance are apparent within the domain from 1 eV to 1.2 eV in InAs/GaAs quantum-dot heterojunctions [181, 182, 183, 184, 185]. The features within this domain, similar to the features of the InAs/GaAsSb of Figure 32, are attributed to electronic transitions at bound states introduced by the quantum-dot heterojunctions [181, 182, 183, 184, 185]. However, in some instances the correspondence between time-resolved photoluminescent spectra and time-resolved photoreflectent spectra of an absorber are not apparent. An appreciable photoluminescence is apparent and an appreciable change in the photoreflectance is not apparent within the domain from 1 eV to 1.2 eV in InAs/GaAs quantum-dot heterojunctions [186, 183, 185].

There are four potential reasons as to why a photoreflectent signal would not appear within this domain. First, if the modulated pump beam is comprised of photons with energies below the bandgap of the barrier material, then a photoreflectent signal may not appear [183]. Second, if the total volume of the quantum dots is small and the size distribution of the quantum dots is largely inhomogeneous, then a photoreflectent signal may not appear [185]. Third, if the oscillator strength is reduced because of the transition from a type-I heterojunctions, then a photoreflectent signal may not appear [187]. Fourth, if the signal-to-noise ratio is low, then a photoreflectent signal may not appear.

The first reason is not plausible in explaining the experimental results because the pump beam is comprised of photons with energies larger than both the GaAsSb matrix and GaAs matrix. The second reason is plausible in explaining the results because the quantum-dot absorber presented here is composed of a single quantum-dot layer with a qualitatively large inhomogeneity in the size of the quantum dots –this is indicated by atomic-force microscopic images, which are not illustrated. The third reason is plausible in

explaining the results because the quantum-dot absorber presented here is not composed of quantum-dot heterojunctions with a type-I band alignment. The fourth reason is plausible in explaining the results because, when the signal appears within this domain, the amplitude of the photoreflectent signal may be of the order 1×10^{-5} or less [181, 183]. The signal-to-noise ratio in the photoreflectance apparatus employed by the author is too large to discern a signal with an amplitude that is of the order 1×10^{-5} (see Figure 32 on page 115).

The author now offers concluding remarks.

6.6 Conclusions

Experimentation on the InAs/$GaAs_{1-x}Sb_x$ ($x \approx 0.12$) quantum-dot absorber offers significant insight regarding the research and development of a three-transition solar cell. The band alignment of the InAs/$GaAs_{1-x}Sb_x$ ($x \approx 0.12$) heterojunctions occurs at the transition between a type-I and type-II heterojunctions, which abates the difficulty in interpreting empirical data from inter-band, optical experimental methods. The plausibility that the InAs/$GaAs_{1-x}Sb_x$ ($x \approx 0.12$) quantum-dot absorber is, in fact, a three-transition absorber remains an open question. This remains so because the author does not detect photoreflectance nor photoluminescence associated with each of the three distinct photo-induced interband electronic transitions of a three-transition absorber. The author detects one change in the photoreflectent signal and detects photoluminescent intensity within two well-separated spectral bands. All of these are detected within the visible regime of the electromagnetic spectrum. The author infers that one of the three distinct photo-induced interband electronic transitions of the InAs/$GaAs_{1-x}Sb_x$ ($x \approx 0.12$) is only viewable in the infrared regime of the electromagnetic spectrum. The author concludes that when using optical experimental methods, detecting photons within the infrared regime of the electromagnetic spectrum is necessary to confirm that the InAs/$GaAs_{1-x}Sb_x$ ($x \approx 0.12$) absorber is, in fact, a three-transition absorber and, more generally, that any absorber is a three-transition absorber that is appropriate for a three-transition solar cell. The general conclusion is derived from the fact that the domain of high solar irradiance is roughly centered around 800 meV (1.55 μm) and the related fact that the optimal band structure

of a three-transition solar cell's absorber has a bandgap at roughly 700 meV (1.77 μm). Therefore, as long as researchers intend to realize three-transition absorbers appropriate for three-transition solar cells, researchers must include infrared photodetection in their optical experimental apparati.

APPENDIX A

RAPID AND PRECISE CALCULATION OF FLUX

A.1 Appendix Introduction

The central problem addressed in this appendix is the rapid and precise calculation of the energy and particle flux for detailed-balance photovoltaic applications. The calculation of energy and particle flux is essential to modeling the efficiencies and efficiency limits of solar energy conversion devices. Computing flux with the canonical Bose-Einstein integral, which has no closed-form solution, is time consuming and, without due care, prone to error. The novel numerical approach presented here transforms the Bose-Einstein integral into a linear combination of incomplete Riemann zeta integrals. The numerical method is benchmarked by comparisons with the Riemann zeta functions. The rapidity of the numerical package is gauged by comparing the duration of flux calculations to other calculation methods.

The organization of this appendix is as follows: the next section presents the details of this method, the third section shows the means by which the precision of the method has been verified, the fourth section presents evidence that this method is highly precise, and the fifth section presents evidence that this method, in most cases, is faster than other methods.

A.2 Calculation of flux

To calculate flux rapidly and precisely an integral is sought such that its integrand is a function of a single dummy variable and its limits of integration allow it to be a proper definite integral. In order to avoid accruing numerical error, the limitations of the computer arithmetic must be considered with respect to the integrands. In regions where there is large floating-point error, appropriate limiting functions must be employed to approximate the integrands. Finally, consideration must be given to the generation of the LUT.

A.2.1 Form suitable for numerical computations

The integral describing photon flux, F_P, derives from the emissivity of the matter that the photons are interacting with, the density of photon modes, and the Bose-Einstein statistics. The canonical form of the flux is given as

$$F_P(E_A, E_B, T, \mu) = \begin{cases} \frac{2\,\pi}{c^2\,h^3} \int_{E_A}^{E_B} \frac{E^P\,dE}{\exp\left(\frac{E-\mu}{k\,T}\right)-1} & \text{if } \mu < E_A < E_B,\ 0 < E_A < E_B, \text{ and} \\ 0 & \text{otherwise.} \end{cases} \tag{26}$$

where E_B and E_A are the upper and lower energy limits of the photon emission from the solid, respectively, μ is the equilibrium chemical potential of the radiation, T is the surface temperature of the matter, c is the speed of light, h is Planck's constant, k is Boltzmann's constant, and P takes the values 2 or 3 for the calculation of particle flux or energy flux, respectively [174]. In future expressions for flux, it is understood that the inequalities given in Equation (26) are satisfied so that that the flux is non-zero.

The first step in creating look-up-tables, which expedite the rapidity and precision of flux calculations, is to transform Equation (26) into a form whose integrands are functions of unitless, dummy variables. By the following substitution, $y = (E-\mu)/k\,T$, Equation (26) is rewritten as a linear combination of IRZI

$$F_P(E_A, E_B, T, \mu) = \sum_{p=1}^{P+1} a_{p-1} \int_{\frac{E_A-\mu}{k\,T}}^{\frac{E_B-\mu}{k\,T}} \frac{y^{p-1}\,dy}{\exp(y)-1}, \tag{27}$$

where a_{p-1} may be determined from carrying through the algebra. Though the integrands of Equation (27) are a function of a unitless dummy variable, the form of Equation (27) is not always suitable. Such is the case when the upper limit of the emissivity tends toward infinity, which is the case in the majority of detailed-balance efficiency calculations. In such circumstances, the forms given by Equation (26) and Equation (27) become improper integrals. Thus, the numerical integration tends to become arbitrary, as the following question must be answered: Just how large is infinity? According to some some authors [10], it is 6 eV. To surmount this problem, the substitution $x = 1/y$ is employed and thus flux is re-written as

$$F_P(E_A, E_B, T, \mu) = \sum_{p=1}^{P+1} a_{p-1} \int_{\frac{k\,T}{E_B-\mu}}^{\frac{k\,T}{E_A-\mu}} \frac{dx}{x^{p+1}\left[\exp\left(\frac{1}{x}\right)-1\right]}. \tag{28}$$

The form of Equation (28) is superior to the two previous forms because it allows for the construction of LUT and avoids the difficulty of evaluating improper integrals. An additional benefit of Equation (27) and Equation (28) is that the individual integrals (for p a positive integer greater than one) may be compared with closed-form expressions of the Riemann zeta functions, thus allowing checks on the precision of the method.

A.2.2 Limitations of computer arithmetic

Computer arithmetic further complicates the precise computation of flux. When x is small, one must guard against underflow errors when evaluating the Riemann zeta integrands. For comparison, when E of Equation (26) is large, one must guard against both underflow and round-off errors. Further, when x is large, the floating-point error caused by the subtraction in the denominator causes the integrands to oscillate with x, until finally one-over-zero errors occur. This may be seen clearly by plotting the relative error between the integrands and a limiting approximation to the integrands. Figure 34 illustrates for the case $p = 3$ that the Riemann integrand of Equation (28) begins to oscillate with x, but that the integrand may be approximated by a limiting expression given in Equation (30). For comparison, when μ nears E_A, the same phenomenon is observed for the Bose-Einstein integrands. As shown in Figure 35, when x increases a bit beyond 1×10^7, the relative error between the two integrands stops decreasing and begins to oscillate with larger and larger amplitude. Thus, for all the Riemann integrals, there is a fixed domain of x, $\mathcal{D}_x$, such that the integrands are both computable and stable. The limits of this domain largely depend upon the machine precision of the microprocessor, yet some judgment is necessary as to the location of the upper cutoff of the domain. It is found [122] that for a machine precision of order 1×10^{-16}, $\mathcal{D}_x = \left[1.41 \times 10^3, 1.00 \times 10^7\right]$ is suitable for all the orders of the IRZI that are of interest ($p = 1, 2, 3, 4$). The limits of this numerical domain derive purely from the constraints of the computer arithmetic, as opposed to considerations regarding the spectrum of a given radiation of interest.

In those cases where there is a contribution to the flux from outside the boundaries of $\mathcal{D}_x$, limiting expressions must be used to calculate that contribution. The author recommends

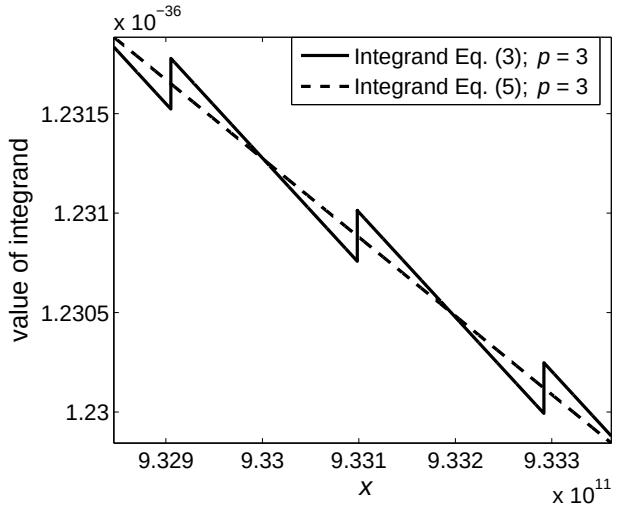

Figure 34: For large x, evaluation of Riemann zeta integrands is subject to round-off errors that are caused by the denominator terms. In these cases, the integrands may be approximated by limiting functions such as those given in Equation (30). This figure shows the integrand of Equation (27), $\left(x^{p+1}\left[\exp\left(1/x\right)-1\right]\right)^{-1}$, and that of Equation (30), x^{-p}, for the case $p=3$

the use of $\hat{F}_P^{\text{low}}$ and $\hat{F}_P^{\text{high}}$ to calculate that contribution if $kT/(E_B-\mu) < \min(\mathcal{D}_x)$ and if $kT/(E_A-\mu) > \max(\mathcal{D}_x)$ respectively, where

$$\hat{F}_P^{\text{low}}(E_A,E_B,T,\mu) = \sum_{p=1}^{P+1} a_{p-1} \int_{\frac{kT}{E_B-\mu}}^{\min(\mathcal{D}_x)} \frac{dx}{x^{p+1}\exp\left(\frac{1}{x}\right)}. \tag{29}$$

$$\hat{F}_P^{\text{high}}(E_A,E_B,T,\mu) = \sum_{p=1}^{P+1} a_{p-1} \int_{\max(\mathcal{D}_x)}^{\frac{kT}{E_A-\mu}} \frac{dx}{x^{p}}. \tag{30}$$

Note that Equation (29) and Equation (30) are both analytic and thus can be expressed in a closed form, which further augments both the precision and the speed of computation, as numerical integration is unnecessary. In addition to their utility in approximating flux outside the bounds of $\mathcal{D}_x$, Equation (29) and Equation (30) may be used to gauge the accuracy of computations while debugging software and even, in some cases, to approximate the flux across the whole limit of integration, E_A to E_B, as will be seen in Section A.3.

A.2.3 Look-up-tables for Riemann zeta integrals

Each of the Riemann integrals is associated with two LUT: one containing increasing values of x, beginning with $\min(\mathcal{D}_x)$ and ending with $\max(\mathcal{D}_x)$; and a second recording the

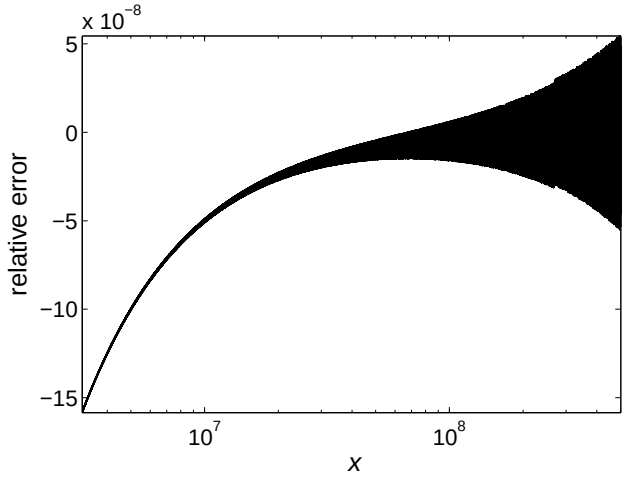

Figure 35: As x increases beyond 1×10^7, the relative error between the integrands of Equation (28) and Equation (30) begins to oscillate with increasing amplitude. This is true for $p = 1, 2, 3, 4$. This figure shows $p = 3$.

computed values of the IRZI between two successive entries in the first LUT. For example, in calculating the particle flux in a situation such that $\min(\mathcal{D}_x) < E_A < E_B < \max(\mathcal{D}_x)$, the operations given in Equation (31) are performed. Here $x_n^{(p)}$ is the smallest value in the first LUT associated with the p^{th} Riemann zeta integral greater than $kT/(E_B - \mu)$, $x_N^{(p)}$ is the largest value in the first LUT associated with the p^{th} Riemann zeta integral less than $kT/(E_A - \mu)$. In addition, and all the integrals in the inner summation are pre-computed and recorded in the second LUT associated with the p^{th} Riemann zeta integral.

$$F_P(E_A, E_B, T, \mu) = \sum_{p=1}^{P+1} a_{p-1} \left(\begin{array}{c} \int_{x_N^{(p)}}^{\frac{kT}{E_A-\mu}} \frac{dx}{x^{p+1}\left[\exp\left(\frac{1}{x}\right)-1\right]} \\ + \sum_{m=n}^{N-1} \int_{x_m^{(p)}}^{x_{m+1}^{(p)}} \frac{dx}{x^{p+1}\left[\exp\left(\frac{1}{x}\right)-1\right]} \\ + \int_{\frac{kT}{E_B-\mu}}^{x_n^{(p)}} \frac{dx}{x^{p+1}\left[\exp\left(\frac{1}{x}\right)-1\right]} \end{array} \right) \tag{31}$$

For the special case where $n = 1$, the last integral in Equation (31) is approximated by the limiting expression given in Equation (29). Similarly, for the special case where $x_N = \max(\mathcal{D}_x)$, the first integral in Equation (31) is approximated by the limiting expression given in Eq (30).

Pre-computing LUT in the manner of Equation (31) not only speeds up calculations during run time but, in general, provides more precise results. The reason is that numerical integration routines are almost exclusively based upon interpolation polynomials and the

integrands of the Riemann zeta integrals must be interpolated with polynomials of very large order. Thus, in general, numerical integration routines will have a difficult time maintaining both precision and rapidity, especially over large intervals [188]. Therefore, the method that the author adopts is to generate LUT by composite integration across $\mathcal{D}_x$.

In performing the composite integrations, the author first performs B-form least-squares spline approximations of order six to the integrand functions using MATLAB's spap2 function. The spline approximations are performed by logarithmically sampling the integrand functions five thousand times. Next, MATLAB's newknt function is employed to choose a knot sequence that divides the numerical range into five intervals. The knot sequence obtained by this procedure is shown in Figure 36 for the case $p = 2$. Next, each interval is logarithmically partitioned into sub-intervals. The number of sub-intervals in a given interval is increased until the integral across the interval converges. Table 7 gives the intervals' breakpoints for the cases $p = 1, 2, 3,$ and 4. For each of these, to obtain convergence, the first interval (small x) is broken into 80 sub-intervals, the last interval is broken into 600 sub-intervals, and the remaining three intervals are broken into ten sub-intervals.

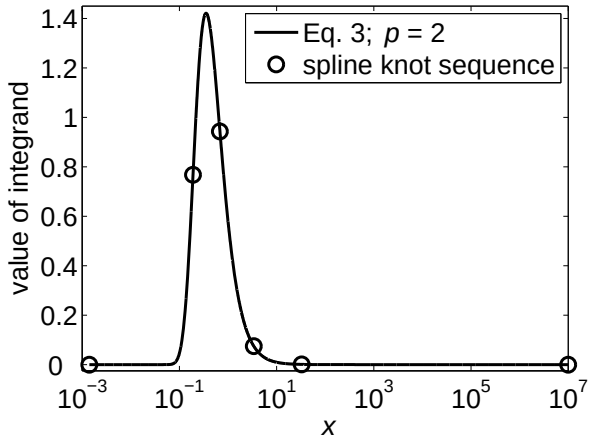

Figure 36: Integrand of the Riemann zeta integral of order two within the numerical domain $\mathcal{D}_x$. The circles indicate the interval demarcations as obtained by the spline approximation.

The next section provides evidence that the method developed in this section has a high degree of precision.

Table 7: The value of x that demarcates the i^{th} breakpoint of the integrand of the p^{th} IRZI. These demarcations are obtained by a spline approximation to the integrands.

i	$p=1$	$p=2$	$p=3$	$p=4$
1	1.4×10^{-3}	1.4×10^{-3}	1.4×10^{-3}	1.4×10^{-3}
2	5.2×10^{-1}	1.9×10^{-1}	1.3×10^{-1}	1.1×10^{-1}
3	6.7×10^{0}	6.8×10^{-1}	3.6×10^{-1}	2.4×10^{-1}
4	1.9×10^{2}	3.4×10^{0}	1.2×10^{0}	6.5×10^{-1}
5	3.8×10^{4}	3.3×10^{1}	5.4×10^{0}	2.2×10^{0}
6	1.0×10^{7}	1.0×10^{7}	1.0×10^{7}	1.0×10^{7}

A.3 Verification of high-precision

The numerical software that implements this method is benchmarked for precision by a number of means. These include comparisons between the Riemann zeta functions, and previously recorded values for solar cell limiting efficiencies from the literature.

Most importantly, the fact that the complete Riemann zeta integrals for positive integers greater than one are given in closed form allows for a comparison that provides conclusive indication of the precision of the combination of LUT and limiting expressions. For $p = 2, 3,$ and 4 the simulator yields an absolute error of order 1×10^{-14} such that the computed value was greater than the closed-form expression. The computational package is also benchmarked against a number of efficiency limit results for the single p-n junction solar cell and the IBSC.

To further judge the precision of the numerical package, results are compared with previous results obtained by the literature. Under maximum solar concentration, a solar surface temperature, T_{s}, of 5762 K, and a planetary surface temperature, T_{p} of 288 K, the efficiency limit of the single junction solar cell (SJSC) is calculated as 40.7%. This efficiency occurs when the lower limit of the emissivity, which is equal to the band-gap E_g, is 1.06 eV and the upper limit of the emissivity tends towards infinity. This compares favorably to the results of De Vos (40.8% for $E_g = 1.15$ eV) [174]. It is worth noting that under these conditions if Equation (29) is used to approximate the solar cell flux over the complete limit

of integration, $x = [0, k \times T_s/E_g]$ (where $\mu = E_g \times (1 - T_p/T_s)$ [174])–which is justified because for $E_g = E_A$ of order 1 eV the integrand of Equation (28) is dominated by the exponential term–then the solar cell particle flux may be approximated analytically. The resultant value will be slightly larger than what would be obtained from numerical calculations using Equation (28) because, for all values of x, the denominator of Equation (29) is greater than the denominator of Equation (28) . Thus a ceiling is obtained, whereby any computed efficiency above this ceiling is patently invalid. The efficiency limit computed in this manner, for the identical conditions stated in the beginning of this paragraph, establishes a ceiling of 40.8%. Using the same temperatures as listed above, but with a solar concentration of 1x, the optimum efficiency is computed as 31.0% when E_g = 1.26 eV. These results compare favorably with the work of De Vos, who records the identical efficiency when E_g = 1.30 eV [174]. The numerical package is also benchmarked on the efficiency limit of a SJSC at full concentration but with T_s = 5759 K and T_p = 300 K. The results of such calculations provide an efficiency limit of 40.6% at E_g = 1.06 eV, which compares favorably to the previously reported result under identical conditions: 40.7% at E_g = 1.06 eV [189].

Finally, the software package is benchmarked against previous calculations of the IBSC. The numerical software obtains a conversion efficiency of 63.2%, which is obtained when the effective band-gap between the conduction band and valence band is 1.95 eV and the band-gap between the intermediate band and valence band is 0.71 eV. This result compares exactly with the efficiency limit as defined here [35]. Additionally, under 1-sun illumination the simulator calculates an optimum efficiency of 46.8%, which is obtained when the effective band-gap between the conduction band and valence band is 2.40 eV and the effective band-gap between the intermediate band and valence band is 0.92 eV. This result again compares favorably with the previously reported optimized efficiency of 46.0%, which is reported to occur when the effective band-gap between the conduction band and valence band is 2.43 eV and the effective band-gap between the intermediate band and valence band is 0.93 eV [10].

The next section presents a verification of the rapidity of the method formulated herein.

A.4 Verification of rapidity

To gauge the rapidity of the method, it must be compared to other methods of calculating flux. The method is benchmarked by comparing the average durations of flux calculations as per the expressions given by Equation (26), Equation (27), Equation (28), and Equation (28)*. Here Equation (28)* signifies the use of Equation (28) with the incorporation of the LUT as well as the limiting functions given in Equation (29) and Equation (30). Table 8 shows how these different methods of calculation compare for twelve unique cases, all of which are performed with a numerical tolerance of 1×10^{-14}. These specific cases are chosen because they are typical for detailed-balance applications with internally biased operating points and applications with multiple absorbers. To minimize the temporal variability with respect to the evaluation of the twelve cases, for each case, the duration is given as the average of 500 identical calculations.

The data of Table 8, which is obtained with a 3.6 GHz processor, indicate that for nine of the twelve cases, the method that is developed herein is roughly between five times and a hundred times faster than the next fastest method. The gains in speed tend to increase as the value of μ approaches its asymptote E_A. Under most circumstances, the method developed herein requires that a numerical integration routine be called $2 \times (P + 1)$ times, which is compared to a single call if using the Bose-Einstein integral of Equation (26). However, the duration is never three times slower when compared to the calculations using Equation (26). Further, in only two of the twelve cases is the method developed herein more than three times slower than the fastest method. Yet, in applications that require the determination of the internally biased operating points, many more flux calculations must be made for μ greater than zero as compared with only a small number of flux calculations where μ is equal to zero. Therefore, for these detailed-balance applications, significant time saving may be achieved by adopting the method presented herein.

Table 8: Average duration of 500 identical flux computations for twelve unique input conditions, each of which are computed by four different methods. These conditions are selected because they are typical for detailed-balance efficiency calculations. The values of E_A, E_B and μ are given in electron-Volts

$F_P(E_A, E_B, T, \mu)$	Average duration of calculation [ms]			
	Eq. (26)	Eq. (27)	Eq. (28)	Eq. (28)*
$F_2(0.7, 1.2, 6000, 0)$	540	130	190	63
$F_2(1.2, 2.0, 6000, 0)$	710	180	180	51
$F_2(2.0, 6.0, 6000, 0)$	1700	410	310	46
$F_2(0.7, 1.2, 300, 0)$	1700	16	15	29
$F_2(1.2, 2.0, 300, 0)$	1700	10	10	29
$F_2(2.0, 6.0, 300, 0)$	15	10	10	29
$F_2(0.7, 1.2, 300, 0.6)$	1800	570	400	41
$F_2(1.2, 2.0, 300, 1.1)$	1800	560	430	41
$F_2(2.0, 6.0, 300, 1.8)$	1800	320	220	31
$F_2\big(0.7, 1.2, 300, 0.7 \times \big(1 - 10^{-9}\big)\big)$	1900	2100	3600	25
$F_2\big(1.2, 2.0, 300, 1.2 \times \big(1 - 10^{-9}\big)\big)$	1900	2100	3600	25
$F_2\big(2.0, 6.0, 300, 2.0 \times \big(1 - 10^{-9}\big)\big)$	1900	2200	3600	25

A.5 Appendix Conclusions

A method is formulated to rapidly and precisely calculate particle flux and energy flux for detailed-balance efficiency calculations. The method transforms the canonical Bose-Einstein integral into a linear combination of incomplete Riemann zeta integrals. By use of this transformation, look-up-tables are generated that record the results of pre-computed composite integration. The precision of the method is established by comparing the numerically computed values of the Riemann zeta integrals with the closed-form expressions for these integrals. An absolute error of 1×10^{-14} is obtained between the two. The rapidity is gauged by comparing the duration of various flux calculations using several different methods. It is found that, under most circumstances, the formulated method is between five times and one hundred times faster than other methods.

APPENDIX B

ABSORPTION COEFFICIENTS BASED ON PARABOLIC-BAND APPROXIMATIONS

In this appendix, the author generalizes the procedure of Rosencher and Vinter [172] is to render the absorption coefficients of the six momentum-conserving transitions. For photons in the range $(\hbar\,\omega, \hbar\,\omega + d\hbar\,\omega)$, the absorption coefficients, $\alpha_{(\mathrm{X,Y})}(\hbar\omega)$, are given in terms of the joint densities of states [121], $\rho_{j,(\mathrm{X,Y})}(\hbar\omega)$, and Fermi-Dirac statistics, $\overline{f}_{(\mathrm{X,Y})}(\hbar\omega)$ and $f_{(\mathrm{X,Y})}(\hbar\omega)$ as

$$\alpha_{(\mathrm{X,Y})}(\hbar\,\omega) = \frac{\pi\, q^2\, x^2_{(\mathrm{X,Y})}\, \hbar\,\omega}{\epsilon_o\, \hbar^2\, n_{\mathrm{op}}\, c}\, \rho_{j,(\mathrm{X,Y})}(\hbar\,\omega)\times \left[\overline{f}_{(\mathrm{X,Y})}(\hbar\,\omega) - f_{(\mathrm{X,Y})}(\hbar\,\omega)\right], \tag{32}$$

where $x_{(\mathrm{X,Y})}$ are the matrix elements of the optical interactions under the supposition that they are independent of the wavevector, ϵ_o is the permittivity of free space, n_{op} is the optical index of refraction, q is the elementary Coulomb charge, ω is the radian frequency of the photons, and c is the speed of light. The joint densities of states and Fermi-Dirac statistics are expressed as

$$\rho_{j,(\mathrm{X,Y})}(\hbar\,\omega) = \begin{cases} \dfrac{\left(2\, m_{r,(\mathrm{X,Y})}\right)^{3/2} \sqrt{\hbar\omega - \varepsilon^{k_0}_{(\mathrm{X,Y})}}}{2\,\pi^2\,\hbar^2} & \text{for } \hbar\,\omega^{i}_{(\mathrm{X,Y})} \le \hbar\,\omega \le \hbar\,\omega^{f}_{(\mathrm{X,Y})} \text{ and} \\ 0 & \text{otherwise,} \end{cases} \tag{33}$$

$$\overline{f}_{(\mathrm{X,Y})}(\hbar\,\omega) = \begin{cases} \dfrac{1}{1+\exp\left(\dfrac{\varepsilon_{\mathrm{Y}} - \frac{m_{r,(\mathrm{X,Y})}}{m_{\mathrm{Y}}}\left(\hbar\,\omega - \varepsilon^{k_0}_{(\mathrm{X,Y})}\right) - \varepsilon_{\mathrm{F,Y}}}{k_{\mathrm{B}}\, T_{\mathrm{c}}}\right)} & \text{for (X,Y) = (CL,VH),(CL,IH),(IL,VH),(IH,IL),(IH,V} \\ \dfrac{1}{1+\exp\left(\dfrac{\varepsilon_{\mathrm{Y}} + \frac{m_{r,(\mathrm{X,Y})}}{m_{\mathrm{Y}}}\left(\hbar\,\omega - \varepsilon^{k_0}_{(\mathrm{X,Y})}\right) - \varepsilon_{\mathrm{F,Y}}}{k_{\mathrm{B}}\, T_{\mathrm{c}}}\right)} & \text{for (X,Y) = (CL,IL), and} \end{cases} \tag{34a}$$

$$f_{(\mathrm{X,Y})}(\hbar\omega) = \begin{cases} \dfrac{1}{1+\exp\left(\dfrac{\varepsilon_{\mathrm{X}}+\frac{m_{r,(\mathrm{X,Y})}}{m_{\mathrm{X}}}\left(\hbar\omega-\varepsilon^{k_0}_{(\mathrm{X,Y})}\right)-\varepsilon_{\mathrm{F,X}}}{k_{\mathrm{B}}T_{\mathrm{c}}}\right)} & \text{for (X,Y) = (CL,VH),(CL,IH),(IL,VH),(IH,IL),(CL,I} \\ \dfrac{1}{1+\exp\left(\dfrac{\varepsilon_{\mathrm{X}}-\frac{m_{r,(\mathrm{X,Y})}}{m_{\mathrm{X}}}\left(\hbar\omega-\varepsilon^{k_0}_{(\mathrm{X,Y})}\right)-\varepsilon_{\mathrm{F,X}}}{k_{\mathrm{B}}T_{\mathrm{c}}}\right)} & \text{for (X,Y) = (IH,VH), where} \end{cases} \tag{34b}$$

$$m_{r,(\mathrm{X,Y})} = \begin{cases} \left(\frac{1}{m_{\mathrm{X}}}+\frac{1}{m_{\mathrm{Y}}}\right)^{-1} & \text{for (X,Y) = (CL,VH), (CL,IH), (IL,VH), (IH,IL),} \\ \left(\frac{1}{m_{\mathrm{X}}}+\frac{-1}{m_{\mathrm{Y}}}\right)^{-1} & \text{for (X,Y) = (CL,IL), and} \\ \left(\frac{-1}{m_{\mathrm{X}}}+\frac{1}{m_{\mathrm{Y}}}\right)^{-1} & \text{for (X,Y) = (IH,VH).} \end{cases} \tag{35}$$

Here, $m_{r,(\mathrm{X,Y})}$ are the reduced effective masses, k_{B} is Boltzmann's constant, and T_c is the temperature of the absorber. The upper and lower bounds of the inequalities of Equation 33 are given in Table 9. Equation 34 is written in terms of the three quasi-Fermi levels (see Figure 22). It is understood from the introduction that the carriers in the two intermediate subbands are in electro-chemical equilibrium, so that $\varepsilon_{\mathrm{F,IH}}$ is equal to $\varepsilon_{\mathrm{F,IL}}$.

Table 9: Optical absorption edges, for each element (X,Y) in the set $\mathcal{T}$ of six allowed momentum-conserving transitions, where the absorption coefficients are non-zero. The onsets and offsets of absorption are labeled as $\hbar\omega_i^{(\mathrm{X,Y})}$ and $\hbar\omega_f^{(\mathrm{X,Y})}$, respectively.

(X,Y)	$\hbar\omega^i_{(\mathrm{X,Y})}$	$\hbar\omega^f_{(\mathrm{X,Y})}$
(CL,VH)	$\varepsilon^{k_0}_{(\mathrm{CL,VH})}$	$\lim \to \infty$
(CL,IH)	$\varepsilon^{k_0}_{(\mathrm{CL,IH})}$	$\varepsilon^{k_{\max}}_{\mathrm{CI}}$
(IL,VH)	$\varepsilon^{k_0}_{(\mathrm{IL,VH})}$	$\varepsilon^{k_{\max}}_{\mathrm{IV}}$
(IH,IL)	0	$\varepsilon^{k_0}_{(\mathrm{IH,IH})}$
(CL,IL)	$\min\left(\varepsilon^{k_0}_{(\mathrm{CL,IL})}, \varepsilon^{k_{\max}}_{\mathrm{CI}}\right)$	$\max\left(\varepsilon^{k_0}_{(\mathrm{CL,IL})}, \varepsilon^{k_{\max}}_{\mathrm{CI}}\right)$
(IH,VH)	$\min\left(\varepsilon^{k_0}_{(\mathrm{IH,VH})}, \varepsilon^{k_{\max}}_{\mathrm{IV}}\right)$	$\max\left(\varepsilon^{k_0}_{(\mathrm{IH,VH})}, \varepsilon^{k_{\max}}_{\mathrm{IV}}\right)$

APPENDIX C

ABSOLUTE LOCATION OF THE QUASI-FERMI LEVELS

In this appendix, the author details the method used to identify the quasi-Fermi levels. This method hinges upon two balance equations and the capability to calculate the carrier statistics in each of the bands. The latter is done with a numerical method [190] to calculate both the complete and the incomplete Fermi-Dirac integrals.

C.1 Balance Equations

The location of the quasi-Fermi levels may be found by simultaneously solving two balance equations: a charge-neutrality condition and a charge current density condition. The charge-neutrality of an IB absorber is enforced by a balance of the electronic charge in the absorber. This balance is written in terms of the concentrations of electrons in the CB, n_{C}, holes in the IB, p_{I}, electrons in the IB, n_{I}, and holes in the valence band, p_{V}, as

$$q\left[n_{\mathrm{C}}(\varepsilon_{\mathrm{F,CL}}) - p_{\mathrm{I}}(\varepsilon_{\mathrm{F,IH}}) + n_{\mathrm{I}}(\varepsilon_{\mathrm{F,IL}}) - p_{\mathrm{V}}(\varepsilon_{\mathrm{F,VH}})\right] = 0. \tag{36}$$

Additionally, while operating in steady state, the charge current density through the IB is in balance [35]. Including the effect of nonradiative recombination the net charge current density is in balance as [44]

$$\begin{aligned} q\left[\dot{N}_{\mathrm{p,IV}} - \dot{N}_{\mathrm{s,IV}} - l\left\langle \dot{N}_{\mathrm{(I,V)}}^{\text{non-rad}} \right\rangle\right] = \\ q\left[\dot{N}_{\mathrm{p,CI}} - \dot{N}_{\mathrm{s,CI}} - l\left\langle \dot{N}_{\mathrm{(C,I)}}^{\text{non-rad}} \right\rangle\right], \end{aligned} \tag{37}$$

where $\dot{N}_{\mathrm{p,IV}}$ [$\mathrm{m^{-2}s^{-1}}$] and $\dot{N}_{\mathrm{s,IV}}$ [$\mathrm{m^{-2}s^{-1}}$] are, respectively, the photons fluxed absorbed and emitted due to photo-induced electronic transition between the IB and VB continua; $\dot{N}_{\mathrm{p,CI}}$ [$\mathrm{m^{-2}s^{-1}}$] and $\dot{N}_{\mathrm{s,CI}}$ [$\mathrm{m^{-2}s^{-1}}$] are, respectively, the photons fluxed absorbed and emitted due to photo-induced electronic transition between the CB and IB continua; $\left\langle \dot{N}_{\mathrm{(I,V)}}^{\text{non-rad}} \right\rangle$ [$\mathrm{m^{-3}s^{-1}}$] and $\left\langle \dot{N}_{\mathrm{(C,I)}}^{\text{non-rad}} \right\rangle$ [$\mathrm{m^{-3}s^{-1}}$] are the average net rates of nonradiative recombination per volume from the IB to the VB and CB to the IB, respectively; and l is the length of

the absorbing medium. The simplifying assumption of parabolic bands allows for a direct numerical computation of the carrier concentrations using the Fermi-Dirac integral. This is now shown below.

C.2 Carrier Concentrations

Solving the charge-neutrality balance equation (Equation 36) requires the computation of the carrier concentrations. In the case of parabolic bands, the carrier concentrations are written as [170]

$$n_{\mathrm{C}} = N_{\mathrm{CL}}\,\mathcal{F}_{1/2}(\eta_{\mathrm{CL}}, 0), \tag{38a}$$

$$p_{\mathrm{V}} = N_{\mathrm{VH}}\,\mathcal{F}_{1/2}(\eta_{\mathrm{VH}}, 0), \tag{38b}$$

$$\begin{aligned} n_{\mathrm{I}} = {} & +N_{\mathrm{IL}}\left[\mathcal{F}_{1/2}(\eta_{\mathrm{IL}}, 0) - \mathcal{F}_{1/2}(\eta_{\mathrm{IL}}, b_{\mathrm{IL}})\right] \\ & - N_{\mathrm{IH}}\left[\mathcal{F}_{1/2}(\eta_{\mathrm{IH}}, 0) - \mathcal{F}_{1/2}(\eta_{\mathrm{IH}}, b_{\mathrm{IH}}) - \frac{4}{3\sqrt{\pi}}\,(b_{\mathrm{IH}})^{3/2}\right], \end{aligned} \tag{38c}$$

and

$$\begin{aligned} p_{\mathrm{I}} = {} & +N_{\mathrm{IH}}\left[\mathcal{F}_{1/2}\left(\eta_{\mathrm{IH}}, 0\right) - \mathcal{F}_{1/2}\left(\eta_{\mathrm{I,H}}, b_{\mathrm{IH}}\right)\right] \\ & - N_{\mathrm{IL}}\left[\mathcal{F}_{1/2}\left(\eta_{\mathrm{IL}}, 0\right) - \mathcal{F}_{1/2}\left(\eta_{\mathrm{IL}}, b_{\mathrm{IL}}\right) - \frac{4}{3\sqrt{\pi}}\,(b_{\mathrm{IL}})^{3/2}\right]. \end{aligned} \tag{38d}$$

The carrier concentrations are given in terms of the effective densities of states, N_{X}, which are given as

$$N_{\mathrm{X}} = \frac{m_{\mathrm{X}}\,k_{\mathrm{B}}\,T_c\,\sqrt{2\,m_{\mathrm{X}}\,k_{\mathrm{B}}\,T_c}}{\pi^2\,\hbar^3}\,\frac{\sqrt{\pi}}{2}, \tag{39}$$

the incomplete Fermi-Dirac function, $\mathcal{F}_j(x, b)$, which is given as [190]

$$\mathcal{F}_j(x, b) \equiv \frac{1}{\Gamma\left(j+1\right)}\int_b^{\infty}\frac{t^j}{\exp\left(t-x\right)+1}\,dt, \tag{40}$$

and the following unitless variables:

$$\eta_{\mathrm{CL}} = \frac{\varepsilon_{\mathrm{F,CL}} - \varepsilon_{\mathrm{CL}}}{k_{\mathrm{B}}\, T_c}, \tag{41a}$$

$$\eta_{\mathrm{IH}} = \frac{\varepsilon_{\mathrm{IH}} - \varepsilon_{\mathrm{F,IH}}}{k_{\mathrm{B}}\, T_c}, \tag{41b}$$

$$\eta_{\mathrm{IL}} = \frac{\varepsilon_{\mathrm{F,IL}} - \varepsilon_{\mathrm{IL}}}{k_{\mathrm{B}}\, T_c}, \tag{41c}$$

$$\eta_{\mathrm{VH}} = \frac{\varepsilon_{\mathrm{VH}} - \varepsilon_{\mathrm{F,VH}}}{k\, T_c}, \tag{41d}$$

$$b_{\mathrm{IH}} = \frac{\varepsilon_{\mathrm{IH}} - \varepsilon_{k_{\mathrm{max}}}}{k_{\mathrm{B}}\, T_c}, \text{ and} \tag{41e}$$

$$b_{\mathrm{IL}} = \frac{\varepsilon_{k_{\mathrm{max}}} - \varepsilon_{\mathrm{IL}}}{k_{\mathrm{B}}\, T_c}. \tag{41f}$$

The carrier concentrations yield the following equation for the concentration of intermediate states in the IB, G_{I} [m^{-3}], which is used extensively in section 5.2.4. This is given as the sum of the concentration of electrons and holes in the IB, and may be written in closed form as

$$G_{\mathrm{I}} = \frac{2\, k_{\mathrm{max}}^3}{3\, \pi^2} = \frac{2^{5/2}}{3\, \pi^2\, \hbar^3} \left[\frac{m_{\mathrm{IL}}\, m_{\mathrm{IH}}}{m_{\mathrm{IL}} + m_{\mathrm{IH}}} \left(\varepsilon_{\mathrm{IH}} - \varepsilon_{\mathrm{IL}} \right) \right]^{3/2}. \tag{42}$$

REFERENCES

[1] P. Würfel, "Thermodynamic limitations to solar energy conversion," Physica E, vol. 14, no. 1-2, pp. 18–26, 2002.

[2] P. Würfel, "Thermodynamics of solar energy converters," in Next Generations Photovoltaics, A. Martí and A. Luque, Eds. Bristol and Philadelphia: Institute of Physics Publishing, 2004, ch. 3, p. 57.

[3] P. T. Landsberg and G. Tonge, "Thermodynamic energy conversion efficiencies," Journal of Applied Physics, vol. 51, p. R1, 1980.

[4] A. De Vos, Endoreversible Thermodynamics of Solar Energy Conversion. Oxford: Oxford University Press, 1992, pp. 4, 7, 18, 77, 94–6, 120–123, 124–125,125–129.

[5] W. Shockley and H. J. Queisser, "Efficiency of p-n junction solar cells," Journal of Applied Physics, vol. 32, p. 510, 1961.

[6] A. De Vos, "Detailed balance limit of the efficiency of tandem solar cells." Journal of Physics D, vol. 13, no. 5, pp. 839–46, 1980.

[7] J. Werner, R. Brendel, and H. Oueisser, "New upper efficiency limits for semiconductor solar cells," in 1994 IEEE First World Conference on Photovoltaic Energy Conversion. Conference Record of the Twenty Fourth IEEE Photovoltaic Specialists Conference-1994 (Cat.No.94CH3365-4), vol. vol.2, Waikoloa, HI, USA, 1994, pp. 1742–5.

[8] A. Martí and G. L. Araújo, "Limiting efficiencies for photovoltaic energy conversion in multigap system," Solar Energy Materials and Solar Cells, vol. 43, pp. 203–222, 1996.

[9] A. de Vos and B. Desoete, "On the ideal performance of solar cells with larger-than-unity quantum efficiency," Solar Energy Materials and Solar Cells, vol. 51, no. 3-4, pp. 413 – 24, 1998.

[10] A. Luque and A. Martí, "A metallic intermediate band high efficiency solar cell," Progress in Photovoltaics, vol. 9, no. 2, pp. 73–86, 2001.

[11] A. S. Brown and M. A. Green, "Detailed balance limit for the series constrained two terminal tandem solar cell," Physica E, vol. 14, pp. 96–100, 2002.

[12] A. Brown and M. Green, "Impurity photovoltaic effect: Fundamental energy conversion efficiency limits," Journal of Applied Physics, vol. 92, no. 3, pp. 1329–36, 2002.

[13] M. Levy and C. Honsberg, "Minimum effect of non-infinitesmal intermediate band width on the detailed balance efficiency of an intermediate band solar cell," in 4th World Conference on Photovoltaic Energy Conversion, Waikoloa, HI, USA, 2006, pp. 71–74.

[14] S.P. Bremner, M.Y. Levy, and C.B. Honsberg, "Analysis of tandem solar cell efficiencies under Am1.5G spectrum using a rapid flux calculation method," Progress in Photovoltaics, vol. -, pp. –, 2008, accepted for publication.

[15] R. Petela, "Exergy of heat radiation," ASME Journal of Heat Transfer, vol. 86, pp. 187–92, 1964.

[16] A. DeVos, C. C. Grosjean, and H. Pauwels, "On the formula for the upper limit of photovoltaic solar energy conversion efficiency," Journal of Physics D, vol. 15, no. 10, pp. 2003–15, 1982.

[17] G. Araújo and A. Martí, "Absolute limiting efficiencies for photovoltaic energy conversion," Solar Energy Materials and Solar Cells, vol. 33, no. 2, pp. 213 – 40, 1994.

[18] A. Luque and A. Martí, "Limiting efficiency of coupled thermal and photovoltaic converters," Solar Energy Materials and Solar Cells, vol. 58, no. 2, pp. 147 – 65, 1999.

[19] E. Jackson, "Areas for improvement of the semiconductor solar energy converter," in Proceedings of the Conference on the Use of Solar Energy, Tucson, Arizona, 1955, pp. 122–6.

[20] M. Wolf, "Limitations and possibilities for improvement of photovoltaic solar energy converters. Part I: Considerations for Earth's surface operation," in Proceedings of the Institute of Radio Engineers, vol. 48, no. 7, 1960, pp. 1246–63.

[21] N. Alvi, C. Backus, and G. Masden, "The potential for increasing the efficiency of photovoltaic systems by using multiple cell concepts," in Twelfth IEEE Photovoltaic Specialists Conference 1976, Baton Rouge, LA, USA, 1976, pp. 948–56.

[22] J. Loferski, "Tandem photovoltaic solar cells and increased solar energy conversion efficiency," in Twelfth IEEE Photovoltaic Specialists Conference 1976, Baton Rouge, LA, USA, 1976, pp. 957–61.

[23] A. De Vos and D. Vyncke, "Solar energy conversion: Photovoltaic versus photothermal conversion." in Fifth E. C. Photovoltaic Solar Energy Conference, Proceedings of the International Conference, Athens, Greece, 1984, pp. 186–90.

[24] P. Würfel, "The chemical potential of radiation," Journal of Physics C, vol. 15, pp. 3867–85, 1982.

[25] T. Markvart, "Thermodynamics of losses in photovoltaic conversion," Applied Physics Letters, vol. 91, no. 6, pp. 064 102 –, 2007.

[26] N. G. Anderson, "On quantum well solar cell efficiencies," Physica E, vol. 14, no. 1-2, pp. 126–31, 2002.

[27] R. King, D. Law, K. Edmondson, C. Fetzer, G. Kinsey, H. Yoon, R. Sherif, and N. Karam, "40% efficient metamorphic GaInP/GaInAs/Ge multijunction solar cells," Applied Physics Letters, vol. 90, no. 18, pp. 183 516 – 1, 2007.

[28] A. Barnett, C. Honsberg, D. Kirkpatrick, S. Kurtz, D. Moore, D. Salzman, R. Schwartz, J. Gray, S. Bowden, K. Goossen, M. Haney, D. Aiken, M. Wanlass, and K. Emery, "50% efficient solar cell architectures and designs," in Conference

Record of the 2006 IEEE 4th World Conference on Photovoltaic Energy Conversion (IEEE Cat. No. 06CH37747), Waikoloa, HI, USA, 2006, pp. 2560–4.

[29] A. Imenes and D. Mills, "Spectral beam splitting technology for increased conversion efficiency in solar concentrating systems: a review," Solar Energy Materials and Solar Cells, vol. 84, no. 1-4, pp. 19–69, 2004.

[30] P. Landsberg, H. Nussbaumer, and G. Willeke, "Band-band impact ionization and solar cell efficiency," Journal of Applied Physics, vol. 74, no. 2, p. 1451, 1993.

[31] J. Werner, S. Kolodinski, and H. Queisser, "Novel optimization principles and efficiency limits for semiconductor solar cells," Physical Review Letters, vol. 72, no. 24, pp. 3851–4, 1994.

[32] S. Kolodinski, J. Werner, T. Wittchen, and H. Queisser, "Quantum efficiencies exceeding unity due to impact ionization in silicon solar cells," Applied Physics Letters, vol. 63, no. 17, pp. 2405–7, 1993.

[33] R. Ross, "Efficiency of hot-carrier solar energy converters," Journal of Applied Physics, vol. 53, no. 5, pp. 3813–8, 1982.

[34] P. Würfel, A. Brown, T. Humphrey, and M. Green, "Particle conservation in the hot-carrier solar cell," Progress in Photovoltaics, vol. 13, no. 4, pp. 277–85, 2005.

[35] A. Luque and A. Martí, "Increasing the efficiency of ideal solar cells by photon induced transitions at intermediate levels," Physical Review Letters, vol. 78, p. 5014, 1997.

[36] A. S. Brown, M. A. Green, and R. P. Corkish, "Limiting efficiency for a multi-band solar cell containing three and four bands," Physica E, vol. 14, pp. 121–5, 2002.

[37] M. Levy and C. Honsberg, "Solar cell with an intermediate band of finite width," in process for Physical Review B, 2008.

[38] A. S. Brown and M. A. Green, "Intermediate band solar cell with many bands: Ideal performance," Journal of Applied Physics, vol. 94, pp. 6150–8, 2003.

[39] M. Green, "Multiple band and impurity photovoltaic solar cells: general theory and comparison to tandem cells," Progress in Photovoltaics, vol. 9, no. 2, pp. 137–44, 2001.

[40] P. Würfel, "Basic principles of solar cells and the possible impact of nano-structures," in Proceedings of the 3rd World Conference on Photovoltaic Energy Conversion, vol. C, Osaka, Japan, 2003, pp. 2672–5.

[41] A. Luque, A. Martí, C. Stanley, N. López, L. Cuadra, D. Zhou, J. L. Pearson, and A. McKee, "General equivalent circuit for intermediate band devices: potentials, currents and electroluminescence," Journal of Applied Physics, vol. 96, no. 1, pp. 903–9, 2004.

[42] T. Trupke and P. Würfel, "Improved spectral robustness of triple tandem solar cells by combined series/parallel interconnection," Journal of Applied Physics, vol. 96, no. 4, pp. 2347–51, 2004.

[43] W. Shockley and W. T. Read Jr., "Statistics of the recombinations of holes and electrons," Physical Review, vol. 87, pp. 835–842, 1952.

[44] M. Y. Levy and C. Honsberg, "Intraband absorption in solar cells with an intermediate band," submitted to IEEE Electron Device Letters, 2007.

[45] E. F. Schubert, "Cambridge studies in semiconductor physics and microelectronic engineering:1," in Doping in III-V Semiconductors, H. Ahmed, M. Pepper, and A. Broers, Eds. Cambridge, UK: Cambridge University Press, 1993, ch. 1, pp. 41–44.

[46] P. Wahnón and C. Tablero, "*Ab initio* electronic structure calculations for metallic intermediate band formation in photovoltaic materials," Physical Review B, vol. 65, no. 16, pp. 165 115 – 1, 2002.

[47] C. Tablero and P. Wahnón, "Analysis of metallic intermediate-band formation in photovoltaic materials," Applied Physics Letters, vol. 82, no. 1, pp. 151–3, 2003.

[48] K. Yu, W. Walukiewicz, J. Wu, W. Shan, J. Beeman, M. Scarpulla, O. Dubon, and P. Becla, "Diluted II-VI oxide semiconductors with multiple band gaps," Physical Review Letters, vol. 91, no. 24, pp. 246 403–1, 2003.

[49] C. Tablero, "Electronic and magnetic properties of zns doped with cr," Physical Review B, vol. 74, no. 19, pp. 195 203–1, 2006.

[50] P. Palacios, J. Fernandez, K. Sanchez, J. Conesa, and P. Wahnon, "First-principles investigation of isolated band formation in half-metallic $ti_xga_{1-x}p$ (x=0.3125-0.25)," Physical Review B, vol. 73, no. 8, pp. 85 206 – 1, 2006.

[51] C. Tablero, "Correlation effects and electronic properties of Cr-substituted SZn with an intermediate band," Journal of Chemical Physics, vol. 123, no. 11, p. 114709, 2005.

[52] D. Reynolds and S. Czyzak, "Mechanism for photovoltaic and photoconductivity effects in activated CdS crystals," Physical Review, vol. 96, no. 6, p. 1705, 1954.

[53] G. Guettler and H.J. Queisser, "Impurity photovoltaic effect in silicon," Energy Conversion, vol. 10, no. 2, pp. 51–5, 1970.

[54] J. Bruns, W. Seifert, P. Wawer, H. Winnicke, D. Braunig, and H. Wagemann, "Improved efficiency of crystalline silicon solar cells due to he^+ implantation," Applied Physics Letters, vol. 64, no. 20, pp. 2700–2, 1994.

[55] H. Kasai, T. Sato, and H. Matsumura, "Impurity photovoltaic effect in crystalline silicon solar cells," in Conference Record of the Twenty Sixth IEEE Photovoltaic Specialists Conference - 1997 (Cat. No.97CB36026), 1997, pp. 215–18.

[56] S. P. Bremner, R. Corkish, and C. B. Honsberg, "Detailed balance efficiency limits with quasi-fermi level variations," IEEE Transactions on Electron Devices, vol. 46, no. 10, pp. 1932–9, 1999.

[57] M. Green, "Prospects for photovoltaic efficiency enhancement using low-dimensional structures," Nanotechnology, vol. 11, no. 4, pp. 401–5, 2000.

[58] K. Barnham, B. Braun, J. Nelson, M. Paxman, C. Button, J. Roberts, and C. Foxon, "Short-circuit current and energy efficiency enhancement in a low-dimensional structure photovoltaic device," Applied Physics Letters, vol. 59, no. 1, pp. 135–7, 1991.

[59] A. Martí, L. Cuadra, and A. Luque, "Quantum dot intermediate band solar cell," in Conference Record of the Twenty-Eighth IEEE Photovoltaic Specialists Conference, Anchorage, AK, USA, 2000, pp. 940–3.

[60] A. Martí, L. Cuadra, and A. Luque, "Partial filling of a quantum dot intermediate band for solar cells," IEEE Transactions on Electron Devices, vol. 48, no. 10, pp. 2394–9, 2001.

[61] A. Martí, L. Cuadra, and A. Luque, "Intermediate band solar cells," in Next Generations Photovoltaics; High Efficiency through Full Spectrum Utilization, A. Martí and A. Luque, Eds. Bristol: Institute of Physics Publishing, 2004, ch. 7, pp. 150–160.

[62] A. Luque, A. Martí, N. López, E. Antolin, E. Cánovas, C. Stanley, C. Farmer, L. J. Caballero, L. Cuadra, and J. L. Balenzategui, "Experimental analysis of the quasi-fermi level split in quantum dot intermediate-band solar cells," Applied Physics Letters, vol. 87, no. 8, p. 083505, 2005.

[63] A. Luque, A. Martí, N. López, E. Antolin, E. Cánovas, C. Stanley, C. Farmer, and P. Diaz, "Operation of the intermediate band solar cell under nonideal space charge region conditions and half filling of the intermediate band," Journal of Applied Physics, vol. 99, no. 9, pp. 94 503–1–9, 2006.

[64] A. Martí, E. Antolín, C. Stanley, C. Farmer, N. López, P. Díaz, E. Cánovas, P. Linares, and A. Luque, "Production of photocurrent due to intermediate-to-conduction-band transitions: A demonstration of a key operating principle of the intermediate-band solar cell," Physical Review Letters, vol. 97, no. 24, pp. 247 701/1–4, 2006.

[65] A. G. Norman, M. C. Hanna, P. Dippo, D. H. Levi, R. C. Reedy, J. S. Ward, and M. M. Al-Jassim, "InGaAs/GaAs QD superlattices: MOVPE growth, structural and optical characterization, and application in intermediate-band solar cells," in Conference Record of the 31st IEEE Photovoltaic Specialists Conference, Orlando, FL, USA, 2005, pp. 43–8.

[66] M. Y. Levy and C. Honsberg, "Nanostructured absorbers for multiple transition solar cells," IEEE Transactions on Electron Devices, vol. -, no. -, p. in print, 2008.

[67] A. Martí, N. López, E. Antolín, E. Cánovas, A. Luque, C. Stanley, C. Farmer, and P. Díaz, "Emitter degradation in quantum dot intermediate band solar cells," Applied Physics Letters, vol. 90, no. 23, pp. 233 510 – 1, 2007.

[68] C. Tablero, A. J. Garcia, J. J.Fernandez, P. Palacios, and P. Wahnón, "First principles characterization of direct transitions for high efficiency new photovoltaic materials," Computational Materials Science, vol. 27, no. 1-2, p. 58, 2003.

[69] C. Tablero, P. Palacios, J. Fernandez, and P. Wahnon, "Properties of intermediate band materials," Solar Energy Materials and Solar Cells, vol. 87, no. 1-4, pp. 323–31, 2005.

[70] C. Tablero, "Analysis of the electronic properties of intermediate band materials as a function of impurity concentration," Physical Review B, vol. 72, no. 3, pp. 35 213 – 1, 2005.

[71] C. Tablero, "Electronic and magnetic properties of ZnS doped with Cr," Physical Review B, vol. 74, no. 19, pp. 195 203 – 1, 2006.

[72] C. Tablero, "Survey of intermediate band materials based on ZnS and ZnTe semiconductors," Solar Energy Materials and Solar Cells, vol. 90, no. 5, pp. 588–596, 2006.

[73] P. Palacios, K. Sanchez, J. Conesa, and P. Wahnon, "First principles calculation of isolated intermediate bands formation in a transition metal-doped chalcopyrite-type semiconductor," Physica Status Solidi A, vol. 203, no. 6, pp. 1395–401, 2006.

[74] W. Kohn and L. Sham, "Self-consistent equations including exchange and correlation effects," Physical Review, vol. 140, no. A, p. 1133, 1965.

[75] O. Gunnarsson and B. Lundqvist, "Exchange and correlation in atoms, molecules, and solids by the spin-density formalism," Physical Review B, vol. 13, no. 10, pp. 4274–98, 1976.

[76] J. Perdew, E. McMullen, and A. Zunger, "Density-functional theory of the correlation energy in atoms and ions: a simple analytic model and a challenge," Physical Review A (General Physics), vol. 23, no. 6, pp. 2785 – 9, 1981.

[77] W. Walukiewicz, K. Yu, J. Wu, J.W. Ager III, W. Shan, M. Scrapulla, O. Dubon, and P. Becla, "Highly mismatched alloys for intermediate band solar cells," Thin-Film Compound Semiconductor Photovoltaics. Symposium (Materials Research Society Symposium Proceedings Vol.865), pp. 125–30, 2005.

[78] K. Yu, W. Walukiewicz, J.W. Ager III, D. Bour, R. Farshchi, O. Dubon, S. Li, I. Sharp, and E. Haller, "Multiband GaNAsP quaternary alloys," Applied Physics Letters, vol. 88, no. 9, p. 092110, 2006.

[79] W. Shan, W. Walukiewicz, J.W. Ager III, E. Haller, J. Geisz, D. Friedman, J. Olson, and S. Kurtz, "Band anticrossing in gainnas alloys," Physical Review Letters, vol. 82, no. 6, pp. 1221 – 4, 1999.

[80] W. Walukiewicz, W. Shan, J.W. Ager III, D. Chamberlin, E. Haller, J. Geisz, D. Friedman, J. Olson, and S. Kurtz, "Nitrogen-induced modification of the electronic structure of group III-N-V alloys," in Photovoltaics for the 21st Century. Proceedings of the International Symposium. (Electrochem. Soc. Proceedings Vol.99-11), Seattle, WA, USA, 1999, pp. 190–9.

[81] W. Walukiewicz, W. Shan, K. Yu, J.W. Ager III, E. Haller, I. Miotkowski, M. Seong, H. Alawadhi, and A. Ramdas, "Interaction of localized electronic states with the conduction band: band anticrossing in II-VI semiconductor ternaries," Physical Review Letters, vol. 85, no. 7, pp. 1552–5, 2000.

[82] J. Wu, W. Shan, and W. Walukiewicz, "Band anticrossing in highly mismatched III-V semiconductor alloys," Semiconductor Science and Technology, vol. 17, no. 8, pp. 860–9, 2002.

[83] N. Ekins-Daukes, C. Honsberg, and M. Yamaguchi, "Signature of intermediate band materials from luminescence measurements," in Conference Record of the Thirty-First IEEE Photovoltaic Specialist Conference (IEEE Cat. No. 05CH37608), Lake Buena Vista, FL, USA, 2005, pp. 49–54.

[84] L. Cuadra, A. Martí, and A. Luque, "Influence of the overlap between the absorption coefficients on the efficiency of the intermediate band solar cell," IEEE Transactions on Electron Devices, vol. 51, no. 6, pp. 1002–7, 2004.

[85] M. Zundel, W. Csaszar, and A. Endrös, "Detailed experimental investigation of a local defect layer used for si solar cells," Applied Physics Letters, vol. 67, no. 26, pp. 3945 – 7, 1995.

[86] K. Yu, W. Walukiewicz, M. Scarpulla, O. Dubon, W. Shan, J. Wu, J. Beeman, and P. Becla, "Synthesis and properties of highly mismatched ii-o-vi alloys," IEE Proceedings-Optoelectronics, vol. 151, no. 5, pp. 452 – 9, 2004.

[87] J. I. Pankove, Optical processes in semiconductors, ser. Prentice-Hall electrical engineering series. Solid state physical electronics series. Englewood Cliffs, New Jersey: Prentice-Hall, 1971, vol. 11, pp. 93–4.

[88] M. Cardona, Modulation Spectroscopy, ser. Solid State Physics: Advances in Research and Applications. New York and London: Academic Press, 1969, vol. 11.

[89] D. Aspnes, "Third-derivative modulation spectroscopy with low-field electroreflectance," Surface Science, vol. 37, pp. 418 – 42, 1973.

[90] F. Pollak and H. Shen, "Modulation spectroscopy of semiconductors: bulk/thin film, microstructures, surfaces/interfaces and devices," Materials Science & Engineering R: Reports, vol. R10, no. 7-8, pp. 275 – 374, 1993.

[91] F. Ragay, J. Wolter, A. Martí, and G. Araújo, "Experimental analysis of GaAs-InGaAs MQW solar cells," in 1994 IEEE First World Conference on Photovoltaic Energy Conversion. Conference Record of the Twenty Fourth IEEE Photovoltaic Specialists Conference-1994 (Cat.No.94CH3365-4), vol. 2, Waikoloa, HI, USA, 1994, pp. 1754–8.

[92] N. Ekins-Kaukes, J. Barnes, K. Barnham, J. Connolly, M. Mazzer, J. Clark, R. Grey, G. Hill, M. Pate, and J. Roberts, "Strained and strain-balanced quantum well devices for high-efficiency tandem solar cells," Solar Energy Materials and Solar Cells, vol. 68, no. 1, pp. 71–87, 2001.

[93] N. Ekins-Daukes, K. Barnham, J. Connolly, J. Roberts, J. Clark, G. Hill, and M. Mazzer, "Strain-balanced GaAsP/InGaAs quantum well solar cells," Applied Physics Letters, vol. 75, no. 26, pp. 4195–7, 1999.

[94] K. Barnham, I. Ballard, J. Connolly, N. Ekins-Daukes, B. Kluftinger, J. Nelson, C. Rohr, and M. Mazzer, "Recent results on quantum well solar cells," Journal of Materials Science: Materials in Electronics, vol. 11, no. 7, pp. 531 – 6, 2000.

[95] N. López, A. Martí, A. Luque, C. Stanley, C. Farmer, and P. Díaz, "Experimental analysis of the operation of quantum dot intermediate band solar cells," Journal of

Solar Energy Engineering, Transactions of the ASME, vol. 129, no. 3, pp. 319–322, 2007.

[96] M. Y. Levy and C. Honsberg, "Modeling of nanostructured materials; photoabsorption based on parabolic band approximations (contract XAT-5-44277-01)," National Renewable Energy Laboratory, Golden, CO, USA, Tech. Rep., Aug. 3 2007.

[97] M. Y. Levy and C. Honsberg, "Absorption coefficients of an intermediate band absorbing medium under parabolic band approximations," in process for Physical Review B, 2008.

[98] M. Y. Levy, N. J. Ekins-Daukes, and C. Honsberg, "Photoluminescent signature of absorbing medium with deep levels based upon absorption coefficients derived from parabolic-band approximations," in Proc. EUPVSEC 22, Milan, Italy, 2007, pp. –.

[99] E. Tsui, J. Nelson, K. Barnham, C. Button, and J. Roberts, "Determination of the quasi-fermi-level separation in single-quantum-well *p-i-n* diodes," Journal of Applied Physics, vol. 80, no. 8, pp. 4599–603, 1996.

[100] J. Nelson, J. Barnes, N. Ekins-Daukes, B. Kluftinger, E. Tsui, K. Barnham, C. T. Foxon, T. Cheng, and J. S. Roberts, "Observation of suppressed radiative recombination in single quantum well p-i-n photodiodes," Journal of Applied Physics, vol. 82, no. 12, pp. 6240–6, 1997.

[101] N. Ekins-Daukes, J. Nelson, J. Barnes, K. Barnham, B. Kluftinger, E. Tsui, C. Foxon, T. Cheng, and J. Roberts, "Radiative currents in quantum-well solar cells," Physica E, vol. 2, no. 1-4, pp. 171–6, 1998.

[102] B. Kluftinger, K. Barnham, J. Nelson, T. Foxon, and T. Cheng, "Temperature-dependent study of the quasi-fermi level separation in double quantum well p-i-n structures," in Microelectronic Engineering, vol. 51-52, no. 1-4, Antalya, Turkey, 2000, pp. 265–74.

[103] B. Kluftinger, K. Barnham, J. Nelson, T. Foxon, and T. Cheng, "Temperature-dependent study of the radiative losses in double-quantum well solar cells," Solar Energy Materials and Solar Cells, vol. 66, no. 1-4, pp. 501–9, 2001.

[104] K. Barnham, I. Ballard, J. Connolly, N. Ekins-Daukes, B. Kluftinger, J. Nelson, and C. Rohr, "Quantum well solar cells," Physica E, vol. 14, no. 1-2, pp. 27 – 36, 2002.

[105] K. Barnham, P. Abbott, I. Ballard, D. Bushnell, J. Connolly, N. Ekins-Daukes, M. Mazzer, J. Nelson, C. Rohr, T. Tibbits, R. Airey, G. Hill, and J. Roberts, "Recent results on quantum well solar cells," in Proceedings of 3rd World Conference on Photovoltaic Energy Conversion (IEEE Cat. No.03CH37497), vol. Vol. 1, Osaka, Japan, 2003, pp. 606 – 11.

[106] N. Ekins-Daukes, C. Calder, I. Ballard, K. Barnham, J. Nelson, J. Roberts, and G. Hill, "Quantum well and bulk quasi-fermi level behaviour under illuminated conditions," in Proceedings of 3rd World Conference on Photovoltaic Energy Conversion (IEEE Cat. No.03CH37497), vol. Vol.3, 2003, pp. 2702 – 5.

[107] C. Summonte, M. Biavati, E. Gabilli, R. Galloni, S. Guerri, R. Rizzoli, and F. Zignani, "Spectral behavior of solar cells based on the 'junction near local defect layer' design," Applied Physics Letters, vol. 63, no. 6, pp. 785–7, 1993.

[108] M. Keevers and M. Green, "Extended infrared response of silicon solar cells and the impurity photovoltaic effect," Solar Energy Materials and Solar Cells, vol. 41-42, pp. 195–204, 1996.

[109] H. Kasai and H. Matsumura, "Study for improvement of solar cell efficiency by impurity photovoltaic effect," in Solar Energy Materials and Solar Cells, vol. 48, no. 1-4, 1997, pp. 93–100.

[110] N. Ekins-Daukes, I. Ballard, C. Calder, K. Barnham, G. Hill, and J. Roberts, "Photovoltaic efficiency enhancement through thermal up-conversion," Applied Physics Letters, vol. 82, no. 12, pp. 1974 – 6, 2003.

[111] K. Barnham, J. Connolly, P. Griffin, G. Haarpaintner, J. Nelson, E. Tsui, A. Zachariou, J. Osborne, C. Button, G. Hill, M. Hopkinson, M. Pate, J. Roberts, and T. Foxon, "Voltage enhancement in quantum well solar cells," Journal of Applied Physics, vol. 80, no. 2, pp. 1201–6, 1996.

[112] B. Kochman, A. D. Stiff-Roberts, S. Chakrabarti, J. D. Phillips, S. Krishna, J. Singh, and P. Bhattacharya, "Absorption, carrier lifetime, and gain in InAs-GaAs quantum-dot infrared photodetectors," IEEE Journal of Quantum Electronics, vol. 39, no. 3, pp. 459–67, 2003.

[113] S. Kettemann and J.-K. Guillemoles, "Limiting efficiency of LDS solar cells," in 13th European Photovoltaic Solar Energy Conference, Nice, France, 1995, pp. 119–21.

[114] P. Gibart, F. Auzel, J.-C. Guillaume, and K. Zahraman, "Below band-gap IR response of substrate-free GaAs solar cells using two-photon up-conversion," Japanese Journal of Applied Physics 1, vol. 35, no. 8, pp. 4401–2, 1996.

[115] T. Trupke, M. A. Green, and P. Würfel, "Improving solar cell efficiencies by down-conversion of high-energy photons," Jounal of Applied Physics, vol. 92, pp. 1668–74, 2002.

[116] F. Hatami, W. Masselink, and J. Harris, "Colour-tunable light-emitting diodes based on InP/GaP nanostructures," Nanotechnology, vol. 17, no. 15, pp. 3703–6, 2006.

[117] S.-D. Chen, Y.-Y. Chen, and S.-C. Lee, "Transverse-electric-field-enhanced response in InAs/AlGaAs/GaAs quantum-dot infrared photodetectors," Applied Physics Letters, vol. 86, no. 25, p. 253104, 2005.

[118] A. De Vos and B. Desoete, "On the ideal performance of solar cells with larger-than-unity quantum efficiency," Solar Energy Materials and Solar Cells, vol. 51, no. 3-4, pp. 413–24, 1998.

[119] A. Luque, A. Martí, and L. Cuadra, "Thermodynamic consistency of sub-bandgap absorbing solar cell proposals," IEEE Transactions on Electron Devices, vol. 48, no. 9, pp. 2118–24, 2001.

[120] T. Trupke, M. A. Green, and P. Würfel, Journal of Applied Physics, vol. 92, p. 1668, 2002.

[121] P. Bardeen, F. J. Blatt, and L. H. Hall, "Indirect transitions from the valence to the conduction bands," in Photoconductivity Conference, R. G. Breckenridge, Ed., Atlantic City, NJ, USA, 1954, pp. 146–154.

[122] M. Y. Levy and C. Honsberg, "Rapid and precise calculations of energy and particle flux for detailed-balance photovoltaic applications," Solid-State Electronics, vol. 50, pp. 1400–5, 2006.

[123] R. C. Alig, S. Bloom, and C. W. Stuck, "Scattering by ionization and phonon emission in semiconductors," Physical Review B, vol. 22, no. 12, pp. 5565–82, 1980.

[124] R. Schaller and V. Klimov, "High efficiency carrier multiplication in PbSe nanocrystals: Implications for solar energy conversion," Physical Review Letters, vol. 92, no. 18, pp. 186 601–1, 2004.

[125] M. C. Beard, K. P. Knutsen, P. Yu, J. M. Luther, Q. Song, W. K. Metzger, R. J. Ellingson, and A. J. Nozik, "Multiple exciton generation in colloidal silicon nanocrystals," Nano Letters, vol. 7, no. 8, pp. 2506–12, 2007.

[126] O. Madelung, Introduction to Solid-State Theory. Heidelberg: Springer-Verlag, 1978, pp. 287,382,435–447.

[127] O. L. Lazarenkova and A. A. Balandin, "Miniband formation in a quantum dot crystal," Journal of Applied Physics, vol. 89, pp. 5509–15, 2001.

[128] A. Martí, L. Cuadra, and A. Luque, "Design constraints of the quantum-dot intermediate band solar cell," Physica E, vol. 14, no. 1-2, pp. 150–7, 2002.

[129] M. Y. Levy, A. Martí, C. Honsberg, and A. Luque, "Calculation of the band properties of quantum dot intermediate band solar cells with hydrogenic impurities," in 19th European Photovoltaic Energy Conference, Paris, France, 2004, pp. 332–5.

[130] A. Sibille, "Miniband transport," in Semiconductor Superlattices; Growth and Electronic Properties, H. T. Grahn, Ed. Singapore: World Scientific, 1995, ch. 2, p. 37.

[131] M. Levy, C. Honsberg, A. Marti, and A. Luque, "Quantum dot intermediate band solar cell material systems with negligible valence band offsets," in Conference Record of the Thirty-First IEEE Photovoltaic Specialist Conference (IEEE Cat. No. 05CH37608), Lake buena Vista, FL, USA, 2005, pp. 90–3.

[132] Y. Sugiyama, Y. Nakata, K. Imamura, S. Muto, and N. Yokoyama, "Stacked InAs self-assembled quantum dots on (001) GaAs grown by molecular beam epitaxy," Japanese Journal of Applied Physics, Part 1 (Regular Papers & Short Notes), vol. 35, no. 2B, pp. 1320–4, 1996.

[133] K. Shiramine, Y. Horisaki, D. Suzuki, S. Itoh, Y. Ebiko, S. Muto, Y. Nakata, and N. Yokoyama, "TEM observation of threading dislocations in InAs self-assembled quantum dot structure," Journal of Crystal Growth, vol. 205, no. 4, pp. 461–6, 1999.

[134] C. H. Roh, Y. J. Park, K. M. Kim, Y. M. Park, F. K. Kim, and K. B. Shim, "Defect generation in multi-stacked InAs quantum dot/GaAs structures," Journal of Crystal Growth, vol. 226, no. 1, pp. 1–7, 2001.

[135] K. Stewart, M. Buda, J. Wong-Leung, L. Fu, C. Jagadish, A. Stiff-Roberts, and P. Bhattacharya, "Influence of rapid thermal annealing on a 30 stack InAs/GaAs quantum dot infrared photodetector," Journal of Applied Physics, vol. 94, no. 8, pp. 5283–9, 2003.

[136] M. Gutiérrez, M. Hopkinson, H. Y. Liu, J. S. Ng, M. Herrera, D. González, R. Garcia, and R. Beanland, "Strain interactions and defect formation in stacked InGaAs quantum dot and dot-in-well structures," Physica E, vol. 26, no. 1-4, pp. 245–251, 2005.

[137] K. Akahane, N. Ohtani, Y. Okada, and M. Kawabe, "Fabrication of ultra-high density InAs-stacked quantum dots by strain-controlled growth on InP(311)B substrate," Journal of Crystal Growth, vol. 245, pp. 31–36, 2002.

[138] P. Lever, H. H. Tan, and C. Jagadish, "InGaAs quantum dots grown with GaP strain compensation layers," Journal of Applied Physics, vol. 95, no. 10, pp. 5710–4, 2004.

[139] Z. H. Zhang, C. F. Xu, K. C. Hsieh, and K. Y. Cheng, "Defect-free 50-layer strain-balanced InAs quantum dots grown on InAlGaAs/InP for infrared photodetector applications," Journal of Crystal Growth, vol. 278, no. 1-4, pp. 61–6, 2005.

[140] K. Akahane, N. Yamamoto, and N. Ohtani, "Long-wavelength light emission from InAs quantum dots covered by GaAsSb grown on GaAs substrates," Physica E, vol. 21, pp. 295–299, 2004.

[141] Z. H. Zhang, K. Y. Cheng, C. F. Xu, and K. C. Hsieh, "Defect-free 100-layer strain-balanced InAs quantum dot structure grown on InP substrate," Applied Physics Letters, vol. 89, no. 6, p. 63115, 2005.

[142] T. Trupke, M. A. Green, and P. Würfel, "Improving solar cell efficiencies by up-conversion of sub-band-gap light," Journal of Applied Physics, vol. 92, p. 4117, 2002.

[143] U. Laheld, F. Pedersen, and P. Hemmer, "Excitons in type-II quantum dots: finite offsets," Physical Review B, vol. 52, no. 4, pp. 2697–703, 1995.

[144] C.-K. Sun, A. Wang, J. Bowers, B. Brar, H.-R. Blank, H. Kroemer, and M. Pilkuhn, "Optical investigations of the dynamic behavior of GaSb/GaAs quantum dots," Applied Physics Letters, vol. 68, no. 11, pp. 1543–5, 1996.

[145] H. Munekata, T. Smith, III, F. Fang, L. Esaki, and L. Chang, "Electrons and holes in InAs-Ga(Al)Sb(As) quantum wells," Journal de Physique Colloque, vol. 48, no. C-5, pp. 151–4, 1987.

[146] I. Vurgaftman, J. R. Meyer, and L. R. Ram-Mohan, "Band parameters for III-V compound semiconductors and their alloys," Journal of Applied Physics, vol. 89, no. 11, pp. 5815–5875, 2001.

[147] N. Ekins-Daukes, K. Kawaguchi, and J. Zhang, "Strain-balanced criteria for multiple quantum well structures and its signature in X-ray rocking curves," Crystal Growth & Design, vol. 2, no. 4, pp. 287–92, 2002.

[148] N. Nuntawong, S. Birudavolu, C. Hains, S. Huang, H. Xu, and D. Huffaker, "Effect of strain-compensation in stacked 1.3 μm InAs/GaAs quantum dot active regions grown by metalorganic chemical vapor deposition," Applied Physics Letters, vol. 85, no. 15, pp. 3050–2, 2004.

[149] E. Ribeiro, R. Maltez, W. Carvalho, D. Ugarte, and G. Medeiros-Ribeiro, "Optical and structural properties of InAsP ternary self-assembled quantum dots embedded in GaAs," Applied Physics Letters, vol. 81, no. 16, pp. 2953–5, 2002.

[150] R. L. Maltez, E. Ribeiro, W. Carvalho Jr., D. Ugarte, and G. Medeiros-Ribeiro, "Controlling alloy composition of InAsP self-assembled quantum dots embedded in GaAs," Journal of Applied Physics, vol. 94, no. 5, pp. 3051–6, 2003.

[151] H. Y. Liu, M. J. Steer, T. J. Badcock, D. J. Mowbray, M. S. Skolnick, P. Navaretti, K. M. Groom, M. Hopkinson, and R. A. Hogg, "Long-wavelength light emission and lasing from InAs/GaAs quantum dots covered by a GaAsSb strain-reducing layer," Applied Physics Letters, vol. 86, p. 143108, 2005.

[152] H. Y. Liu, M. J. Steer, T. J. Badcock, D. J. Mowbray, M. S. Skolnick, F. Suarez, J. Ng, M. Hopkinson, and J. P. R. David, "Room-temperature 1.6 μm light emission from InAs/GaAs quantum dots with a thin GaAsSb cap layer," Journal of Applied Physics, vol. 99, p. 46104, 2006.

[153] M. Copel, M. C. Reuter, E. Kaxiras, and R. M. Tromp, "Surfactants in epitaxial growth," Physical Review Letters, vol. 63, no. 6, pp. 632–5, 1989.

[154] M. Larsson, W. Ni, K. Joelsson, and G. Hansson, "Growth of high quality Ge films on Si(l l l) using Sb as surfactant," Applied Physics Letters, vol. 65, no. 11, pp. 1409–11, 1994.

[155] H. Shimizu and S. Saravanan, "Buffer-material dependence of InAs quantum dots on GaAs substrate," Applied Physics Letters, vol. 88, no. 4, p. 41119, 2006.

[156] C. Tablero, "Optical properties for $Ga_{32}P_{31}Cr$ and Ga_{31} $P_{32}Cr$ intermediate band materials," Solar Energy Materials and Solar Cells, vol. 90, no. 2, pp. 203–12, 2006.

[157] D. L. Dexter, "Absorption near the edge in insulators," in Photoconductivity Conference, R. G. Breckenridge, Ed., Atlantic City, NJ, USA, 1954, pp. 155–83.

[158] H. Y. Fan, M. L. Shepherd, and W. Spitzer, "Infrared absorption and energy-band structure of germanium and silicon," in Photoconductivity Conference, R. G. Breckenridge, Ed., Atlantic City, NJ, USA, 1954, pp. 184–202.

[159] H. Fan, "Infra-red absorption in semiconductors," Reports on Progress in Physics, vol. 19, pp. 107–154, 1956.

[160] S. Pantelides and C. Sah, "Theory of localized states in semiconductors. i. new results using an old method," Physical Review B, vol. 10, no. 2, pp. 621–37, 1974.

[161] E. J. Johnson, "Absorption near the fundamental edge," in Semiconductors and Semimetals, R. K. Willardon and A. C. Beer, Eds. New York: Academic Press, 1967, vol. 3, ch. 6, p. 203.

[162] M. Asada, Y. Miyamoto, and Y.Suematsu, "Gain and the threshold of three dimensional quantum-box lasers," IEEE Journal of Quantum Electronics, vol. QE-22, no. 9, pp. 1915–21, 1986.

[163] W.-Y. Wu, J. Schulman, T. Hsu, and U. Efron, "Effect of size nonuniformity on the absorption spectrum of a semiconductor quantum dot system," Applied Physics Letters, vol. 51, no. 10, pp. 710–2, 1987.

[164] K. Kang, B. McGinnis, Sandalphon, Y. Hu, S. Koch, N. Peyghambarian, A. Mysyrowicz, L. Liu, and S. Risbud, "Confinement-induced valance-band mixing in cds quantum dots observed by two-photon spectroscopy," Physical Review B, vol. 45, no. 7, pp. 3465–8, 1992.

[165] T. Trupke, M. A. Green, and P. Würfel, "Improving solar cell efficiencies by up-conversion of sub-band-gap light," Jounal of Applied Physics, vol. 92, pp. 4117–22, 2002.

[166] K. Choi, B. Levine, C. Bethea, J. Walker, and R. Malik, "Infrared photoelectron tunneling spectroscopy of strongly coupled quantum wells," Physical Review B, vol. 39, no. 11, pp. 8029–32, 1989.

[167] E. Martinet, E. Rosencher, F. Luc, P. Bois, E. Costard, and S. Delaître, "Switchable bicolor (5.5-9.0 μm) infrared detector using asymmetric GaAs/AlGaAs multiquantum well," Applied Physics Letters, vol. 61, no. 3, pp. 246–8, 1992.

[168] S. Chakrabarti, X. Su, P. Bhattacharya, G. Ariyawansa, and A. Perera, "Characteristics of a multicolor InGaAs-GaAs quantum-dot infrared photodetector," IEEE Photonics Technology Letters, vol. 17, no. 1, pp. 178–180, 2005.

[169] A. M. Stoneham, Theory of Defects in Solids: Electronic Structure of Defects in Insulators and Semiconductors. Oxford: Clarendon Press, 1975, p. 274.

[170] M. Y. Levy and N. M. Elwakil, "Quarterly review," National Renewable Energy Laboratory, Golden, CO, USA, Tech. Rep., June 2006.

[171] M. Y. Levy and C. Honsberg, "Quarterly review: Salient features of intermediate band absorbing media," National Renewable Energy Laboratory, Golden, CO, USA, Tech. Rep., July 2007.

[172] E. Rosencher and B. Vinter, Optoelectronics, english edition ed. Cambidge, UK: Cambridge University Press, 2002, chapter 7, pp. 300, 301–4.

[173] A. J. Nozik, "Quantum dot solar cells," Physica E, vol. 14, pp. 115–20, 2002.

[174] A. DeVos, Endoreversible Thermodynamics of Solar Energy Conversion. Oxford: Oxford University Press, 1992, pp. 1–12,10,21,92,96,99,120,121–131.

[175] E. Antolín, A. Martí, and A. Luque, "Energy conversion efficiency limit of series connected intermediate band solar cells," in 21th European Photovoltaic Solar Energy Conference, Dresden, Germany, 2006, pp. 412–5.

[176] S. Dahal, "k·p method for band structure calculation of intermediate band solar cell," Unpublished, annotated draft of a poster presentation, Nov. 2007, personal communication.

[177] G. Narvaez and A. Zunger, "Calculation of conduction-to-conduction and valence-to-valence transitions between bound states in (In,Ga)As/GaAs quantum dots," Physical Review B, vol. 75, no. 8, pp. 85 306 – 1, 2007.

[178] Y. Zhang, A. Pancholi, and V. Stoleru, "Size-dependent radiative lifetime in vertically stacked (In,Ga)As quantum dot structures," Applied Physics Letters, vol. 90, no. 18, pp. 183 104–1, 2007.

[179] H. Yu, S. Lycett, C. Roberts, and R. Murray, "Time resolved study of self-assembled InAs quantum dots," Applied Physics Letters, vol. 69, no. 26, pp. 4087 – 9, 1996.

[180] A. Martí, N. López, E. Antolín, E. Cánovas, C. Stanley, C. Farmer, L. Cuadra, and A. Luque, "Novel semiconductor solar cell structures: The quantum dot intermediate band solar cell," Thin Solid Films, vol. 511-512, pp. 638 – 44, 2006.

[181] G. Rowland, T. Hosea, S. Malik, D. Childs, and R. Murray, "A photomodulated reflectance study of InAs/GaAs self-assembled quantum dots," Applied Physics Letters, vol. 73, no. 22, pp. 3268 – 70, 1998.

[182] J. Rojas-Ramirez, A. Pulzara-Mora, E. Cruz-Hernandez, A. Perez-Centeno, M. Melendez-Lira, V. Mendez-Garcia, and M. Lopez-Lopez, "Photoreflectance study of InAs quantum dots on GaAs(n11) substrates," Physica E, vol. 32, no. 1-2, pp. 139 – 43, 2006.

[183] M. Motyka, G. Sek, R. Kudrawiec, J. Misiewicz, L. Li, and A. Fiore, "On the modulation mechanisms in photoreflectance of an ensemble of self-assembled InAs/GaAs quantum dots," Journal of Applied Physics, vol. 100, no. 7, pp. 073 502 –, 2006.

[184] G. Sek, K. Ryczko, M. Motyka, J. Andrzejewski, K. Wysocka, J. Misiewicz, L. Li, A. Fiore, and G. Patriarche, "Wetting layer states of InAs/GaAs self-assembled quantum dot structures: effect of intermixing and capping layer," Journal of Applied Physics, vol. 101, no. 6, pp. 63 539 – 1, 2007.

[185] W. Rudno-Rudziński, G. Sek, J. Misiewicz, T. Lamas, and A. Quivy, "The formation of self-assembled InAs/GaAs quantum dots emitting at 1.3 μm followed by photoreflectance spectroscopy," Journal of Applied Physics, vol. 101, no. 7, p. 073518, 2007.

[186] J.-R. Lee, C.-R. Lu, W.-I. Lee, and S.-C. Lee, "Investigation of populated InAs/GaAs quantum dots by photoluminescence and photoreflectance," Physica E, vol. 25, no. 4, pp. 562 –8, 2005.

[187] J. Prieto, G. Armelles, T. Utzmeier, F. Briones, J. Ferrer, F. Peiró, A. Cornet, and J. Morante, "Strain-induced quenching of optical transitions in capped self-assembled quantum dot structures," Physical Review Letters, vol. 80, no. 5, pp. 1094 – 7, 1998.

[188] R. Burden and J. D. Faires, Numerical Analysis, Sixth Edition. Oxford: Brooks/Cole Publishing Company, 1997, p. 199.

[189] G. L. Araújo and A. Martí, "Generalized detailed balance theory to calculate the maximum efficiency of solar cells," in Proceedings of the 11th EC PVSEC, Montreaux, Switzerland, 1992, pp. 142–5.

[190] M. Goano, "Algorithm 745: computation of the complete and incomplete Fermi-Dirac integral," ACM Transactions on Mathematical Software, vol. 21, no. 3, pp. 221–32, 1995.